# Study on the Frequency-Tunable $Ba_xSr_{1-x}TiO_3$ Films with Emphasis on Deposition Substrate Type and Demonstration of Frequency Conversion by a $Ba_xSr_{1-x}TiO_3$ Capacitor

（周波数可変素子用 $Ba_xSr_{1-x}TiO_3$ 薄膜の堆積基板依存性及びその周波数逓倍特性に関する研究）

**GUN BHAKDISONGKHRAM**

**Information Device Science**

**Graduate School of Materials Science**

**Nara Institute of Science and Technology**

**Advisor : Prof. Tadashi SHIOSAKI**

**February 2007**

## Abstract

Barium strontium titanate - $Ba_xSr_{1-x}TiO_3$ (BST) is one of the ferroelectric materials that are considered to be promising as a microwave material for tunable circuits. In such application, the material must possess high tunability, i.e. the strong dependence of permittivity on an applied dc bias. BST has such property because it has large dipoles. BST also benefits from fast switching speed and compatibility with IC process as demonstrated in DRAM technology. At room temperature, it is in paraelectric phase and has moderate dielectric loss. Moreover, its Curie point can be simply controlled by adjusting the Ba:Sr composition ratio during the film deposition, which enable the flexible manufacturing process. The dielectric property of BST films with different Br:Sr composition ratio (BST, x=0.3, 0.4 and 0.5) was studied in the first part of this thesis. The reason for choosing such composition will be described; although it was known that larger barium contents would result in higher tunability and permittivity, it was generally known that BST is likely to be in ferroelectric phase and has high dielectric loss at the composition x>0.5, and therefore the barium composition value x=0.3, 0.4 and 0.5 was chosen in this experiment. At room temperature, the relative

permittivity of the BST with composition x=0.3, 0.4, and 0.5 was observed to be 229, 354, and 616, respectively, and the resultant phase shift of the same waveguide structure at 7 GHz was $0.5^{o}$, $1.5^{o}$, and $2.5^{o}$, respectively. This result indicates that the films with x=0.5 has highest tunability.

Deposition of BST films that possess low dielectric loss and high tunability is the main objective. Unlike bulk or single crystal BST, thin BST films suffer from decrease in permittivity and high dielectric loss. This was considered to be due to defects occurring during deposition, and the dead layer in film interface because of the discontinuity of the atomic bonds at the material surface. Epitaxial BST film growth is one of the solutions to suppress the problems due to the defects, which is likely to be oxygen vacancies.

Magnesium oxide (MgO), strontium titanate (STO), and lanthanum aluminate ($LaAlO_3$) are popular substrates of choice that help assist the BST epitaxial growth. Nevertheless, those substrates are chosen mainly for research but not commercial manufacturing because of their high cost and deliquescence of the surfaces.

Substrate selection for epitaxial BST film growth was investigated using MgO, sapphire, and silicon substrates. BST films were directly deposited onto different types of substrates by conventional RF sputtering. The evaluation of BST films as microwave material was done through the measurement of phase shift of the microwave signal (8 GHz) passing through the waveguide on the BST/substrate. The phase shift was solely due to the permittivity change of the BST films, and not due to the substrates. The results showed that the c-cut sapphire assisted BST epitaxial 111-oriented film growth, while the MgO assisted BST 100-oriented film growth. The BST grown on silicon and r-cut sapphire preferred random orientation. At 7 GHz, The phase shift and dielectric loss due to the BST film (1 $\mu$m) deposited on MgO were $3.0^{o}$ and 0.75%, which is comparable to the values of $2.4^{o}$ and 0.68% in the case of BST deposited on the c-cut sapphire. Thus it was successfully demonstrated that the c-cut sapphire substrates are suitable for depositing BST films for microwave application.

On the other hand, despite the extensive research on the applications that make use of the large tunability of the BST films, little research has been carried out to realize a BST-based frequency conversion. Frequency conversion by a coplanar waveguide transmission line on a BST film has also been studied before. However, the nonlinearity

of a BST film in such a planar structure is not large enough for an effective frequency conversion. In this thesis, a parallel-plate capacitor was used to realize practical frequency conversion because it made the voltage drop across the capacitance higher. Practical frequency conversion due to BST film's nonlinearity was successfully demonstrated. It was also shown that the higher the frequency conversion efficiency can be achieved by increasing the input signal power. For the conversion from 500 MHz to 1 GHz, the conversion loss was -30 dB at an input power of 20 dBm.

## Contents

# Chapter 1. Introduction

## 1.1 Background

Wireless tunable circuits make use of several tunable components that can be adjusted by only applying a voltage bias adjustment. The advantages of this technology fulfill the requirements for modern telecommunication technology. Wireless communication devices used in radar, cellular, wireless LAN and other technologies, make uses of a number of tuned high-frequency analog circuits. Tuned circuits are designed to respond at some specific frequency, power level, or impedance. They play an important role in determining overall signal quality, sensitivity, size and power consumption of mobile devices and their base stations. However, these conditions may vary with location, and thus mobility in wireless system causes some sub-optimum performance of these conditions. The device designer may build several tuned components in a parallel configuration, and switch between them as conditions change. However, this may lead to associated penalties of increasing in size, weight and cost.

In many cases, a better solution is to use a single tunable circuit that is not only tuned, but “tunable”. Wireless tunable devices make use of several tunable circuits that can be adjusted by only applying a voltage bias adjustment. This may lead to a savings in cost, reduction in size, improved battery life, or increased manufacturability.

Examples of tunable devices

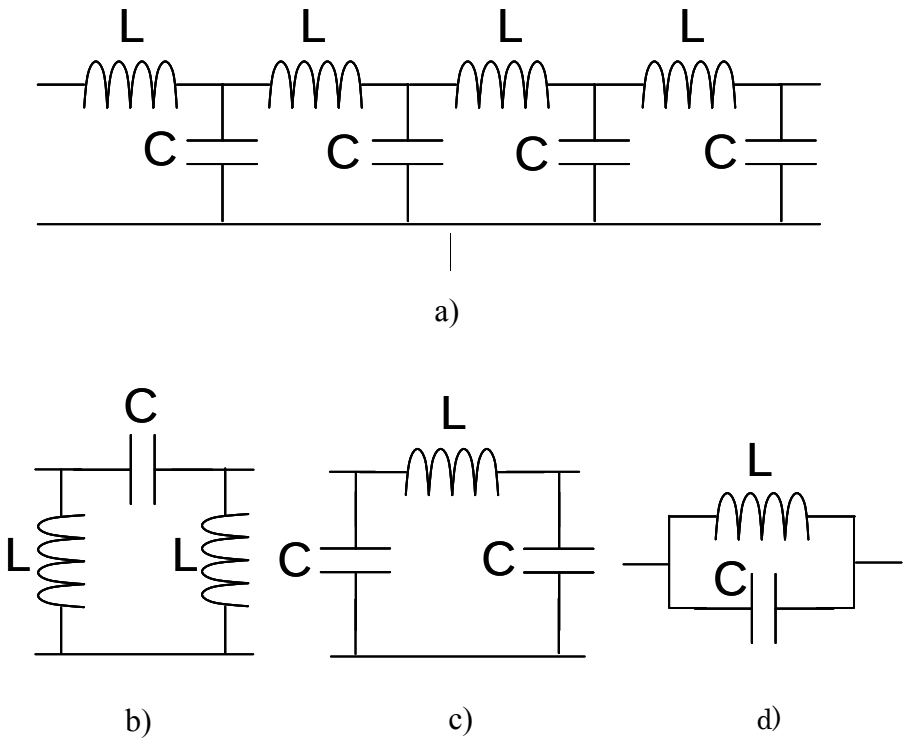


Figure 1-1 Equivalent circuits of a) the transmission line, b) the high-pass filter, c) the low-pass filter, d) the resonator.

From figure 1-1, the transmission line, high-pass or low-pass filter, and resonator can be modeled by using the capacitors and inductors. The value of the inductance and capacitance determines the characteristics of the devices.

For a phase shifter, the phase ( $\beta$ ), impedance (Z) and phase velocity (v) are expressed as:

$$\beta = \omega\sqrt{LC} \tag{1-1}$$

$$Z = \sqrt{\frac{L}{C}} \tag{1-2}$$

$$v = \frac{1}{\sqrt{LC}} \tag{1-3}$$

For a high-pass or low-pass filter, the cutoff frequency is expressed as:

$$\omega = \frac{1}{\sqrt{LC}} \tag{1-4}$$

For a resonator, a resonant frequency can be expressed as:

$$\omega = \frac{1}{\sqrt{LC}} \tag{1-5}$$

Accordingly, the characteristics of such devices can be adjusted by changing the value of the inductance (L) or capacitance (C).

In the case that the inductance is adjusted, the inductor's high losses at the microwave

frequency can be high. The limitation of the inductors, which is generally fabricated on the Si chip, is their power loss during operation, meaning that it requires high power consumption. The loss mechanisms for the inductors are:

1. At low frequencies, the loss is mainly due to the resistance encountered in the winding.

2. On a $SiO_2$/Si substrate, at low frequencies, the charge carriers in the substrate can follow the speed of the electric field of the alternating circuit signal, and the field thus terminates at the interface between the oxide and the silicon. At higher frequencies, the charge carriers in the substrate cannot follow the high speed of the ac field, thus the electric field penetrates into the silicon substrate. Thus the charges move in response to, but lag behind the applied ac field. In this case, the additional parallel substrate resistance must be taken into account. This kind of loss limits the use of an inductor at the microwave frequencies.

3. The magnetic field of the applied ac field also penetrates into the substrate. Considering a transformer where the field generated by one winding passes through another, a current is induced in the substrate flowing in the direction opposite to that of the intended signal. Continuing the transformer analogy, such *eddy current* flows in the secondary (substrate) side as a result of signal energy applied to the primary winding.

And just as with a transformer, loss in the “secondary” due to finite substrate resistivity can be observed through the primary side. At higher microwave frequency, this mechanism is the cause of very high loss in the silicon-based spiral inductor. Even the high-resistivity silicon-on-insulator substrate was used, the quality factor of the spiral inductor is less than 5 (equivalent to loss of 20 %), at 1 GHz [1].

On the other hand, the capacitance of a capacitor can be controlled by applying an external direct current (dc) bias. The ferroelectric capacitor suits for the tunable application. Figure 1-2 shows the capacitance of a capacitor that contains $Ba_{0.5}Sr_{0.5}TiO_3$. Figure 1-3 shows the expected result of tuning the devices. From the equations (1-1) to (1-5), in a transmission line, this capacitor can tune the value of phase to 66% and can shift the operating frequencies of high-pass filters, low-pass filters and resonators to 1.5 times. This range of tuning is enough for most applications.

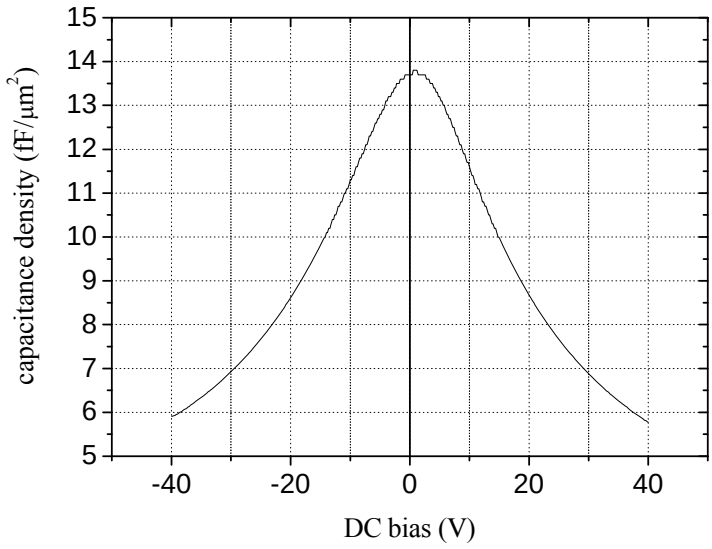


Figure 1-2 The capacitance as a function of an external direct current bias

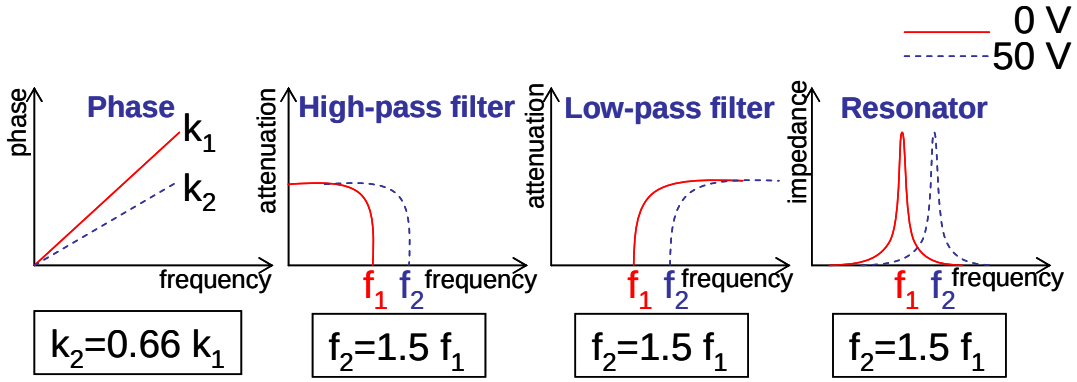


Figure 1-3 The expected results of tuning by a BST capacitor.

## Historical perspective

Ferroelectric behavior in materials was first observed in Rochelle salt in the 1920s. Barium titanate was recognized as a practical ferroelectric material in 1942–1943 by von Hippel at the Massachusetts Institute of Technology (MIT) [2]. Review of the *IEEE Microwave Theory and Techniques Society* (IEEE MTT-S) *International Microwave Symposium Digests* reveals two distinct periods of activity. The first stretched from approximately 1958 to the 1960s. Morgenthaler [3] and Coleman and Becker [4] discussed the possibility of ferroelectric phase modulators and mixers in 1958. DiDomenico and Pantell [5] described an -band waveguide ferroelectric phase shifter in 1962. In the same year, Cohn and Eikenberg described a stripline phase shifter for 100–1000 MHz. They described a PbTiO –SrTiO HF–UHF power limiter capable of handling 25-kW peak power in 1964 [6]. The application of ferroelectric materials as a millimeter- wave harmonic generator is reported by DiDomenico in a review paper in 1963 [7]. Das described their use in parametric amplifiers in 1965 [8]. Amoss *et al.* described a low-power switch using PbTiO –SrTiO elements in diode-like packages in 1965. Alday *et al.* described ferroelectric and pyroelectric millimeter-wave detectors [10] in 1966. Another limiter utilizing a packaged ferroelectric element was described by Horton and Donaldson in 1967 [11]. Van Doeren utilized ferroelectrics to rotate

wave polarization in 1966 [12]. A microstrip phase shifter using PbTiO –SrTiO was described by Das in 1967 [13]. Measurement techniques for dielectric constant and loss tangent were discussed by Horton and Burdick in 1968 [14]. Variable delay lines were investigated by Kirchner [15] and by Squire *et al.* [16] in 1969.

Little new work utilizing the unique properties of ferroelectric materials was reported until 1993. Beall, Ono, and Price made tunable microstrip resonators by combining the low loss of superconductors with thin film SrTiO, in contrast to the bulk ceramic most often used previously [17]. Cho combined piezoelectric and ferroelectric effects in a surface-acoustic-wave convolver in 1994 [18]. In 1995, Jackson *et al.* [19] described a coplanar waveguide X-band phase shifter producing $150^{o}$ phase shift with a 30 V bias at the temperature of 60 K. A finite-element analysis of microstrip lines on BaTiO –SrTiO substrates was reported by Sung *et al.* [20]. Abbas *et al.* discussed a model of a ferroelectric superconducting phase shifter in 1996 [21]. The preparation of various titanates by the sol-gel process was reported by DeFlaviis *et al.* and, in 1997, their devices yielded $165^{o}$ phase shift and less than 3-dB loss at 2.4 GHz [22]. In 1998, Subramanyam *et al.* used SrTiO in a 19-GHz tunable band pass filter, controlled by a 400-V bias [23]. Nonlinear effects including IMD and detuning were studied by

Kozyrev *et al.* [24]. Superconductors were again combined with ferroelectrics to make tunable filters for 0.5–2 GHz, by Gevorgian *et al.* [25]. A coupled microstrip approach was used in a phase shifter with BaTiO –SrTiO by Van Keuls *et al.* [26]. Coplanar waveguides were revisited by Carlsson and Gevorgian in 1999 [27].

## 1.2 Barium strontium titanate thin films ($Ba_xSr_{1-x}$)$TiO_3$

Barium strontium titanate $Ba_xSr_{1-x}TiO_3$ (BST) has been investigated as a proper dielectric material for a variety of applications such as dynamic random access memories (DRAM), bypass capacitors, non-volatile memories [28]. The BST films show a field-dependent permittivity. After an external DC voltage bias was applied to a BST capacitor, the dielectric constant of the BST film decreases in a non-linear way. This makes BST attractive for tunable microwave devices such as varactors, filters, voltage controlled oscillators (VCO), delay lines, matching circuits, antennas and phase shifters. BST based devices and circuits could provide an alternative to GaAs varactors which are the most popular but expensive. $Ba_xSr_{1-x}TiO_3$ is a continuous solid solution between $BaTiO_3$ and $SrTiO_3$. Figure 1-4 shows the perovskite structure of the unit cell of the BST material. BST films have a very high dielectric constant typically in the range of 100-1000 [28], making them suitable for small-area bypass capacitors. In

the early 1990's, there was a huge effort in DRAM industry for alternative high dielectric constant materials. BST have been investigated as a replacement for the silicon oxide/nitride dielectric material [28]. GaAs chips for wireless communication applications use on chip BST bypass capacitors gaining a performance advantage over external bypass capacitors. Smaller device packages with reduced pin count are possible which do not required external components and bonding.

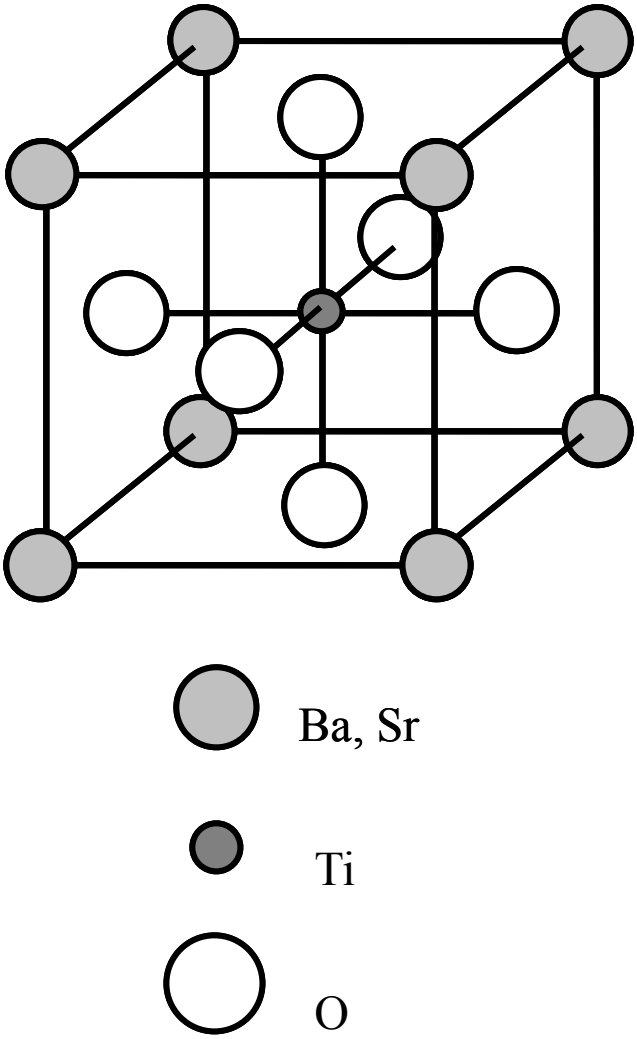


Figure 1-4 Perovskite structure of BST.

Figure 1-5 shows the structure and lattice constants as a function of Ba:Sr ratio [29]. One important feature of the BST is that its Curie temperature decreases linearly with increasing Sr concentration at a rate of 3.4 $^{o}$C per mole % Sr [30]. As a result, the transient temperature and hence the electrical and optical properties of BST can be tailored over a broad range to meet the requirements of various electronic applications.

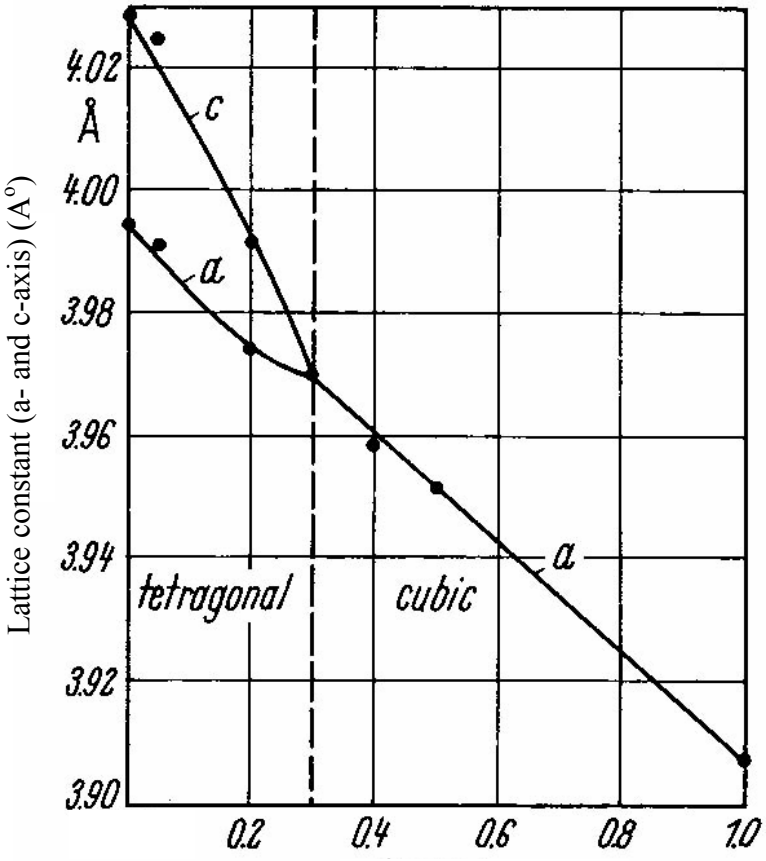


Figure 1-5 $(Ba_{1-x}Sr_x)TiO_3$ (ceramics) has the lattice constant in a- and c-axis that correspond to the tetragonal or cubic structure of the material. *x* is the ratio number of the Sr atoms [28].

## 1.3. BST-based varactor

BST-based varactors have high breakdown fields of typically $2\times10^6$V/cm [31]. They also allow a large RF signal to be applied to devices, which indicates good power-handling capability. Intrinsic fast polarization response of the BST films allows continuous and rapid tuning. The fast field response combined with the non-linear behavior of the dielectric permittivities enables frequency conversion devices such as multipliers and up/down converters using BST thin films. As most tunable devices are based on semiconductor materials, BST-based devices are of modern technologies, and are not well known. Table 1-1 shows materials that are promising for tunable device [30, 31]. The BST varactors have fast tuning speed, excellent power handling, and are cheap, but the disadvantages are their poor dielectric losses. Another important feature of BST based devices, in comparison to semiconductor-based alternatives, is the wide variety of substrate materials available for thin-film deposition. Using inexpensive substrates such as silicon or $Al_2O_3$ and high-volume deposition technologies, very low cost microwave circuits can be realized using thin-film BST. BST varactors also have higher breakdown field strengths and higher power handling capability than semiconductor varactor diodes. Good power handling and intermodulated distortion (IMD) can be obtained by using relatively thicker films at the expense of control voltage.

Table 1-1 comparison of varactor technologies [31]

| | GaAs | BST | MEMS |
|---|---|---|---|
| **Tunability** | **High (75%)** | **Moderate (55-70%)** | **Low (<50%)** |
| **RF Loss** | **Moderate (Q<60)** | **Moderate (Q<100)** | **Very Good (Q<200)** |
| **Control Voltage** | **<10 V** | **10-20 V** | **50-100 V** |
| **Tuning Speed** | **Fast** | **Fast** | **Slow** |
| **Power Handling** | **Poor** | **Excellent** | **Excellent** |
| **IMD** | **Poor** | **Poor** | **Excellent** |
| **Packaging** | **Hermetic** | **(Unknown)** | **Vacuum** |
| **Cost** | **High** | **Low** | **Low** |

## 1.4. Problems of thin films $(Ba_xSr_{1-x})TiO_3$ for microwave applications

Table 1-2 Permittivity, quality factor of dielectrics used as the microwave application [31]

| Material | $\varepsilon_r$ @ 25°C | Q = 1/tan$\delta$ @ 25°C |
|---|---|---|
| Ba-Zn-Ta-O | 30 | 12600 (@10 GHz) |
| Zr-Sn-Ti-O | 37 | 5800 (@ 9 GHz) |
| $Ba_2Ti_9O_{20}$ | 37 | 7000 (@ 7 GHz) |
| $ZrTiO_2$ | 42 | 4000 (@ 7 GHz) |
| Ba-Nd-Ti-O | 88 | 1100 (@ 5 GHz) |
| $TiO_2$ | 100 | 14500 (@ 3 GHz) |
| $CaTiO_3$ | 170 | 1800 (@ 2 GHz) |
| $SrTiO_3$ | 300 | 1000 (@10 GHz) |
| $Ba_{0.6}Sr_{0.4}TiO_3$ | 4000 | 50 (@10 GHz) |

Table 1-2 shows permittivity and quality factors (1/tanδ) of various dielectric materials for microwave applications [31]. Although high permittivity of the BST is promising for tunable applications, the fabrication of the BST films usually results in high dielectric losses (tanδ). This is mostly believed to be due to the defects in the films that emerge during the film deposition. Even in the case of sputtering deposition, which is an excellent way to fabricate a high-quality film, particle bombardment of BST target can introduce defects into films or simply cause oxygen resputtering. This is because the target is generally bombarded with the particles that have energy of 1-100eV, while defect formation is on the order of several eVs. Under a DC voltage field, the oxygen

vacancies migrate to the cathode and results in electron injection into the films. Under a microwave signal, the migration of these oxygen vacancies may not occurred due to the low speed of the migration than the switching speed of the applied signal. However, such vacancies may cause dislocation inside the films that are likely to induce stress or strain inside the films or cause some changes in lattice constants of the BST, resulting in higher dielectric loss and low tunability and permittivity.

## 1.5. Approaches to improvement of thin films $(Ba_xSr_{1-x})TiO_3$ for microwave applications

In general, it is believed that tunability higher than 50% should be enough for varactors to operate properly and it is almost impossible to increase the tunability to over 80% [1]. On the other hand, lowering the dielectric loss is very important. This is because the trade off value "tunability×1/tanδ", which is often used to determine the quality of the tunable components, can be increased more effective by 1 % of loss than 1 % of tunability. Moreover, a quality value of a device: Q=1/tanδ is an important parameter when choosing capacitors, resonators, or dielectric devices.

### 1.5.1 Deposition substrate selection

To achieve low-loss BST films, it is believed that fabricating the epitaxial films is necessary. This is because the epitaxial films resemble single crystal which has low distribution of defects. To fabricate the epitaxial films, substrates must be selected to match the lattice constant and thermal expansion coefficient of the BST films. Moreover the substrates itself should have low dielectric losses. Substrates such as MgO, $SrTiO_3$ or $LaAlO_3$ single crystals suit the above requirements and are considered as favorite options for the research. However, such substrates are expensive and thus may not be practical for manufacturing, especially when compared to the semiconductor-based tunable devices. In this thesis, low-cost substrates including sapphire and Si were investigated as deposition substrates and were compared to MgO. The permittivity, tunability, and dielectric loss of deposited BST on different substrate types were evaluated.

### 1.5.2 Consideration for frequency conversion by using BST capacitor

Conventional passive multipliers can be classified as resistive or capacitive types. In the first case, the frequency–multiplying mechanism is due to the strong nonlinearity of the conduction current flowing in the diode. In the latter case, the frequency-multiplying mechanism is due to the nonlinear nature of the reactance of the diode. The mechanism

of the multiplier presented in my thesis is similar to that of the latter case. However, unlike the conventional semiconductor diode, the nature of an ideal dielectric material is that it does not contain free electrons that generate noise in the device. Thus, it can be expected to have a lower noise level than in conventional devices. Moreover, low leakage currents in dielectrics result in some advantages such as lower DC power consumption and higher breakdown voltage.

## 1.6 Objective and Justification

There are two main objectives in this dissertation. One is to deposit the BST film that has low dielectric loss (<2%) and high tunability (>50%), especially at the microwave frequency. The other one is to demonstrate frequency conversion (producing the output signal at 1 GHz) due to the nonlinearity of the BST capacitor.

**Approach to the deposition of the BST films that possess low dielectric loss and high tunability**

Features of this approach in this dissertation include:

(i) The dielectric property of BST films with different Br:Sr composition ratio (BST, x=0.3, 0.4 and 0.5) was studied in the first part of this thesis. The reason for

choosing such composition will be described; although it was known that larger barium contents would result in higher tunability and permittivity, it was generally known that BST is likely to be in ferroelectric phase and has high dielectric loss at the composition x>0.5 [31], and therefore the barium composition value x=0.3, 0.4, and 0.5 was chosen in this experiment.

(ii) Epitaxial BST film growth is one of the solutions to suppress the problems due to the defects, which is likely to cause high dielectric loss. Although magnesium oxide (MgO), strontium titanate (STO), and lanthanum aluminate ($LaAlO_3$) are popular substrates of choice that help assist the BST epitaxial growth, these substrates have severe disadvantages due to their high cost and the deliquescence of the surfaces. Low-cost substrate including sapphire and silicon substrates were chosen and investigated for epitaxial BST film growth. MgO, sapphire, and silicon substrates. BST films were directly deposited onto different types of substrates by conventional RF sputtering.

(iii) Even small phase shifts on different samples can be reliably compared, because the on-wafer Thru-Reflect-Line calibration was used to ensure the preciseness of the measurement during the measurement of phase shift.

**Demonstration of the frequency conversion due to the nonlinearity of the BST capacitor**

A simple circuit was used to make a high voltage drop across the capacitance. As a result, the electric charge and electric current across the BST capacitor are distorted because of the nonlinear electric charge-voltage characteristics of the BST films. This distortion includes high-order harmonics whose frequencies are multiples of the input signal frequency. Therefore, these higher-harmonic signals can be filtered out as a signal of the multiplied frequency. The more an input signal is distorted, the larger a harmonic signal becomes.

## 1.7 Dissertation outline

The dissertation was organized into five chapters:

**Chapter 1** is a general introduction for the entire study, including the necessity of tunable circuits, brief introduction to the dielectric property of BST material and BST varactors. Some features of the approaches used in this dissertation will be described; namely composition selection, substrate selection for epitaxial growth, and demonstration of the frequency conversion by using a BST capacitor.

**Chapter 2** explains the process of BST film deposition and the resultant tunability, permittivity and dielectric loss at low frequency. The relationship of the structural, microstructural, and electrical properties is discussed.

**Chapter 3** explains the measurement and results of coplanar waveguide at microwave frequency. In such waveguide structure, the tunability is expressed in a form of phase shift after a DC bias was applied. The on-wafer Thru-Reflect-Line calibration helps to ensure the precise measurement results. Based on the findings of Chapter 2 on preparation of high-tunability and low-loss BST films by RF sputtering method, presents the deposition of BST on different substrate types including sapphire, MgO and silicon in order to achieve epitaxial growth. Tunability of the BST film was evaluated as the phase shifts in a coplanar waveguide. The relationship between the crystallinity of the BST and the results of phase shift and dielectric loss of BST on different substrates was discussed.

**Chapter 4** demonstrates the frequency conversion by using a BST capacitor. A simple circuit was chosen to intentionally drop more voltage on the BST capacitor. As a result, nonlinearity of the film was observed as the distortion of the out signal across the BST

capacitor.

**Chapter 5** draws general conclusion from this study.

## References

1) Junichi Kodate, Takafumi Douseki, Tsuneo Tsukahara, Takehito Okabe and Nobuhiko Sato, “Practical high-resistivity silicon-on-insulator solution for spiral inductors in radio-frequency integrated circuits”, Japanese Journal of Applied Physics, **44** 8 (2005) 5987

2) A. von Hippel, “Dielectric materials and applications”, Cambridge, MA, MIT Press, 1954

3) F. R. Morgenthaler, “Velocity modulation of electromagnetic waves”, IEEE Transaction of Microwave Theory and Techniques, vol. 6, (1958) 167

4) P. D. Coleman and R. C. Becker, “Present state of the millimeter wave generation and technique art—1958,” IEEE Transaction of Microwave Theory and Techniques, vol. 7, (1959) 42

5) M. DiDomenico, Jr. and R. H. Pantell, “An X-band ferroelectric phase shifter,” IEEE Transaction of Microwave Theory and Techniques, vol. 10, (1962) 179

6) M. Cohn and A. F. Eikenberg, “Ferroelectric phase shifters for VHFand UHF,” IEEE Transaction of Microwave Theory and Techniques, vol. 10, (1962) 536

7) P. D. Coleman, “State of the art: Background and recent developments—Millimeter

and submillimeter waves," IEEE Transaction of Microwave Theory and Techniques, vol. 11, (1963) 271

8) S. N. Das, "Application of barium titanate compositions to parametric amplification (correspondence)," IEEE Transaction of Microwave Theory and Techniques, vol. 13, (1965) 245

9) J. W. Amoss, M. R. Donaldson, L. J. Lavedan, A. L. Stanford, and J.E. Pippin, "A ferroelectric microwave switch," IEEE Transaction of Microwave Theory and Techniques, vol. 13, (1965) 789

10) J. R. Alday, G. E. Everett, and D. J. White, "Improved response of pyroelectric millimeter wave detectors (correspondence)," IEEE Transaction of Microwave Theory and Techniques, vol. 14, (1966) 100

11) J. B. Horton and M. R. Donaldson, "A one-GHz ferroelectric limiter," IEEE Transaction of Microwave Theory and Techniques, vol. 15, (1967) 517.

12) R. E. Van Doeren, "Polarization transformation in twisted anisotropic media," IEEE Transaction of Microwave Theory and Techniques, vol. 14, (1966) 106

13) R. Das, "Ferroelectric phase shifters," in IEEE MTT-S Int. Microwave Symposium Program Digest, vol. 1, (1967), 185

14) J. B. Horton and G. A. Burdick, "Measurement of dielectric constant and loss

tangent in materials having large dielectric constants (correspondence)," IEEE Transaction of Microwave Theory and Techniques, vol. 16, (1968) 873

15) E. K. Kirchner, "Microwave variable delay devices," IEEE Transaction of Microwave Theory and Techniques, vol. 17, (1969) 986

16) W. D. Squire, H. J. Whitehouse, and J. M. Alsup, "Linear signal processing and ultrasonic transversal filters," IEEE Transaction of Microwave Theory and Techniques, vol. 17, (1969) 1020

17) J. A. Beall, R. H. Ono, D. Galt, and J. C. Price, "Tunable high temperature super conductor microstrip resonators," in IEEE MTT-S Int. Microwave Symposium Program Digest, vol. 3, (1993) 1421

18) Y. Cho, S.-I. Haitsuka, and M. Kadota, "20 dB efficiency increment of surface acoustic wave elastic convolver using actively controlled nonlinear piezoelectric effect," in IEEE MTT-S Int. Microwave Symposium Program Digest, vol. 2, (1994) 1217

19) C. M. Jackson, T. Pham, Z. Zhang, A. Lee, and C. Pettiete-Hall, "Model for a novel CP W phase shifter," in IEEE MTT-S Int. Microwave Symposium Program Digest, vol. 3, (1995) 1439

20) Y. Sung, S. Choi, and S. Nam, "Finite element analysis of microstrip line on ferroelectric (Ba–Sr)TiO substrate," in IEEE MTT-S Int. Microwave Symposium

Program Digest, vol. 3, (1995) 1261

21) F. Abbas, L. E. Davis, and J. C. Gallop, "A distributed ferroelectric superconducting transmission-line phase shifter," in IEEE MTT-S Int. Microwave Symposium Program Digest, vol. 3, (1996) 1671

22) F. De Flaviis, D. Chang, N. G. Alexopoulos, and O. M. Stafsudd, "High purity ferroelectric materials by sol-gel process for microwave applications," in IEEE MTT-S Int. Microwave Symposium Program Digest, vol. 1, (1996) 99; vol. II, (1998) 1027

23) G. Subramanyam, F. Van Keuls, and F. A. Miranda, "A K-band tunable microstrip bandpass filter using a thin-film conductor/ferroelectric/dielectric multilayer configuration," IEEE Microwave Guided Wave Letters, vol. 8, (1998) 78

24) A. Kozyrev, A. Ivanov, V. Keis, M. Khazov, V. Osadchy, T. Samoilova, O. Soldatenkov, A. Pavlov, G. Koepf, C. Mueller, D. Galt, and T. Rivkin, "Ferroelectric films: Nonlinear properties and applications in microwave devices," in IEEE MTT-S Int. Microwave Symposium Program Digest, vol. 2, (1998) 985

25) S. S. Gevorgian, E. F. Carlsson, E. L. Kollberg, and E. Wikborg, "Tunable superconducting band-stop filters," in IEEE MTT-S Int. Microwave Symposium Program Digest, vol. 2, (1998) 1027

26) F. W. Van Keuls, C. H. Mueller, F. A. Miranda, R. R. Romanofsky, C. L. Canedy, S.

Aggarwal, T. Venkatesan, R. Ramesh, J. S. Horwitz, W. Chang, and W. J. Kim, “Room temperature thin film Ba Sr TiO Ku-band coupled microstrip phase shifters: effects of film thickness, doping, annealing and substrate choice,” in IEEE MTT-S Int. Microwave Symposium Program Digest, vol. 2, (1999) 737

27) E. Carlsson and S. Gevorgian, “Conformal mapping of the field and charge distributions in multilayered substrate CPWs,” IEEE Transaction of Microwave Theory and Techniques, (Special Issue), vol. 47, (1999) 1544

28) A. K. Tagantsev, V. O. Sherman, K. F. Astafiev, J. Vankatesh, N. Setter, “Ferroelectric Materials for Microwave Tunable Applications”, Journal of Electroceramics, **11** (2003) 5

29) D. F. Rushman, M. A. Strivens, “The Permittivity of Polycrystals of the Perovskite Type”, Transaction of Faraday Society **42**, (1946) 231

30) B. A. Baumert, L. H. Chang, A. T. Matsuda, T. L. Tsai, C. J. Tracy, R. B. Gregory, P. L. Fejes, N. G. Cave and W. Chen, “Characterization of sputtered barium strontium titanate and strontium titanate-thin films”, Journal of Applied Physics, **82** (5) (1998) 2558

31) Y. Liu, “ MEMS and BST Technologies for Microwave Applications”, University of California (Santa Barbara), Ph.D. thesis, (2002)

# Chapter 2. Dielectric properties of $Ba_{0.3}Sr_{0.7}TiO_3$, $Ba_{0.4}Sr_{0.6}TiO_3$ and $Ba_{0.5}Sr_{0.5}TiO_3$ at frequency below 10 MHz and the electrical properties of the varactors based on these films

In this chapter, Barium Strontium Titanate (BST) film growth by RF sputtering and the resultant dielectric characteristics are presented for several film compositions; $Ba_{0.3}Sr_{0.7}TiO_3$, $Ba_{0.4}Sr_{0.6}TiO_3$ and $Ba_{0.5}Sr_{0.5}TiO_3$. All the films were grown onto Pt/Si substrates and were finally built into parallel plate capacitors. BST deposition and the resulting electrical characteristics are discussed.

## 2.1 Introduction

### 2.1.1. Deposition Methods for $(Ba_xSr_{1-x})TiO_3$ thin films [1]

Table 2-1 shows the advantages and limitations of oxide films deposition [1]. Solution method such as sol-gel produces a film from a homogenous solution which contains the precursors. The solution is spun, or sprayed onto a substrate while hydrolysis and poly-condensation occur. This process produces an amorphous thin film. Heating of the amorphous film helps the film to crystallize. Energetic process use energetic ions to

bombard a solid target source material, in vacuum. Gas phase collisions and scattering make the target material deposit onto the substrate [2].

Table 2-1 Deposition methods for thin ferroelectric films [1]

| **Growth Method** | **Advantages** | **Limitations** |
|---|---|---|
| Solution | | |
| Sol-Gel & Chemical Solution Deposition(CSD) | Inexpensive<br>Rapid turnaround and sampling | Phase control<br>Composition control<br>Morphology<br>Reproducibility<br>Scalability |
| Energetic | | |
| Sputtering | Uniformity<br>Scalability<br>Low thermal budget | Point defect concentrations<br>Limited compositional control<br>High residual stress<br>Poor conformality |
| Pulsed Laser Deposition (PLD) | Rapid sampling<br>Quickly produce new materials | Morphology<br>Point defect concentration<br>Scalability<br>Uniformity<br>High residual stresses |
| Vapor | | |
| Metal organic chemical Vapor deposition | Uniformity<br>Morphology<br>Composition control<br>Low thermal budget<br>Scalability<br>High conformality | Expensive<br>Precursor availability<br>Precursor stability<br>Still a relative immature technology |

Control over process gases, deposition substrate temperature, gas pressure and plasma power makes it possible to adjust the electrical properties of the deposited films. In Metal organic chemical vapor deposition (MOCVD) method, organic precursors, such as metal alkoxides and diketonates, containing the required cation are vaporized and transported to the substrate [1]. Precursor decomposition at the substrate surface, when heated, results in film growth. Precise control of the precursor and gas flow rate into the MOCVD reactor results in strict control over film stoichiometry and growth.

### 2.1.2. Rf magnetron sputtering for $(Ba_xSr_{1-x})TiO_3$ thin films

In the sputtering method, compounds are volatilized stoichiometrically by positive ion bombardment. The advantage of this method is that the uniformity over large areas can be excellent. The sputtering occurs within plasma, which is a partially ionized gas composed of ions, electrons and neutral species. When the plasma is struck at a low gas pressure, the cathode is bombarded by the ionized gas molecules and surface of the target material, which is placed at the cathode, are removed, disintegrated and leave the target surface as atoms or chemical compounds and then move toward the substrate that is placed at the anode. This makes the deposition of the films on the substrates. The deposition rate depends on the target-to-substrate distance. Argon is typically used for

bombarding because it is an inert gas, has a low ionization potential and is cost effective.

RF magnetron sputtering was designed for insulators because the insulating target will self bias to a negative potential, as a consequence of faster response times of electrons compared to ions when following an alternating electric field [1]. A magnetic field helps confine the plasma, thus produce higher deposition rate. Typically, energy distributions in rf sputtering range from 1 to 10 eV. The distribution for sputtered sputtered particles generally peaks from 1 to 5 eV, and may extend to 100 eV [4]. The bombardment of material by ions results in residual damage in the growing film. The stress in the sputtered film is a function of substrate temperature, sputtering gas and gas pressure. Particle bombardment of $BaTiO_3$ and $SrTiO_3$ can introduce defects into the films or cause the resputtering of oxygen because defect formation is on the order of 2-5 eV [5]. It has been well shown that in $BaTiO_3$ and $SrTiO_3$ bulk ceramics that defects and nonstoichiometry lower the materials quality factor and overall electrical performance [6].

### 2.1.3. Previous works [2], [7-35]

**Tunability [2, 7-15]**

The application of ferroelectric materials in tunable high-frequency devices dates back over 40 years, when the ferroelectric material in the form of ceramics or single crystal was mainly used [2]. However, due to both device electronics and materials technology, it is only in the past decade that intensive efforts are being made for the ferroelectric thin films in the microwave application. The main driving force for this resurgent interest is the potential for miniaturization of the microwave device, and the potential for integration with microelectronic circuits following the development of thin and thick film ferroelectric technology [2].

It is believed that tunability is largely dependent on the behavior of the soft mode, i.e. the lowest frequency transverse optical phonon, whose zone-center frequency is connected to the static dielectric constant via Lyddane-Sachs-Teller (LST) relationship and vanishes at the temperature of the ferroelectric phase transition [7]. In fact, it has been shown that the phenomenon of tunability in the bulk is due to the field-induced hardening of the soft-mode, which arises from the anharmonic restoring forces on the Ti

ion when it is displaced from its equilibrium position [8].

In fact, several reasons are believed to induce the hardening of the soft mode in thin films and will be listed below [2, 7-15].

- *Strain* in thin film due to the lattice mismatch with substrate.

- Depolarization field due to *discontinuity at the interfaces*.

- *Oxygen vacancies*, which is well known as a common defects in titanates.

These oxygen vacancies emerge from impurities and cation nonstoichiometry. It was shown that the oxygen vacancies give rise to the appearance of local polar regions, which have a polarization that may cause an increase in the soft-mode frequency in the film.

The dependence of the dielectric permittivity on the applied dc bias electric field $E_0$ can be expressed as:

$$n = \frac{\varepsilon(0)}{\varepsilon(E_0)} \tag{2-1}$$

where; n : tunability

$\varepsilon(0)$: dielectric constant at the zero bias

$\varepsilon(E_0)$: dielectric constant when the bias of $E_0$ is applied to the film

and relative tunability:

$$n_r = \frac{\varepsilon(0) - \varepsilon(E_0)}{\varepsilon(0)} = \frac{n-1}{n} \tag{2-2}$$

where;

$n_r$ : relative tunability

n : tunability

$\varepsilon(0)$: dielectric constant at the zero bias

$\varepsilon(E_0)$: dielectric constant when the bias of $E_0$ is applied to the film

First, in the case of weak nonlinearity, i.e. when the relative tunability is very low ($n_r << 1$), the tunability becomes:

$$n = \frac{\varepsilon(0)}{\varepsilon(E_0)} = 1 + 3\beta\varepsilon(0)\varepsilon_0 P_{dc}^2 \approx 1 + 3\beta(\varepsilon(0)\varepsilon_0)^3 E_0^2 \tag{2-3}$$

where;

n : tunability

$\varepsilon(0)$: dielectric constant at the zero bias

$\varepsilon(E_0)$: dielectric constant when the bias of $E_0$ is applied to the film

$\beta$ : constant coefficient

From the above equation, the relative tunability becomes strongly dependent on the permittivity:

$$n_r = \frac{n-1}{n} \propto \varepsilon(0)^3 \tag{2-4}$$

In the case of strong nonlinearity, i.e. when $n >> 1$, the tunability becomes:

$$\varepsilon(E_0) \approx \frac{\beta^{-\frac{1}{3}} E_0^{-\frac{2}{3}}}{3\varepsilon_0} \tag{2-5}$$

From the above equation, the tunability is a linear function of the permittivity $\varepsilon(0)$.

$$n = \frac{\varepsilon(0)}{\varepsilon(E_0)} \quad \propto \quad \varepsilon(0) \tag{2-6}$$

It is instructivethat the dc field required to achieve a given tunability *n* is [2]:

$$E \; = \frac{\sqrt{n-1}(2+n)}{\varepsilon_0 \sqrt{27\beta\varepsilon_0}} \frac{1}{\varepsilon(0)^{\frac{3}{2}}} \tag{2-7}$$

**Dielectric Permittivity [2, 13-35]**

The origin of the high dielectric permittivity of the ferroelectrics in the paraelectric phase is a delicate compensation of various kinds of microscopic forces that maintains the material in a non-poled state in the absence of a microscopic electric field [2]. Because of this compensation, the restoring force opposing the poling action of the applied field is relatively weak [2]. This results in a high dielectric permittivity of the material. In addition to this, the permittivity may be further increased by contributions from ferroelectric domains. For microwave application, paraelectric phase of the ferroelectric is believed to exhibit a high tunability and a relatively low loss at microwave frequencies [2].

The general description of the dielectric response of ferroelectrics is given by the conventional Landau theory and is based upon an expansion of the Helmholtz free energy ($F$) with respect to the vector macroscopic polarization ($P$). For this situation where the polarization is collinear with the macroscopic electric field *(E*) in the material, the first two terms of this expansion read [2]:

$$F = \frac{\alpha}{2}P^2 + \frac{\beta}{4}P^4 \tag{2-8}$$

The equation of state $E = \frac{\partial F}{\partial P}$ then leads to a relation between the polarization and electric field:

$$E = \alpha P + \beta P^3 \tag{2-9}$$

From this equation, the relative dielectric permittivity of the material can be presented as:

$$\varepsilon = \frac{1}{\varepsilon_0}\frac{\partial P}{\partial E} = \frac{1}{\varepsilon_0}\frac{1}{\alpha + 3\beta P^2} = \varepsilon(0)\frac{1}{1 + 3\beta\varepsilon(0)\varepsilon_0 P^2} \tag{2-10}$$

where $\varepsilon(0) = (\varepsilon_0\alpha)^{-1}$ and $\varepsilon_0 = 8.854 \times 10^{-12}$ $[F/m]$.

This expression describes the dielectric permittivity both in the absence of a bias field ($P$=0) and under it ($P$=$P_{dc}$).

In Landau theory, the coefficient $\alpha$ is assumed to be a linear function of temperature and vanishes at the Curie-Weiss temperature $T_0$.

$$\alpha = \alpha_L = \frac{1}{\varepsilon_0}\frac{T - T_0}{C} \tag{2-11}$$

where $C$ is the Curie-Weiss constant. This assumption of the Landau theory is valid when $\frac{|T - T_0|}{T_0} << 1$. The theory is in good agreement with the experiment using the materials $SrTiO_3$ and $KTaO_3$. The above equation is not valid when the temperature is much below the Debye temperature (Debye temperature are about 400 K for $SrTiO_3$ and $KTaO_3$), where the quantum statistics of the lattice vibration should be taken into account [2].

An essential feature of the displacive ferroelectrics is the typical value of the Curie-Weiss constant $C$ of about $10^5$ K. Such a value of $C$ implies high values of the dielectric permittivity even far from the Curie-Weiss temperature $T_0$ [2].

**Dielectric loss in ferroelectrics [2], [7-25]**

At the microwave frequencies, both intrinsic mechanisms (due to fundamental phonon loss) and extrinsic mechanisms (due to the coupling of the microwave field with defects of the films) are believed to be main reasons for the dielectric losses. These mechanisms are listed below.

1) Intrinsic loss

This type of dielectric loss is due to the interaction of the electromagnetic field with the phonons of the material. A theory is developed for materials where the damping of phonons (average frequency of the inter-phonon collisions) is much smaller than their frequencies. This theory predicts that the fundamental loss mainly corresponds to the absorption of the energy quantum ($\hbar\omega$) of the electromagnetic field in collisions with the thermal phonons that have higher energies. In these collisions, the large difference of the energies makes it difficult for the conservation law to be satisfied. In such a situation, there exist three efficient schemes of absorption of the $\hbar\omega$ quanta, which are: [1] three-quantum, [2] four-quantum, and [3] quasi-Debye.

[1] Three-quantum mechanism

This mechanism involves a $\hbar\omega$-quantum (energy of the electromagnetic field) and two phonons, and occurs only where difference of the different phonon branches is in the order of $\omega$ or of the phonon damping. These regions are usually located in the vicinity of the degeneracy lines of the spectrum, i.e. the lines in $\vec{k}$-space where the frequencies of different branches are equal.

In the materials for tunable applications, the phonon spectrum contains low-lying (soft)

optical modes controlling their high dielectric permittivity. And the degeneracy lines formed with participation of these modes are of primary importance for the loss. Because the degeneracy of the spectrum is mainly controlled by the symmetry of the crystal, the explicit temperature dependence (which does not take into account the temperature dependence of the dielectric permittivity) and frequency dependence of the three-quantum loss are very *sensitive* to the symmetry of the crystal.

For microwave high-$\varepsilon$ and tunable materials, which are typically centrosymmetric, cubic or pseudocubic, the temperature, frequency ($\omega$), and dielectric permittivity are believed to be related in an analytical form, from the model in which the dielectric response is assumed to be controlled only by the lowest polar transverse optical (TO) mode. In this model, the damping of these phonons is proportional to the temperature value. This model predicts a fast growth of dielectric loss with increasing permittivity.

For high-$\varepsilon$ but non-ferroelectric materials, an experiment that supported this theory was carried out in a system of complex perovskites $Ba(M_{1/2}N_{1/2})O_3$ (M = Mg, In, Y, Gd, Nd and N = W, Ta, Nb). These are cubic non-ferroelectric (pseudo-cubic) centrosymmetric materials with the relative dielectric permittivity ranging from 20 to 40.

In the experiment, at the frequency range of sub-millimeter wave frequency (~300 GHz), the imaginary part of the dielectric permittivity was expected to be controlled mainly by the three-quantum mechanism. As predicted by the model, a strong correlation between imaginary part ($\varepsilon''$) and the real part ($\varepsilon$) of the dielectric permittivity was revealed in the experiment. The numerical results matched well with the theory, except that there was some deviation which was considered to be due to a small but appreciable dispersion of the optical (TO) modes in the studied materials (as the non-ferroelectric crystals are usually supposed to have a *negligible* TO mode dispersion).

For the case of a tunable material with ferroelectric soft mode, the above theory was studied by using the $SrTiO_3$ crystals, at the frequency of 9 GHz. In this case, the expression of the loss tangent becomes;

$$\tan\delta \equiv \frac{\varepsilon''}{\varepsilon} \propto \omega T^2 \varepsilon^{1.5} \qquad (2\text{-}12)$$

where $\tan\delta$ is the dielectric loss; $\varepsilon''$ and $\varepsilon$ are the imaginary part and the real part of the dielectric permittivity; $\omega$ is the electromagnetic wave frequency; T is the temperature. The expression was in good agreement with the experimental data.

[2] Four-quantum mechanism

The four-quantum mechanism involves a $\hbar\omega$-quantum (energy of the electromagnetic

field) and three phonons. From the conservation laws of energy and quasi-momentum, there are no strong restrictions on the type and energy of the phonons participating in these processes. For this reason, in contrast to the three-quantum processes, not only the degeneracy lines but also the whole thermally excited part of the $\vec{k}$-space contributes to the loss. Therefore, the explicit temperature and frequency dependence of the contribution of this mechanism to the imaginary part of the dielectric permittivity appears to be *insensitive* to the symmetry of the crystal. At room temperature, the expression of the loss tangent is identical to the case of three-quantum mechanism in the ferroelectric material. Although the expression of the loss tangent of the three-quantum and four-quantum mechanism is identical, the value of $\varepsilon''$ is different. Based on the order-of-magnitude estimates, it is expected that, in the ferroelectric materials, the three-quantum contribution is dominant in the total intrinsic loss [2].

- Other proposed intrinsic loss mechanism

Other than the three- and four-quantum mechanisms, the “Vendik model” and the “Damped oscillator model” were the two models that have been independently developed. The Vendik model can be categorized into the case of four-quantum mechanism. This model has been well supported by experimental results.

The damped oscillator model calculates the loss tangent from the shape of the far-infrared absorption lines (associated with transverse optical branches) at the alternating-current (ac) field frequency, which is much below the resonance frequencies.

[3] Quasi-Debye loss mechanism

The relaxation of the phonon distribution function is the reason for dielectric loss in a similar way as a relaxation of the distribution function of the dipoles gives rise to the loss in the Debye theory. This analogy is expressed by “quasi-Debye”. In this mechanism, the small oscillating ac field results in time modulation of the phonon frequencies, therefore induces a deviation of the phonon distribution fro m the equilibrium. The average relaxation time of the phonon distribution function is expressed as the Debye relaxation time, which is the origin of the frequency dependence of the dielectric loss.

This mechanism does not apply for the centrosymmetric crystals. However, when such crystals are under an external direct current (dc) bias, the symmetry is broken due to the dc-field-induced quasi-Debye mechanism. There is a reasonable agreement between the theory and experiment in $SrTiO_3$, $(BaSr)TiO_3$ and $KTaO_3$, however the theoretical estimates are questionable due to the lack of reliable information on the damping of the

phonons participating in the microwave absorption.

For low applied dc field, this mechanism predicts a quadratic field dependence of the dc field on the dielectric loss. However, for higher fields, the dependence appears to be different for different materials. In the case of $SrTiO_3$ and $Ba_{0.6}Sr_{0.4}TiO_3$, the value of these materials` dielectric loss at zero bias (0 V) was taken from the experiment and then the dielectric loss as a function of an external dc bias (ranging from 0 to 200 kV/cm) was theoretically simulated at 1 GHz. The simulated results showed the dielectric loss ranging from 0.001 to 0.005 for $SrTiO_3$, and 0.0004 to 0.001 for $Ba_{0.6}Sr_{0.4}TiO_3$. The significant difference of the dielectric loss between the two materials was due to the difference in the strength of the flexoelectric coupling between the soft mode and the acoustic branches in these materials. In the case of $SrTiO_3$, the loss was related to the contribution of the acoustic phonon to the quasi-Debye loss, which is activated by this flexoelectric coupling, in contrast to the case of $Ba_{0.6}Sr_{0.4}TiO_3$ where such dielectric loss mechanism is negligible because the flexoelectric coupling is much smaller. For higher frequency, this mechanism predicts higher dielectric loss. For instance, at an applied dc bias of 100kV/cm and the ac frequency of 25 GHz, the dielectric loss of $SrTiO_3$ and $Ba_{0.6}Sr_{0.4}TiO_3$ are expected to be 0.1 and 0.02 at the temperature of 80 K and 300 K, respectively. The assumed temperature of 80 K and 300

K are selected for high permittivity and tunability for these materials.

2) Extrinsic loss

In the case of tunable ferroelectric materials at microwave frequencies, the intrinsic and extrinsic contributions to the dielectric loss are comparable. And the dominating mechanism for loss is considered to depend on the quality of the material [2]. There are three types of known mechanisms for extrinsic loss;

[1] Loss due to charges defects

An ac electric field causes the motion of charged defects and thus results in the generation of the acoustic waves at the frequency of the applied field [2]. This mechanism becomes dominant in thin films because of the higher defect concentration than in the bulks. An important feature is that the dielectric loss in this mechanism is a direct function of the permittivity of the material and inversely dependent on the applied dc field [2].

[2] Universal-relaxation-law mechanism

For frequencies below microwave region, weak frequency dependence is usually observed. This cannot be explained by other mechanisms discussed above, which

predict the loss tangent as a linear function of frequency. The weak frequency dependence is found to be consistent with the so-called universal relaxation law. The origin of this behavior is attributed to a variation in charge transport barriers, e.g. at the grain boundaries, or the creep of the boundary of the near-by-electrode depletion layer. In this mechanism, no information is available on the dependence of the dielectric loss on the dielectric constant of the material. In $BaSrTiO_3$ films, the dielectric relaxation was modeled up to the microwave frequencies.

[3] Impact of local polar regions

Although the tunable materials usually are centrosymmetric, there may exist the local polar regions induced by various defects and structural imperfections. For example, recent infrared reflectivity investigations of $SrTiO_3$ ceramics revealed a presence of grain-boundary-induced polar phase inclusions [2]. Random field defects can also be responsible for the appearance of local polar regions. In all these situation, the quasi-Debye mechanism is considered to be active and can be dominant contribution of the dielectric loss. Although the “defect-induced” quasi-Debye mechanism is not developed, the strong dependence of the dielectric constant on the dielectric loss can be expected [2].

## 2.2 Experimental

### 2.2.1. Fabrication of BST thin films

BST film deposition was carried out in a custom built RF magnetron sputtering system. The sputtering system has a heater capable of heating the substrate up to $700^{o}$ C. Distance between the substrate and sputtering target can be adjusted from 35 to 55 cm. Mass flow controller was used for controlling the amount of the flowing oxygen and argon gas, which was fixed at a value between 2 to 5 sccm. The sputtering rate of this system was around 200 nm per hour. BST powder ($Ba_{0.3}Sr_{0.7}TiO_3$, $Ba_{0.4}Sr_{0.6}TiO_3$ and $Ba_{0.5}Sr_{0.5}TiO_3$), which was manufactured by the Murata Manufacturing Co. Ltd., was used as a sputtering target. The Pt/BST/Pt parallel plate capacitors were built by sputtering with the top circular electrode that has a diameter of 0.1 mm.

### 2.2.2. Characterization of films

Dielectric behavior (dielectric constant and loss) was investigated as a function of frequency from 100 Hz to 10 MHz using an impedance analyzer (HP4194A) and probe station. The dielectric constant was calculated from the capacitance of a BST parallel plate capacitor. Then the tunability of a BST capacitor, which is defined as $[\varepsilon(0)-\varepsilon(V)]/\varepsilon(0)$ where$\varepsilon(0)$ is the dielectric constant at zero bias and $\varepsilon(V)$ is a dielectric

constant at V voltage, was examined by varying an external bias voltage from -20 to 20 V or -40 to 40 V. The ac oscillation level for the measurements was 0.1 V, because this yielded the greatest signal to noise ratio without suppressing the permittivity peak near zero bias. The crystalline structures, stoichiometric composition and surface morphologies were investigated through the measurement of X-ray Diffraction (XRD) analysis, X-ray Fluorescence (XRF) analysis and Field-Emission Scanning Electron Microscope (FE-SEM), respectively.

## 2.3 Results and discussions

### 2.3.1 Influence of the sputtering pressure on the crystallinity of the sputtered BST films

Figures 2-1 to 2-4 show the results of XRD $\theta$–$2\theta$ scans for BST deposited on a platinum/silicon substrate.

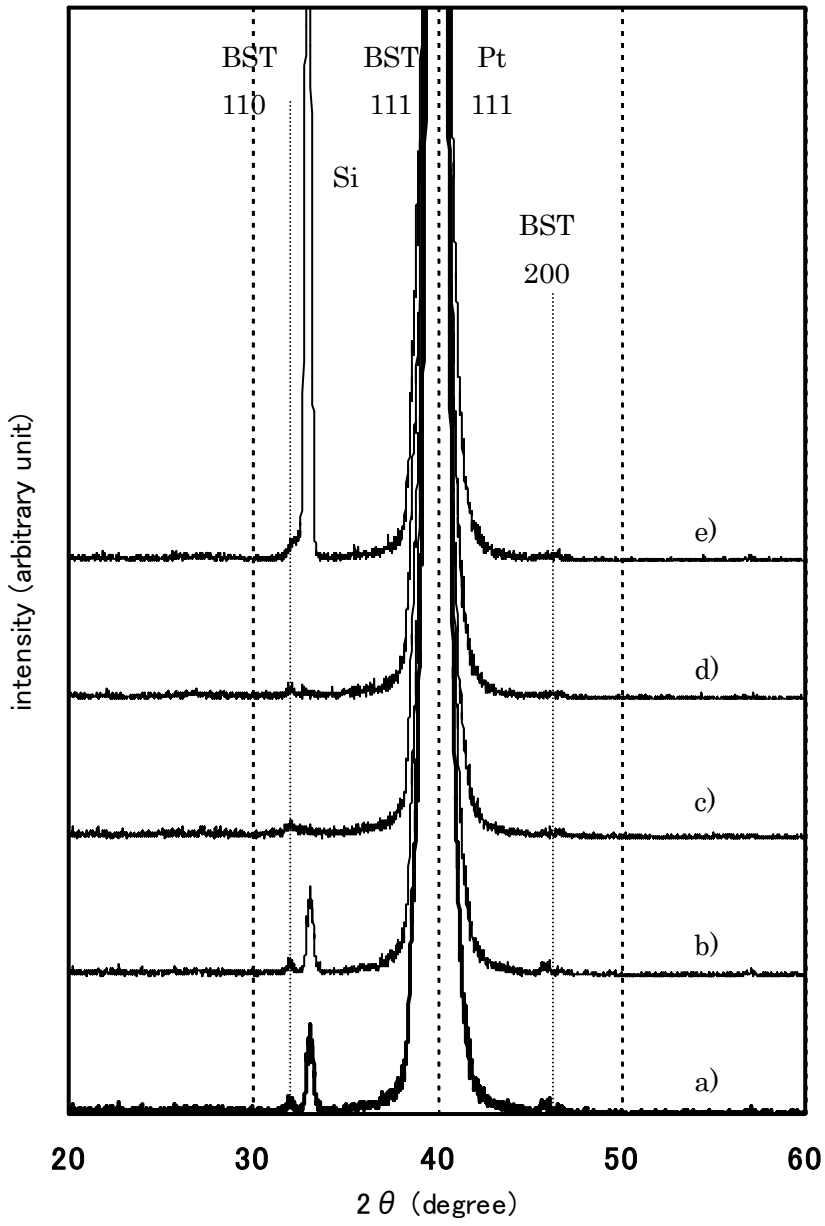


Figure 2-1 XRD pattern of BST (x=0.3) thin films. The sputtered gas pressures were 10, 20, 30, 40, 50mTorr for a), b), c), d), e), respectively. Deposition temperature was 600$^{o}$C.

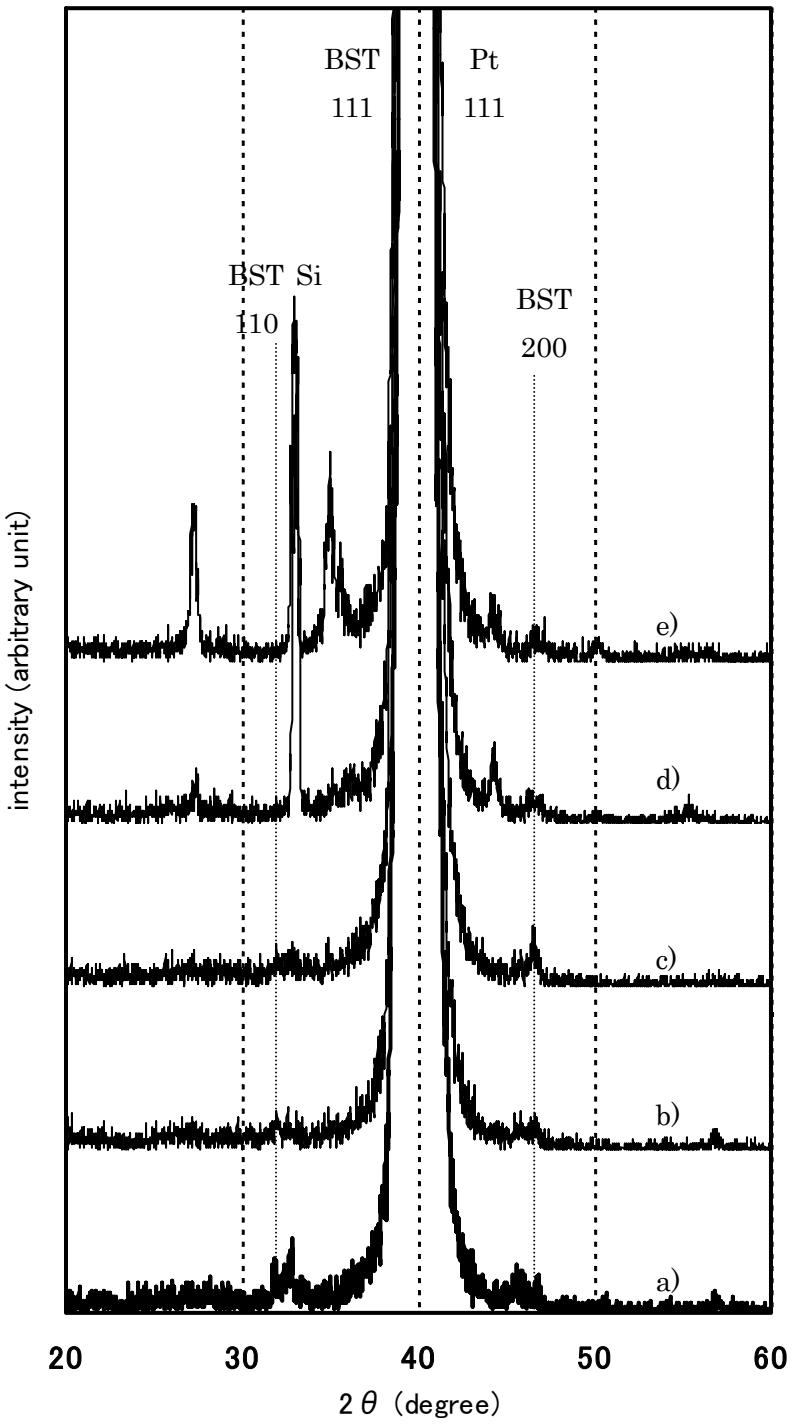


Figure 2-2　XRD pattern of BST (x=0.4) thin films. The sputtered gas pressures were 10, 20, 30, 40, 50mTorr for a), b), c), d), e), respectively. Deposition temperature was 600$^{o}$C.

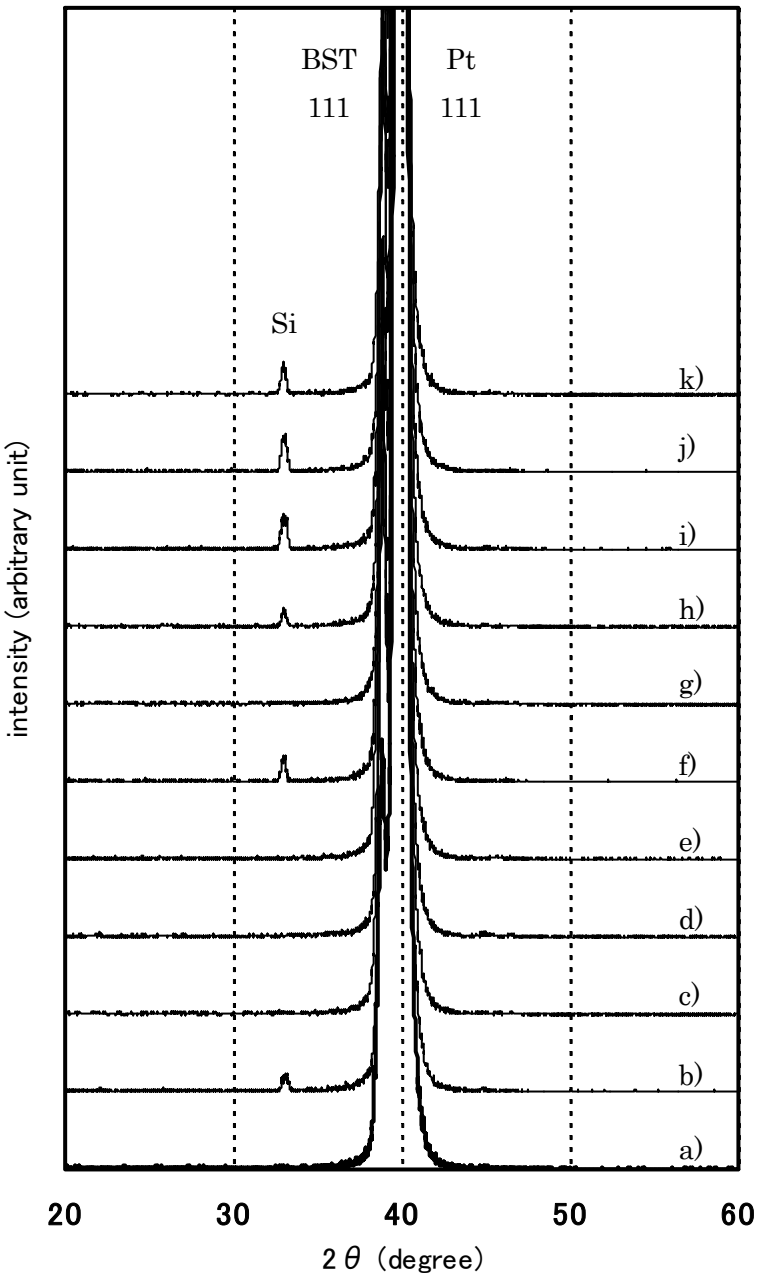


Figure 2-3　XRD pattern of BST (x=0.5) thin films. The sputtered gas pressure were 5, 10, 15, 20, 25, 30, 35, 40, 45, 50, 55mTorr for a), b), c), d), e), f), g), h), i), j), k), respectively. Deposition temperature was 500$^{o}$C.

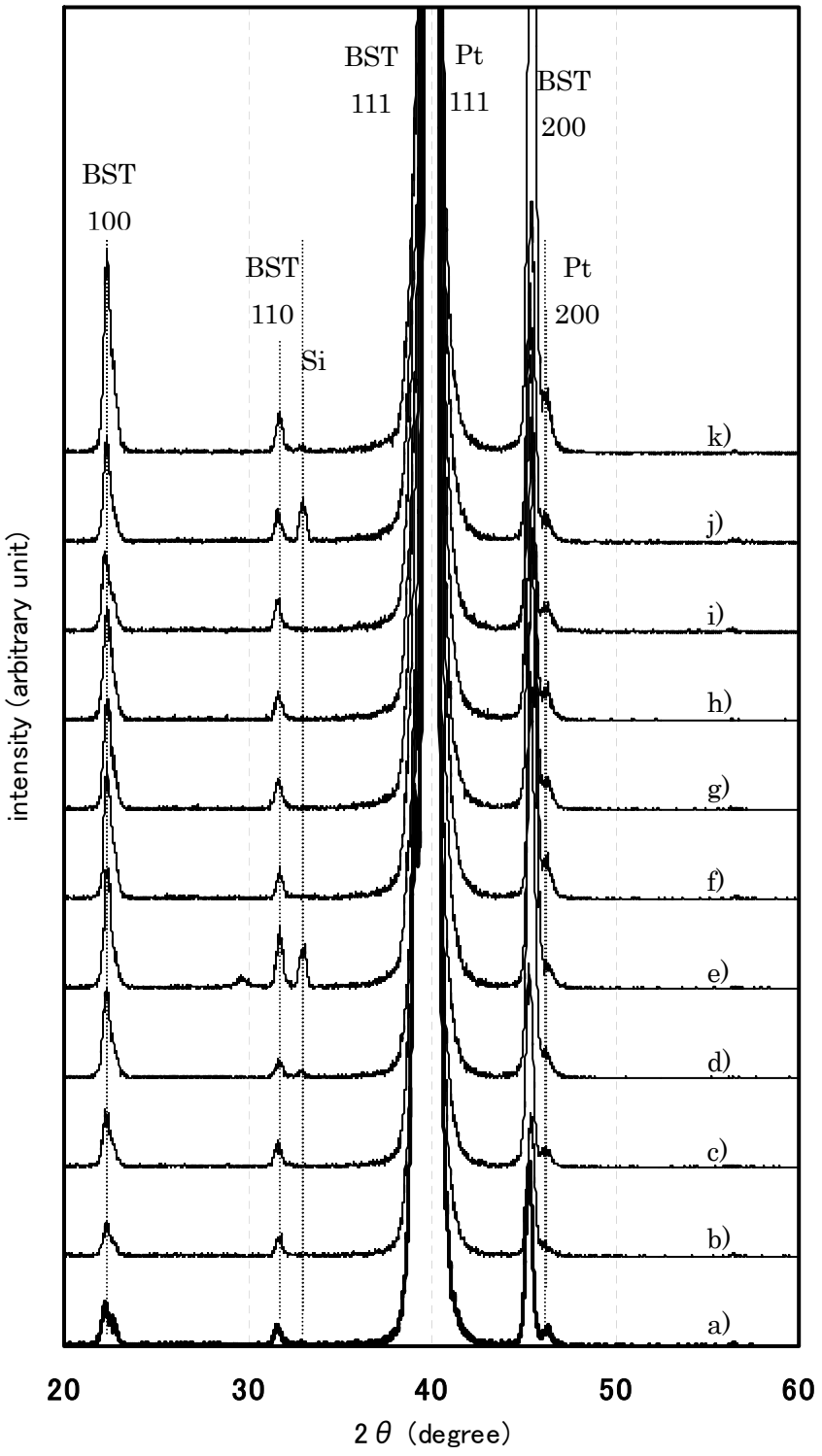


Figure 2-4　XRD pattern of BST (x=0.5) thin films. The sputtered gas pressure were 5, 10, 15, 20, 25, 30, 35, 40, 45, 50, 55mTorr for a), b), c), d), e), f), g), h), i), j), k), respectively. Deposition temperature was 600$^{o}$C.

The XRD peak found at $22^o$, $32^o$, $39^o$ and $46^o$ is the peak of the BST(100), BST(110), BST(111) and BST(200), respectively.

In the case of $Ba_{0.3}Sr_{0.7}TiO_3$ and $Ba_{0.4}Sr_{0.6}TiO_3$ , the film prefers random orientation and yield higher XRD counts at lower sputtering gas pressure, which implies good crystallinity. The weak BST(111) peaks were also observed by the conformal mapping method in XRD analysis. In the case of $Ba_{0.5}Sr_{0.5}TiO_3$, with substrate temperature $500^oC$ (Fig. 2-3), only BST(111) orientation was observed. The BST(111) peaks is stronger at all range of sputtering gas pressure. In the case of $Ba_{0.5}Sr_{0.5}TiO_3$, with substrate temperature $600^oC$ (Fig. 2-4), BST(111) peaks is strong at all range of sputtering gas pressure and BST(100) is stronger at higher sputtering gas pressure. There was no shift of the position of each BST peak, thus the lattice constant were rather constant, and not a function of sputtering gas pressure. Increase of substrate temperature from $500^oC$ to $600^oC$ results in random orientation with strong BST(111) and BST(100) orientation and is crucial if it is needed to obtained strong BST(100) orientation. Random orientation which occurred at higher substrate temperature, thus higher crystallization energy, may correspond to the cracks observed in these films as a result of relaxation of stress in film

### 2.3.2 Influence of the sputtering pressure on the surface morphology of the sputtered BST films

Figures 2-5 to 2-8 show the surface morphology of the BST deposited on a platinum/silicon substrate. In the case of $Ba_{0.3}Sr_{0.7}TiO_3$ (Fig. 2-5) and $Ba_{0.4}Sr_{0.6}TiO_3$ (Fig. 2-6), high density of fine spherical grains is observed in the case of low sputtering gas pressure. In the case of higher sputtering gas pressure, the films looks like powders because there is not enough energy to crystallized. As a result, the molecules accumulate together and form a polygonal shape before they can diffuse, leading to a porous structure.

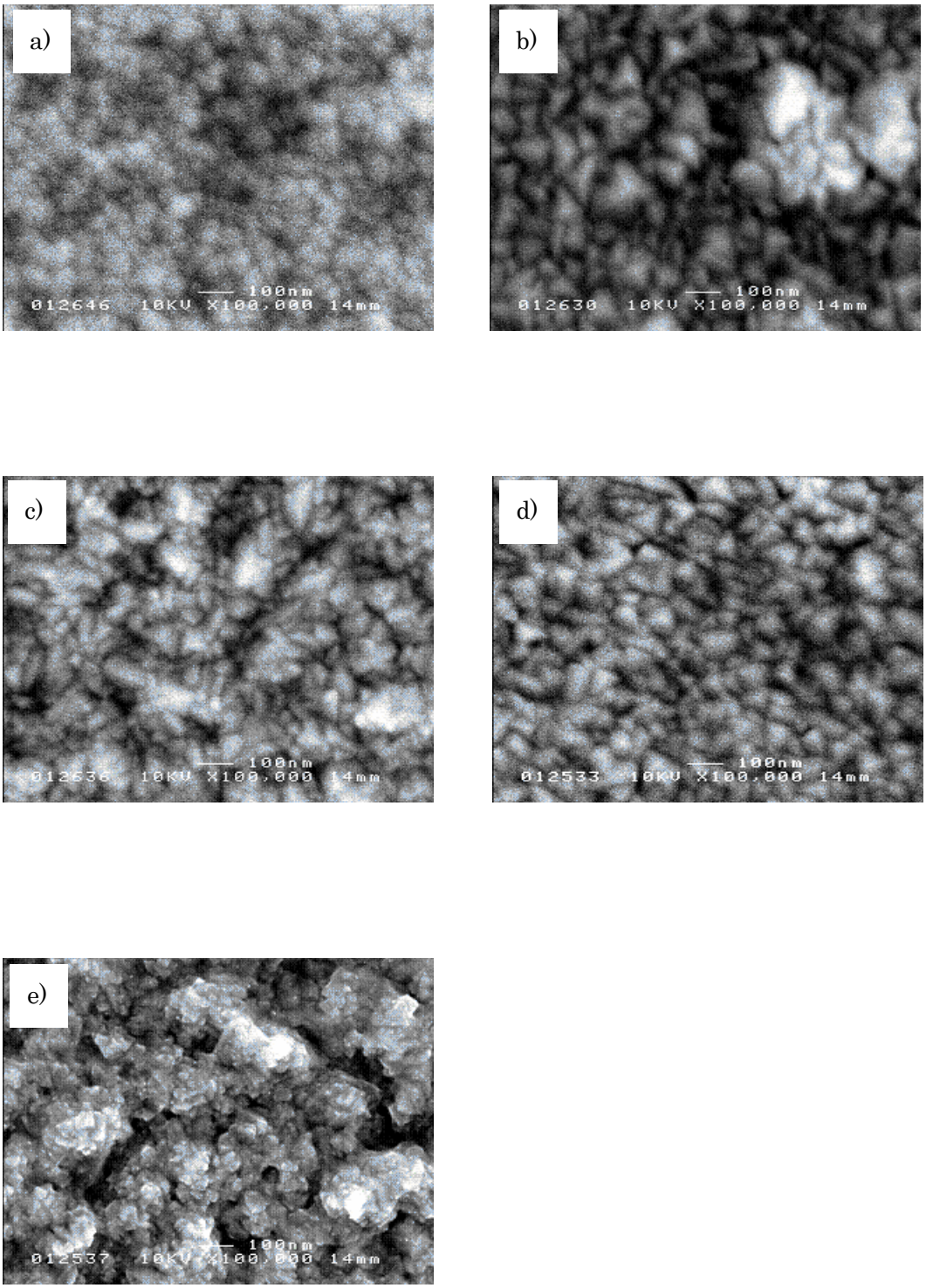


Figure 2-5 Surface morphology of BST (x=0.3) thin films observed by FE-SEM. The sputtered gas pressure were 10, 20, 30, 40, 50mTorr for a), b), c), d), e), respectively. Deposition temperature was 600$^{o}$C.

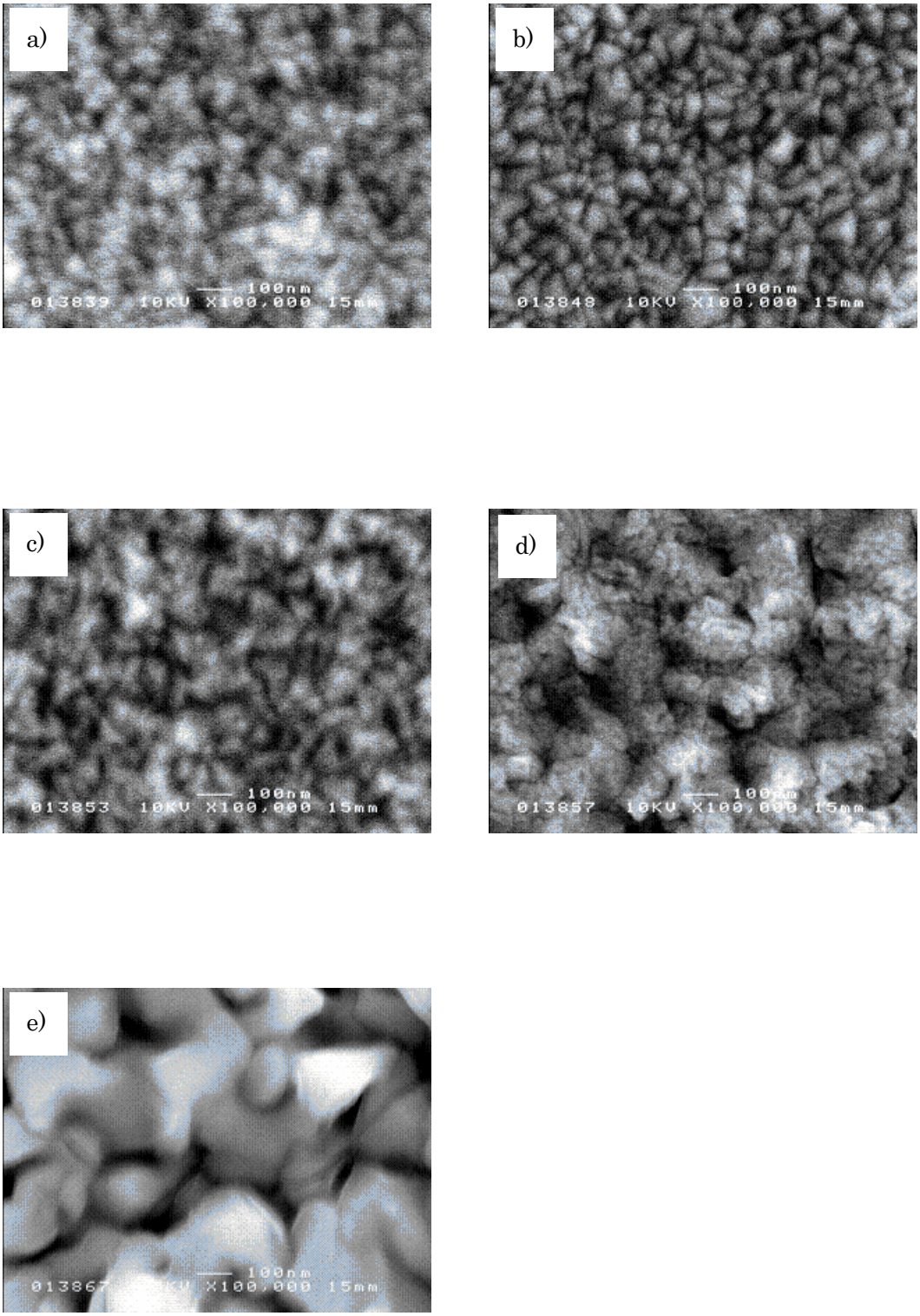


Figure 2-6 Surface morphology of BST (x=0.4) thin films observed by FE-SEM. The sputtered gas pressure were 10, 20, 30, 40, 50mTorr for a), b), c), d), e), respectively. Deposition temperature was 600$^{o}$C.

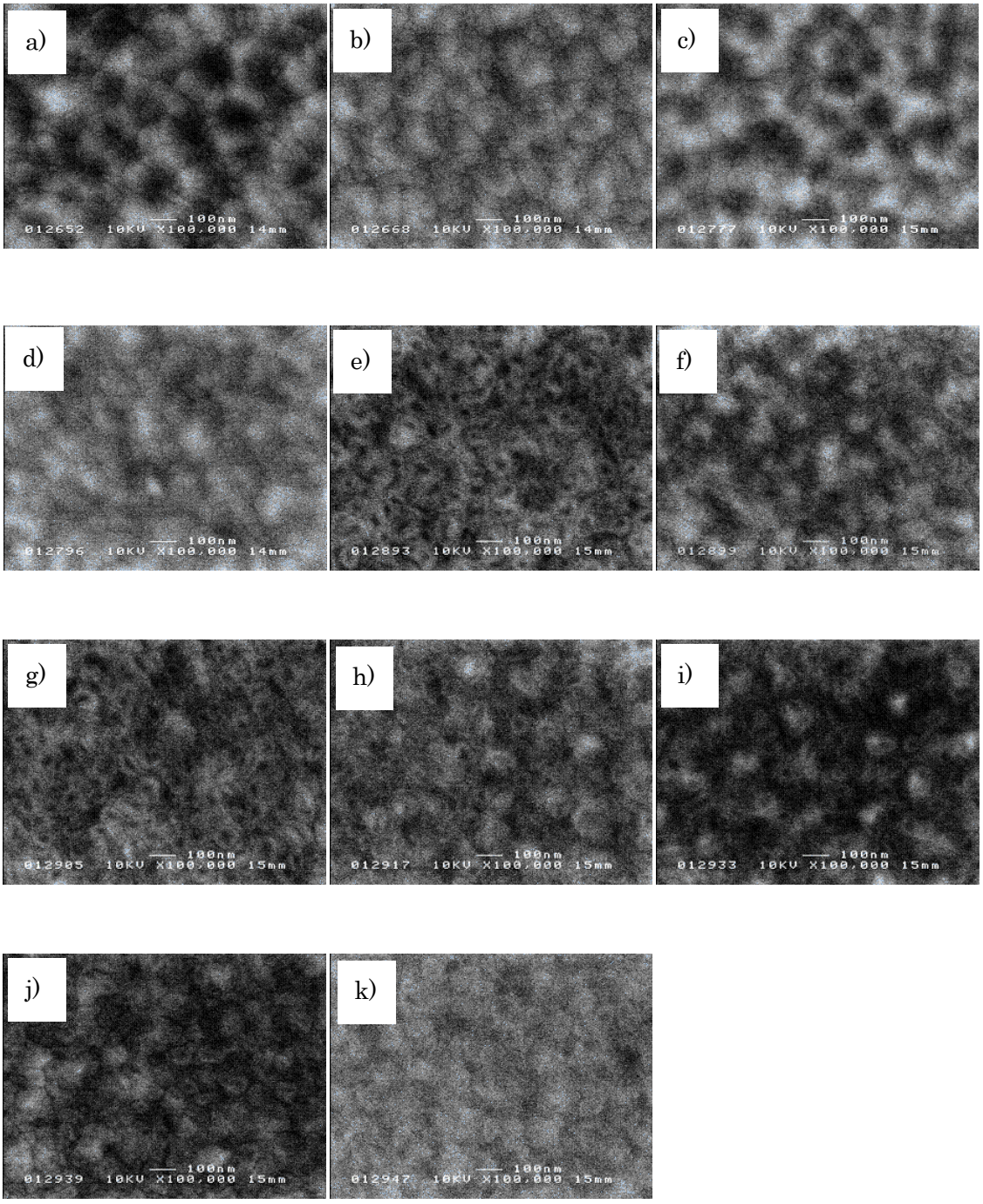


Figure 2-7 Surface morphology of BST (x=0.5) thin films observed by FE-SEM. The sputtered gas pressure were 5, 10, 15, 20, 25, 30, 35, 40, 45, 50, 55mTorr for a), b), c), d), e), f), g), h), i), j), k), respectively. Deposition temperature was 500$^{o}$C.

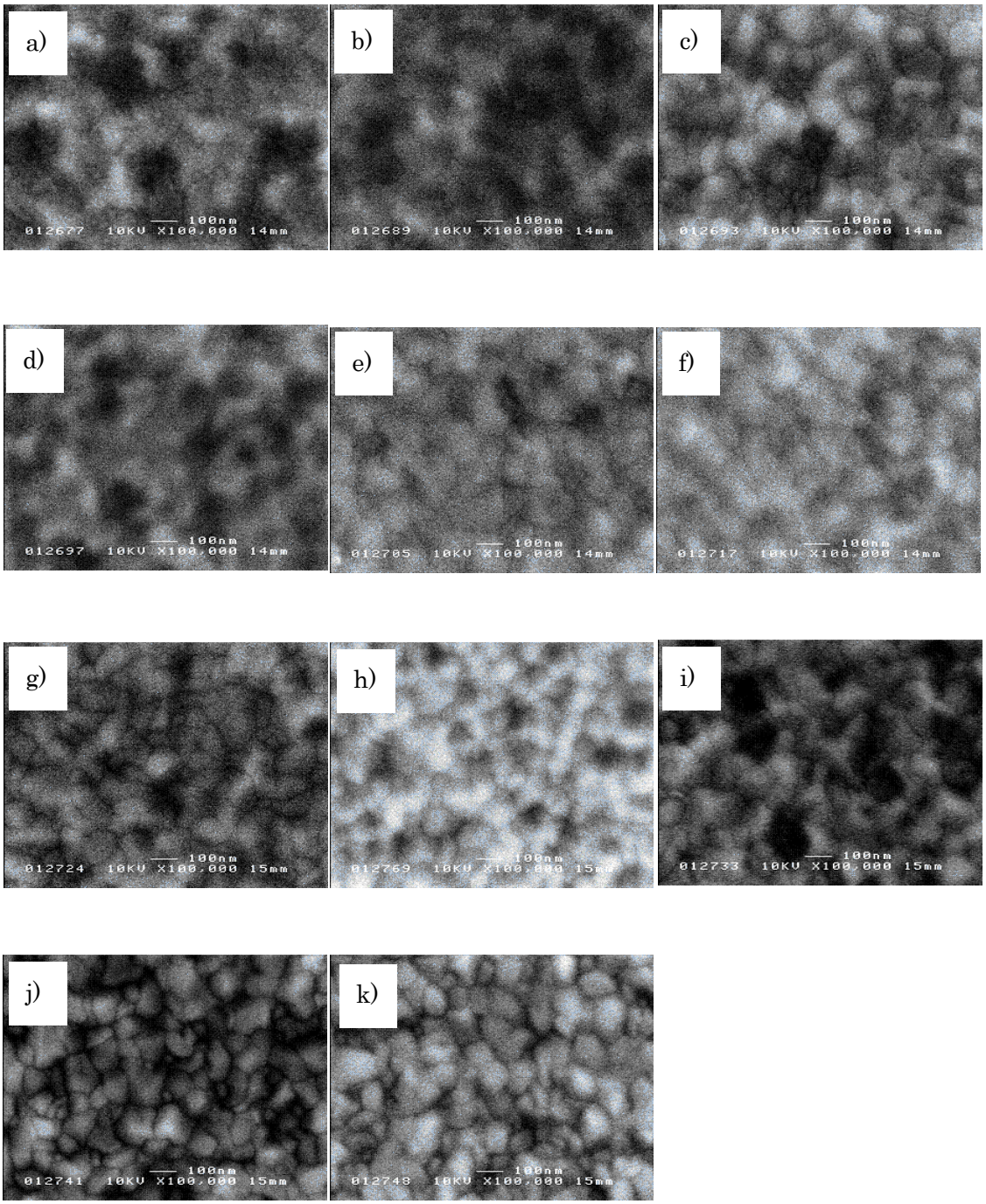


Figure 2-8　Surface morphology of BST (x=0.5) thin films observed by FE-SEM. The sputtered gas pressure were 5, 10, 15, 20, 25, 30, 35, 40, 45, 50, 55mTorr for a), b), c), d), e), f), g), h), i), j), k), respectively. Deposition temperature was 600$^{o}$C.

In the case of $Ba_{0.5}Sr_{0.5}TiO_3$, see Fig. 2-7and Fig. 2-8 Higher substrate temperature of 600$^oC$ (Fig. 2-8) helps the crystallization. At higher sputtering gas pressure, argon atoms loss more the energy while traveling in chamber, thus the sputtering rate is slower. Thus the surface of the films at higher sputtering gas pressure is smoother. From Fig. 2-8 j) and k), random size and shape of grains were observed. This is because when the deposition rate is slower, the molecules has time to diffuse and crystallize and thus the crystal structure is less dependent on the crystal structure of the substrate Pt(111). This corresponds to the result in last section (Fig. 2-4) where random orientations of BST x-ray peaks were observed by XRD.

### 2.3.3 Composition of the sputtered BST films

Due to the buffer layer of $TiO_2$ between platinum and silicon substrate, exact amount of Ti cannot be measured through XRF. However, it is possible to qualitatively determine the composition of the deposited BST films.

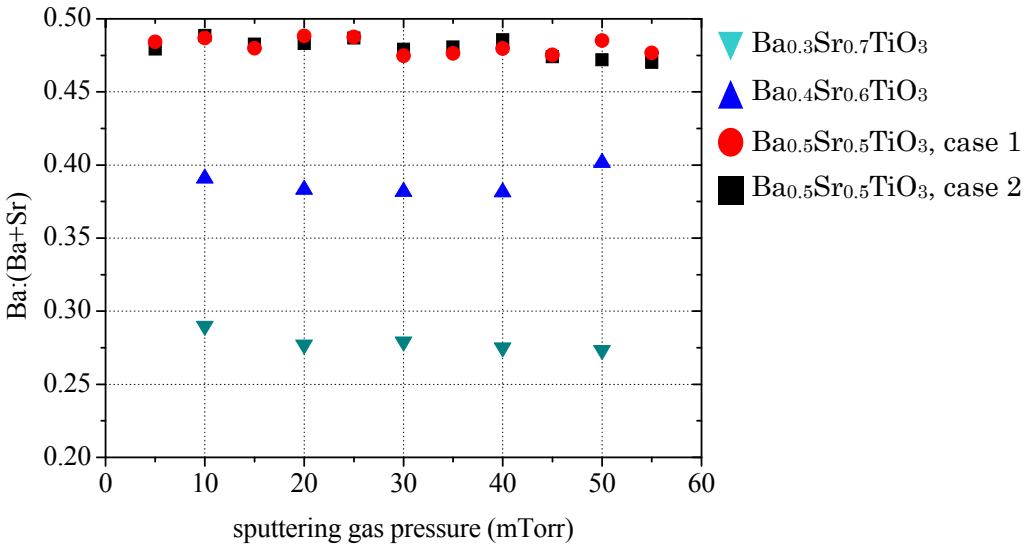


Figure 2-9 Atomic ratio of the barium atoms in the sputtered films. $Ba_xSr_{1-x}TiO_3$ (x=0.3, 0.4) were sputtered at 600°C. $Ba_xSr_{1-x}TiO_3$ (x=0.5) case 1 and case 2 are for deposition temperature of 600°C and 500°C,

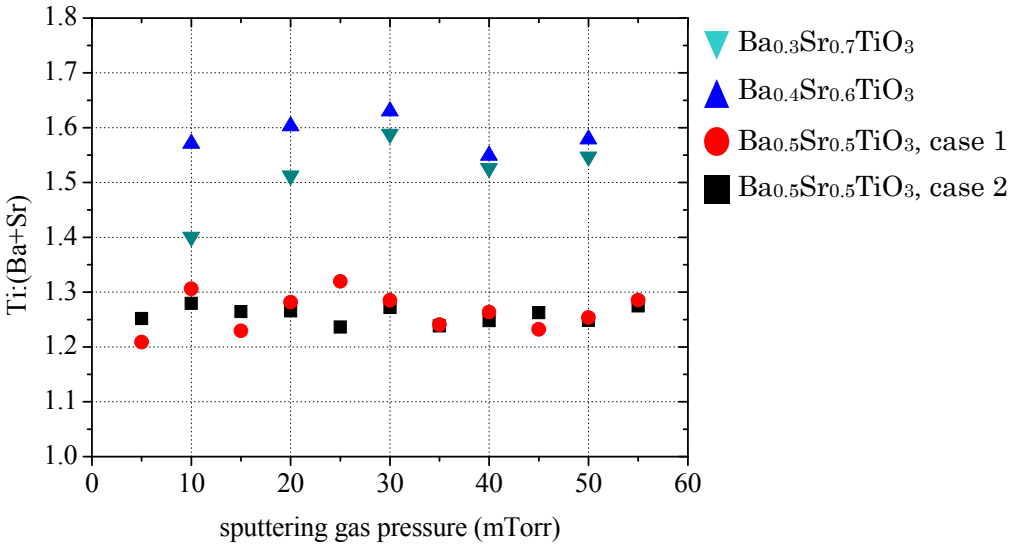


Figure 2-10 Atomic ratio of the titanium atoms in the sputtered films. $Ba_xSr_{1-x}TiO_3$ (x=0.3, 0.4) were sputtered at 600°C. $Ba_xSr_{1-x}TiO_3$ (x=0.5) case 1 and case 2 are for deposition temperature of 600°C and 500°C, respectively.

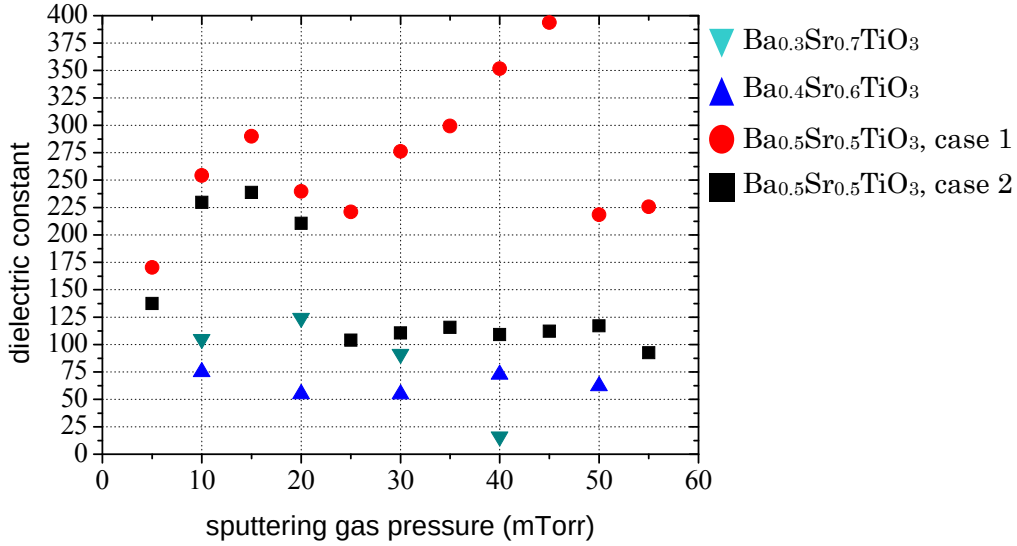


Figure 2-11 Dielectric constants of the sputtered films. $Ba_xSr_{1-x}TiO_3$ (x=0.3, 0.4) were sputtered at 600°C. $Ba_xSr_{1-x}TiO_3$ (x=0.5) case 1 and case 2 are for deposition temperature of 600°C and 500°C, respectively.

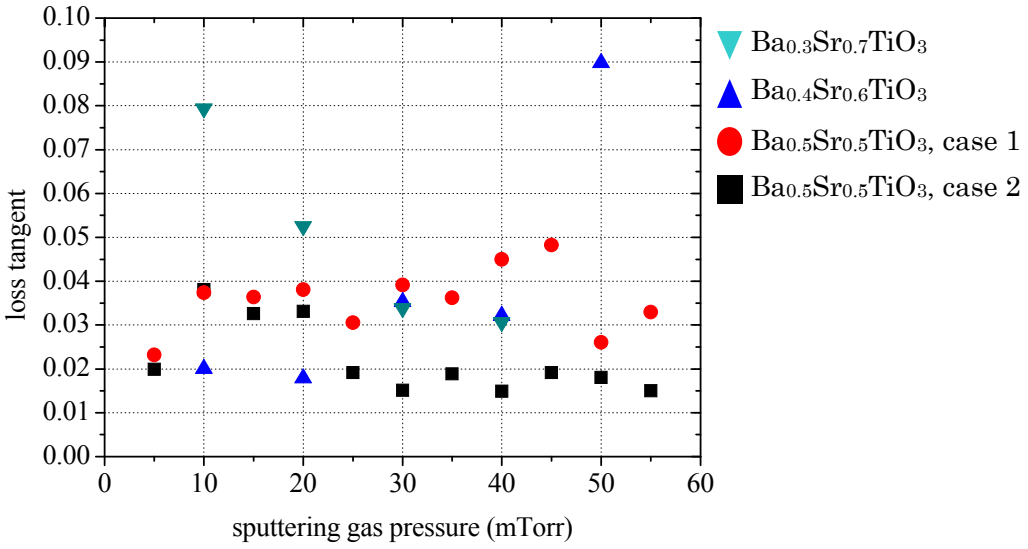


Figure 2-12 Loss tangent of the titanium atoms in the sputtered films. $Ba_xSr_{1-x}TiO_3$ (x=0.3, 0.4) were sputtered at 600°C. $Ba_xSr_{1-x}TiO_3$ (x=0.5) case 1 and case 2 are for deposition temperature of 600°C and 500°C, respectively.

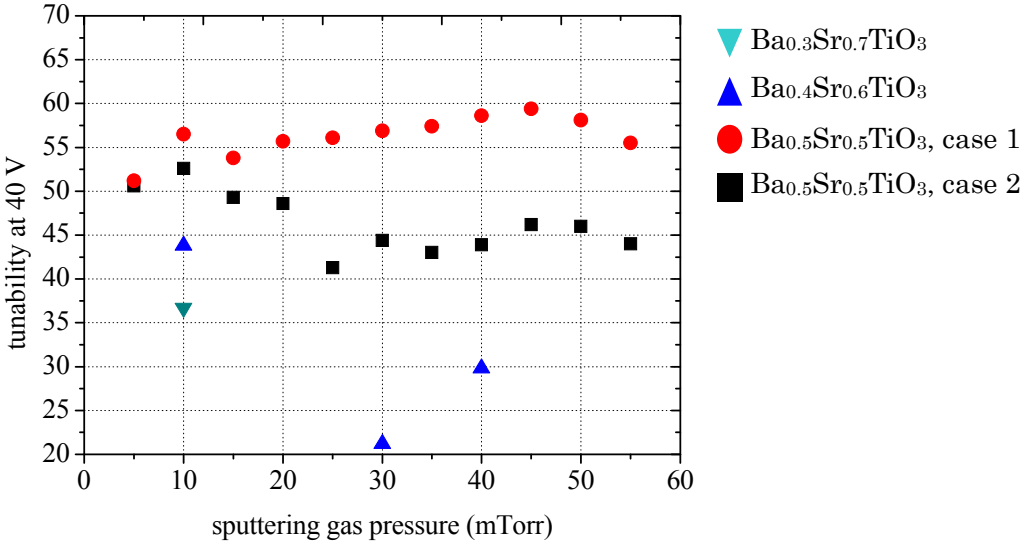


Figure 2-13 Tunability at 40 V, of the sputtered films. $Ba_xSr_{1-x}TiO_3$ (x=0.3, 0.4) were sputtered at 600°C. $Ba_xSr_{1-x}TiO_3$ (x=0.5) case 1 and case 2 are for deposition temperature of 600°C and 500°C, respectively.

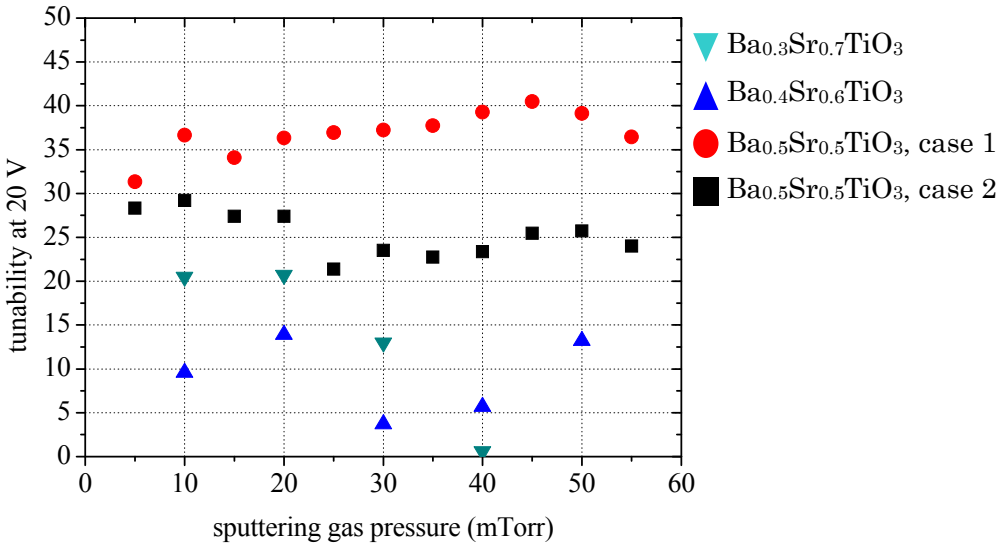


Figure 2-14 Tunability at 20 V of the sputtered films. $Ba_xSr_{1-x}TiO_3$ (x=0.3, 0.4) were sputtered at 600°C. $Ba_xSr_{1-x}TiO_3$ (x=0.5) case 1 and case 2 are for deposition temperature of 600°C and 500°C, respectively.

Figure 2-9 shows that there is a barium deficiency in the deposited films, and in the case of $Ba_{0.5}Sr_{0.5}TiO_3$, the composition of Ti (Fig. 2-10 is quite stable and is near stoichiometry. The barium deficiency is the result of lower sputtering yield of the barium atoms than that of the strontium and titanium atoms. The barium deficiency was observed in almost every film prepared by sputtering in this dissertation. In the case of $Ba_{0.5}Sr_{0.5}TiO_3$ films, the reason that the compoisition of Ti is independent of the sputtering gas pressure and near stoichiometry may be due to the fact the surface of these film, as discussed in the previous section, has almost no dense spherical grains, comparing to those $Ba_{0.3}Sr_{0.7}TiO_3$ and $Ba_{0.4}Sr_{0.6}TiO_3$ films. Thus the titanium atoms are not trapped in between the grain and may accumulate at the bottom layer of the BST films, thus assisting the crystallization of BST (111) which corresponds to the strong BST (111) x-ray peaks of Figs 2-3 and 2-4 .

### 2.3.4 Dielectric properties of the BST films

Figure 2-11 shows the dielectric constant of the BST films. Figures 2-12 show the dielectric loss of the BST films. Figures 2-13 and 2-14 show the tunability of the films at 40 V and 20 V, respectively. Some samples had a breakdown voltage lower than 40 V, therefore no data of those samples are available in the Fig. 2-13. The dielectric constant,

dielectric loss and tunability are constant trough the measured frequency range up to several MHz, and there are no dispersions observed. Finally, the sputtering conditions were optimized and the results are summarized in the Table 2-2.

Table 2-2 Summary of the dielectric properties of $Ba_xSr_{1-x}TiO_3$ (x=3, 4 ,5)

| | BST X=0.3 | BST X=0.4 | BST X=0.5 (500oC) | BST X=0.5 (600oC) |
|---|---|---|---|---|
| Loss tangent | 0.018 | 0.031 | 0.015 | 0.023 |
| Die. constant | 75 | 121 | 239 | 394 |
| Tunability (@20V) | 14 | 21 | 29 | 40.5 |
| Tunability (40V) | 44 | breakdown | 53 | 60 |
| Figure of merit | 598 | 405 | 1521 | 1439 |

### 2.3.5 Discussion

Tunability, dielectric constant and dielectric loss

BST film with highest tunability (58%) was obtained when the composition of $Ba_{0.5}Sr_{0.5}TiO_3$ was deposited at sputtering gas pressure of 45 mTorr, and the substrate temperature of 600$^{o}$C. The highest tunability is coincident with the highest dielectric constant and highest dielectric loss of the BST film.

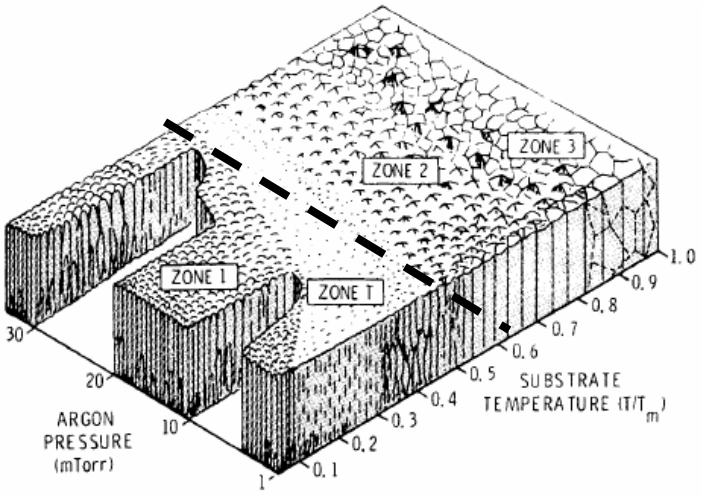


Figure 2-15 Typical surface morphology of the film surface after sputtering [36].

Figure 2-15 shows the typical surface morphology of the film deposited by the sputtering method. In zone T, the film has dense and fine grains. In zone 1, the film has too low energy to crystallize. In contrast, the zones 2 and 3 are where the film crystallizes so much and the grains become larger and the film surface becomes rough.

In this experiment, the film that possesses highest tunability is believed to be that in zone T in Fig. 2-15. The deposited films are considered to be explainable as expressed by a dot line in Fig. 2-15. That is, at low sputtering gas pressure, the films have surface

morphology that can be classified into zone 2. In this zone, the films are well crystallized and the grains are large, as can be seen in Fig. 2-8 a)-h). At high sputtering gas pressure, the films have surface morphology that can be classified into zone 1. In this zone, the films do not have enough energy to crystallize and the deposited particles may accumulate like powder (Fig. 2-8 j), k)). In this case, the orientation of the films becomes close to that of powders, which prefer 100 random orientations, which correspond to the results in XRD analysis (Fig. 2-8).

The high dielectric constants are coincident with high tunability. Theoretical explanation that high dielectric constant is coincident with high tunability was already described in the equations (2-1)-(2-6). The experimental explanation for this is believed to be due to high polarizations in the well crystallized film and large grain size.

High dielectric losses are also coincident with high tunability, but are found to be more highly dependent on the substrate temperature during film deposition, rather than deposition gas pressure. Figure 2-12 shows the dielectric losses of the BST films. $Ba_{0.5}Sr_{0.5}TiO_3$ films that were deposited at 500$^{o}$C have the dielectric losses of approximately 2%, which is half of the value of that in the films which were deposited

at 600°C. Moreover, there are no 100 XRD peaks in the $Ba_{0.5}Sr_{0.5}TiO_3$ films that were deposited at 500°C, and the films are purely 111 oriented. In contrast, the $Ba_{0.5}Sr_{0.5}TiO_3$ films that were deposited at 600°C have 100 random orientations, which resemble the BST powder. In this case, the low dielectric losses are believed to be due to the films being single oriented. And the high dielectric losses are believed to be due to the random orientations of the films.

Ti-excessive

For BST with excessive Ti and O atoms, the composition of the BST is expressed as $Ba_xSr_{1-x}Ti_{1+y}O_{3+z}$. In this case, solubility of excess Ti in bulk BST is approximately $y$<0.001 [10]. However, reasonable performance of BST (x=0.7) can be found up to y=0.15 [11].

Ti adhesion or surface layers have been shown to promote epitaxial growth on (111) Pt grains for other perovskite films [14–17]. Tani *et al.* reported a change from (100) to (111) texture in $(Pb,Zr)TiO_3$ thin films, if Ti from the adhesion layer migrated to the electrode surface [17]. Although it is well known that Ti diffuses through Pt electrodes,

[18–21] the precise mechanisms by which Ti underlayers control perovskite thin film textures are not fully understood. In the literature, it has been suggested that either a Pt–Ti intermetallic or $TiO_2$ on the Pt surface provide a templating layer for (111) epitaxial perovskites growth. [14,17]. Furthermore, (111) oriented epitaxial $SrTiO_3$ thin films showed a much more pronounced thickness dependence of their permittivity than (110) oriented films. [22] This thickness dependence is commonly modeled by an interfacial capacitance with a lower permittivity than the "bulk" of the film, [6, 23] but its origins are not understood.

Sputtering condition that results in Ti-rich BST films

Most of the films fabricated in this thesis are titanium-rich. In this thesis, during the film deposition by sputtering, it was found that the BST films possessed more Ti-excessive composition when:

(i) The target-to-substrate spacing is short (35 mm). The stoichiometry of the films was improved when the target-to-substrate spacing is longer (45 mm and 55 mm).

(ii) The sputtering temperature is low (500$^{o}$C). The sputtering temperature in this thesis

was in the range from 500°C to 650 °C. Susanne *et al*, investigate the BST (x=0.7) films (deposited by MOCVD method) by an electron energy-loss spectroscopy (EELS), and suggested that, when the films are deposited at low temperature, there may be the accommodation of excess titanium in the grain interior. The grain boundary area in the BST films is larger than that in much larger grain in bulk ceramics; therefore the excess titanium amount well beyond the bulk solid solubility can be tolerated. It appears to be a general feature in these materials that Ti maintains its octahedral coordination at grain boundaries, even in cases where Ti is thought to segregate to the boundaries [21].

(iii) When the sputtering gas pressure was high.

(iv) When the oxygen to argon gas ratio ($O_2$:Ar) during the sputtering was high.

2. Ba-deficient

Barium-atom deficiency is crucial in the BST films because it linearly and strongly decrease the lattice constant of the BST unit cell, and thus reduce the value of Curie temperature, which dominates the permittivity, tunability and dielectric loss of the BST films.

Sputtering condition that results in Ba-deficient BST films

Unlike other reported papers [25], the films deposited in this study tend to be Ba-deficient when the gas pressure is high or oxygen amount is high.

(i) The target-to-substrate spacing is short (35 mm). The stoichiometry of the films was improved when the target-to-substrate spacing is longer (45 mm and 55 mm). This is believed to be caused by the higher resputtering rate.

(ii) The temperature is low.

(iii) The sputtering gas pressure was high.

## References


1) Troy R. Taylor, "Stoichiometry and Thermal Mismatch Effects on Sputtered Barium Strontium Titanate Thin Films", University of California (Santa Barbara), Ph.D. thesis, (2003)

2) R. Waser, Integrated Feeroelectrics **15**, 39, (1997) 39

3) A. K. Tagantsev, V. O. Sherman, K. F. Astafiev, J. Vankatesh, N. Setter, "Ferroelectric Materials for Microwave Tunable Applications", Journal of Electroceramics **11** (2003) 5

4) L. A. Wills, T. Schmitz, T. Reyes, and J. Amano, Integrated Ferroelectrics **21** (1998) 429

5) M. Yamamuka, T. Kawahara, A. Yuuki, and K. Ono, "Reaction Mechanism and Electrical Properties of (Ba,Sr)$TiO_3$ Films Prepared by Liquid Source Chemical Vapor Deposition", Japanese Journal of Applied Physics, **35** (1996) 2530

6) J. A. Thornton, Journal of Vacuum Science Technology, **15** (1978) 171

7) M. J. Akhtar, Z. U. N. Akhtar, R. A. Jackson, and C. R. A. Catlow, Journal of American Ceramics, **78**, (1995) 421

8) N. H. Chan, R. K. Sharma, and D. M. Smyth, **"**Nonstoichiometry in undoped

$BaTiO_3$", Journal of Electrochemistry Society, **128** (1981) 1762

9) A. Akimov, A.A. Sirenko, A.M. Clark, J.H. Hao and X.X. Xi, "Electric-Field-Induced Soft-Mode Hardening in $SrTiO_3$ Films", Physical Review Letters **84** (20) (2000) 4625

10) D. A. Tenne, A. Soukiassian, X.X. Xi, H. Choosuwan, R. Guo and A.S. Bhalla, "Lattice dynamics in $BaSrTiO_3$ single crystals: A Raman study", Physical Review B **70** (2004) 174302

11) D. A. Tenne, A. Soukiassian, X.X. Xi, H. Choosuwan, R. Guo and A.S. Bhalla, "Lattice dynamics in $BaSrTiO_3$ thin films studied by Raman spectroscopy", Physical Review B **70** (2004) 174302

12) P. Kuzel, F. Kadlec, H. Nemec, R. Ott, E. Hollmann and N. Klein, "Dielectric tunability of SrTiO3 thin films in the terahertz range", Journal of Applied Physics **96** 11 (2004) 6597

13) J. M. Wesselinowa amd St. Kovachev, "Hardening and softening of soft phonon modes in ferroelectric thin films", Physical Review B **75** (2007) 045411

14) J.M. Worlock and P.A. Fleury, "Electric field dependence of Optical-phonon frequencies", Physical Review Letters **19** (1967), 1176

15) P.A. Fleury and J.M. Worlock, "Electric-field-induced Raman effect in Paraelectric

crystals", Physical Review Letters **18** (1967) 665

16) E.J. Cukauskas, Steven W. Kirchoefer, William J. Desisto and Jeffrey M. Pond, "$Ba_{(1-x)}Sr_xTiO_3$ thin films by off-axis cosputtering $BaTiO_3$ and $SrTiO_3$" Applied Physics Letters **74** 26 (1999) 4034

17) Nicholas H. Finstrom , John A. Gannon, Nadia K. Pervez, Robert A. York and Susanne Stemmer, "Dielectric losses of SrTiO3 thin film capacitors with Pt bottom electrodes at frequencies up to 1 GHz" Applied Physics Letters **89** (2006) 242910

18) S.V. Razumov, A.V. Tumarkin, M.M. Gaidukov, A.G. Gagarin, A.B. Kozyrev, O.G. Vendik, A.V. Ivanov, O.U. Buslov and V.N. Keys, "Characterization of quality of $Ba_xSr_{1-x}TiO_3$ thin films by the commutation quality factor measured at microwaves" Applied Physics Letters **81** 9 (2002) 1675

19) B.A. Baumert, L.H. Chang, A.T. Matsuda, T.L. Tsai, C.J. Tracy, R.B. Gragory, P.L. Fejes, N.G. Cave, W. Chen, D.J. Taylor, T. Otsuki, E. Fujii, S. Hayashi and K. Suu, "Characterization of sputtered barium strontium titanate and strontium titanate-thin films" Journal of Applied Physics **82** 5 (1997) 2558

20) D.Y. Noh, H.H. Lee. T.S. Kang and J.H. Je, "Crystallization of amorphous (BA,Sr)$TiO_3$/MgO(001) thin films" Applied Physics Letters **72** 22 (1998) 2823

21) U.C. Oh, T.S. Kang, K.H. Park and J.H. Je, "Effects of plasma power on the

epitaxial growth of $(Ba_{0.48}Sr_{0.52})TiO_3$ thin film" Journal of Applied Physics **86** 1 (1999) 163

22) Ju Cheol Shin, Jaehoo Park, heol Seong Hwang and Hyeong Joon Kim, "Dielectric and electrical properties of sputter grown $(Ba,Sr)TiO_3$ thin films" Journal of Apllied Physics, **86** 1 (1999) 506

23) P. Padmini, T.R. Taylor, M.J. Lefevre, A.S. Nagra, R.A. York and J.S. Speck, "Realization of high tunability barium strontium titanate thin films by rf magnetron sputtering" Applied Physics Letters **75** 20 (1999) 3186

24) Jaemo Im, O. Auciello, P.K. Baumann, S.K. Streiffer, D.Y. Kaufman and A.R> Krauss, "Composition-control of magnetron-sputter-deposited $(Ba_xSr_{1-x})Ti_{1+y}O_{3+z}$ thin films for voltage tunable devices" Applied Physics Letters **76** 5 (2000) 625

25) Byoung Taek Lee and Cheol Seong Hwang, "Influence of interfacial intrinsic low-dielectric layers on the dielectric properties of sputtered $(Ba,Sr)TiO_3$ thin films" Applied Physics Letters **77** 1 (2000) 124

26) Matthew C. Werner, Indrajit Banerjee, Paul C. McIntyre, Noriaki Tani and Michio Tanimura, "Microstructure of $(Ba,Sr)TiO_3$ thin films deposited by physical vapor deposition at 480 $^oC$ and its influence on the dielectric properties" Applied Physics Letters **77** 8 (2000) 1209

27) E.J. Cukauskas, Steven W. Kirchoefer and Jeffrey M. Pond, “Low-loss $Ba_{0.5}Sr_{0.5}TiO_3$ thin films by inverted cylindrical magnetron sputtering” Journal of Applied Physics **88** 5 (2000) 2830

28) S. Stemmer, T. Hoche, R. Keidng, C. Russel, R. Schneider, N.D. Browning, S.K. Streiffer and H.J. Kleebe, “Oxidization states of titanium in bulk titanates and in (100) fiber-textured $(Ba_xSr_{1-x})Ti_{1+y}O_{3+z}$ thin films” Applied Physics Letters **79** 19 (2001) 3149

29) Yu. I. Yuzyuk, V.A. Alyoshin, I.N. Zakharchenko, E.V. Sviridov, A. Almeida and M.R. Chaves, “Polarization-dependent Raman spectra of heteroepitaxial (Ba,Sr)$TiO_3$/MgO thin films” Physical Review B **65** (2002) 134107

30) Tae-Gon Kim, Jeongmin Oh, Yongjo Kim, Taeho Moon, Kug Sun Hong and Byungwoo Park, “Crystallinity dependence of microwave dielectric properties in (Ba,Sr)$TiO_3$ thin films” Japanese Journal of Applied Physics **42** (2003) 1315

31) Ivoyl P. koutsaroff, Thomas A. Bernacki, Marina Zelner, Andrew Cervin-Lawry, Takehito Jimbo and Koukou Suu, “Characterization of thin-film decoupling and high-frequency (Ba,Sr)$TiO_3$ capacitors on $Al_2O_3$ ceramic substrates” Japanese Journal of Applied Physics **43** 9B (2004) 6740

32) Tianjin Zhang, Songzhan Li, Baishun Zhang, Ruikun Pan, Juan Jiang and Weihua

Huang, “Microstructure and optical properties of $Ba_{0.65}Sr_{0.35}TiO_3$ thin films prepared by rf magnetron sputtering” Japanese Journal of Applied Physics **44** 12 (2005) 8599

33) J.Y. Kim and A.M. Grishin, “Processing and on-wafer test of ferroelectric film microwave varactors” Applied Physics Letters **88** (2006) 192905

34) Baishun Zhang, Zui Quan, Tianjin Zhang, Tao Guo and Shaobo Mo, “Effect of oxygen gas and annealing ttreatment for magnetically enhanced reactive ion etched $(Ba_{0.65}Sr_{0.35})TiO_3$ thin films” Journal of Applied Physics **101** (2007) 014107

35) E.A. Fardin, A.S. Holland, K. Ghorbani and P. Reichart, “ Enhances tunabikity of magnetron sputtered $Ba_{0.5}Sr_{0.5}TiO_3$ thin films on c-plane sapphire substrates” Applied physics Letters **89** (2006) 022901

36) J.A. Thornton, Journal of Vacuum Science and Technology **11**, (1974) 666

# Chapter 3. Dependence of microwave properties of the $(Ba_{0.5}Sr_{0.5})TiO_3$ films on substrate

This chapter shows the results of the phase shift in the coplanar waveguide structure on BST films on different substrates, which happened as a result of the decreased permittivity after applied an external voltage bias. The phase of a microwave signal in the waveguide changed corresponding to the change of the permittivity of solely BST films, not the substrates. The high crystalline quality of the epitaxial BST film was found to be necessary for achieving high tunability and low dielectric loss.

## 3.1 Introduction

### 3.1.1 Measurement techniques at microwave frequency for thin ferroelectric films

In this part, the methods and techniques that enable the measurement of the permittivity, tunability and dielectric loss of ferroelectric materials are briefly described. All measurement techniques require two steps. First, the electrical characteristic of the device containing the ferroelectric films is monitored. Second, the dielectric permittivity,

tunability and dielectric loss of the material are evaluated from the obtained results. Thus, the determination of the properties of ferroelectric thin films can be separated into two parts: measurement and evaluation.

All measurement methods can be divided into three groups [1]:

- *direct methods* where the capacitance and dielectric loss of a capacitor containing the investigated material are measured directly by using an impedance analyzer.

- *waveguide methods* in which the scattering matrix of the ferroelectric containing waveguide is measured using a network analyzer.

- *resonance methods* where the characteristics of a ferroelectric containing resonator is measured.

For frequencies below some tens or hundreds of megahertz (radio frequencies), the tunable capacitor which is made of ferroelectric material is regarded as a lumped element because its dimensions are much less than the wavelength of the electromagnetic signal. The capacitance and dielectric loss of the capacitor can be measured directly by a standard impedance analyzer.

At higher frequencies, the dimensions of the capacitors become comparable with the

length of the electromagnetic wave and they cannot be considered any more as lumped elements. Moreover, the impedance of the capacitors becomes very small in comparison to the resolution of the impedance analyzer. Thus, these methods are to be replaced by waveguide methods or resonance methods. In the case of measuring a tunable ferroelectric film, the resonance methods cannot be used as it is difficult to apply an external DC voltage bias to the films during measurement. Moreover, the resonance methods only allow the measurement results at some specific frequencies.

All sources of the errors appearing in different characterization techniques can be divided into measuring errors and evaluation errors. The relative instrument error of the instruments is below than 1-2% and depends on the quality of calibration and calibrating standards. Table 3-1 contains the measurement precisions and limitation for the different measuring techniques.

Table 3-1 Basic measurement errors and limits of the different characterization techniques, $\omega$C is the reactance of the ferroelectric capacitor [1].

| Methods | Instrument errors | Limits |
|---|---|---|
| Direct capacitor measurements | | |
| Capacitance | 0.05-0.1% | 10-17<C[f]<10 |
| Loss tangent | 0.0005-0.001% | 10-6<tand<10 |
| | | F[Hz]<106-108 |
| Capacitor measurement by measuring the reflection coefficient | 2-5% | 0.005<ωC<0.05 |
| Capacitance | 5-6% | [1/Ω] |
| Loss tangent | | 0.0005<ωCtand<0.02 |
| | | [1/Ω] |
| Waveguide and transmission line method | <5 degree | f[GHz]>0.5 |
| Absolute error of the phase | <0.02 | $20^o$ <electric length< $160^o$ |
| Absolute error for the transmission-coefficient | | |
| Resonance methods | | |
| Capacitance or dielectric permittivity | <1% | 10-4-10-2 <tand<0.1 |
| Loss tangent | ~5% | 0.05<C[pF]<1 |

In the following, a discussion of dielectric measurement at GHz region using on-wafer TRL calibration method is presented. The basic principle of operation of the coplanar waveguide line in measuring BST thin films` dielectric properties at GHz region and the

relevant design equations are summarized.

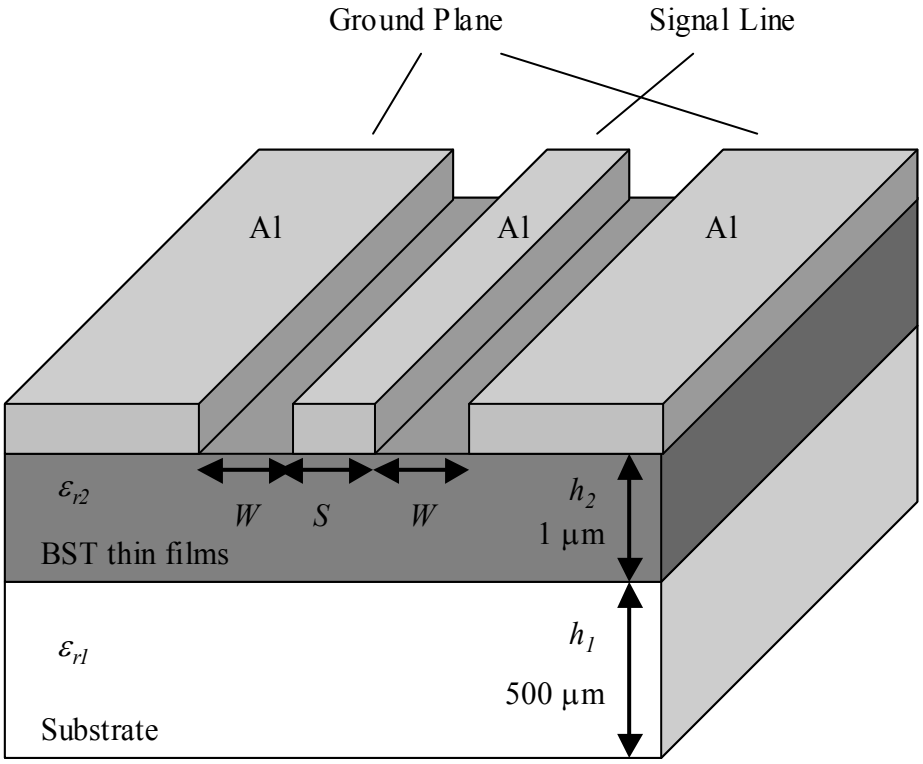


Figure 3-1 Coplanar waveguide structure on BST films and dielectric substrate multilayer.

From figure 3-1, if the substrate is multilayered the closed form formula derived by conformal mapping method is;

$$k_0 = \frac{S}{S+2W} \tag{3-1}$$

$$k_1 = \frac{\sinh(\pi S/4h_1)}{\sinh(\pi(S+2W)/4h_1)} \tag{3-2}$$

$$k_2 = \frac{\sinh(\pi S/4h_2)}{\sinh(\pi(S+2W)/4h_2)} \tag{3-3}$$

$$q_i = \frac{1}{2}\frac{K(k_i)}{K'(k_i)}\frac{K'(k_0)}{K(k_0)} \qquad i = 1,2 \tag{3-4}$$

$$\varepsilon_{eff} = 1 + q_1(\varepsilon_{r1} - 1) + q_2(\varepsilon_{r2} - \varepsilon_{r1}) \tag{3-5}$$

$$Z_c = \frac{30\pi}{\sqrt{\varepsilon_{re}}} \frac{K'(k_0)}{K(k_0)} \tag{3-6}$$

where,

$h_1$ is substrate thickness,

$h_2$ is film thickness,

$\varepsilon_{r1}$ is a relative dielectric constant of the substrate,

$\varepsilon_{r2}$ is a relative dielectric constant of the film,

$\varepsilon_{eff}$ is an effective dielectric constant of the dielectric/substrate multilayer.

$K(x)$ is the elliptic integral of first kind, $K'(x) \equiv K\left(\sqrt{1-x^2}\right)$,

$Z_c$ is an impedance of the line

$k_1$, $k_2$, $q_1$ and $q_2$ are constants.

In this thesis, S(=10-30μm),W(=10-30μm) >> $h_1$(=200-1000nm), thus the value of $k_2$($<10^{-51}$) becomes too small and leads to numerical error in calculating elliptic function K/K'. This error can be overcome by using asymtotic formula for the ratio of K/K';

$$\frac{K(k)}{K'(k)} = \frac{\pi}{\ln\left[\frac{2\left(1+\sqrt[4]{1-k^2}\right)}{1-\sqrt[4]{1-k^2}}\right]} \tag{3-7}$$

for 0<k<0.707 ;

$$\frac{K(k_2)}{K'(k_2)} = \frac{\pi}{\ln\left[\frac{2\left(1+\sqrt[4]{1-k_2^2}\right)}{1-\sqrt[4]{1-k_2^2}}\right]} \approx \frac{\pi}{\ln\left[\frac{16}{k_2^2}\right]} \tag{3-8}$$

Therefore, in BST thin film region, we use equation (3.9) instead of using equation (3.4);

$$q_2 = \frac{1}{2}\frac{\pi}{\ln\left[\frac{16}{k_2^2}\right]}\frac{K'(k_0)}{K(k_0)} \tag{3-9}$$

Table 3-2 Simulation parameter

| | BST | Substrate |
|---|---|---|
| Dielectric Constant | 500 | 10 |
| Thickness | 1μm | 500μm |

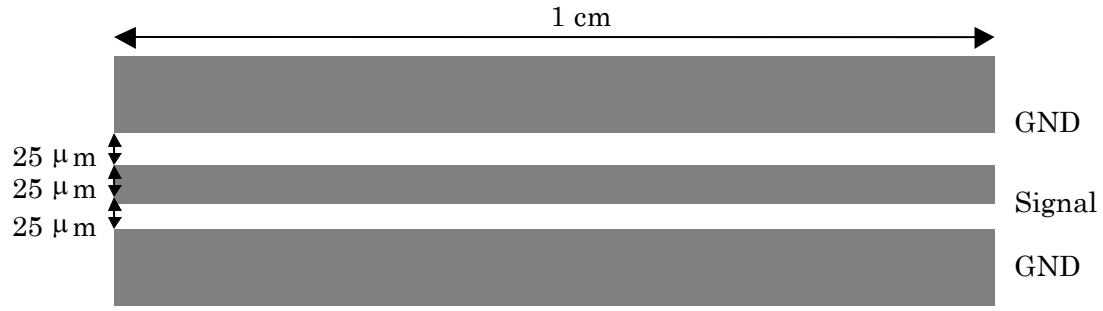


(a) Straight Type Transmission Line

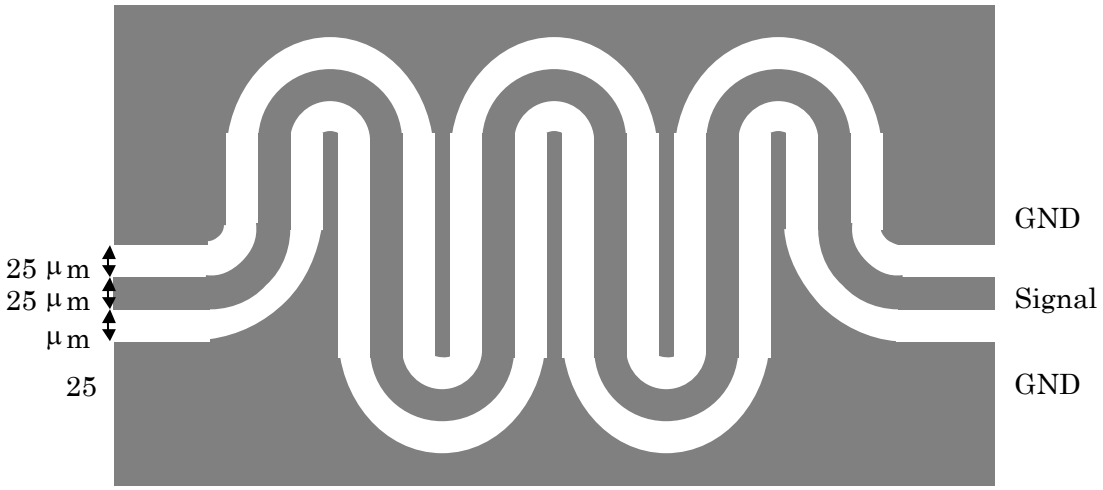


(b) Meander Type Transmission Line

Figure 3-2 (a)straight type and (b) meander type pattern were simulated by *sonnet*.

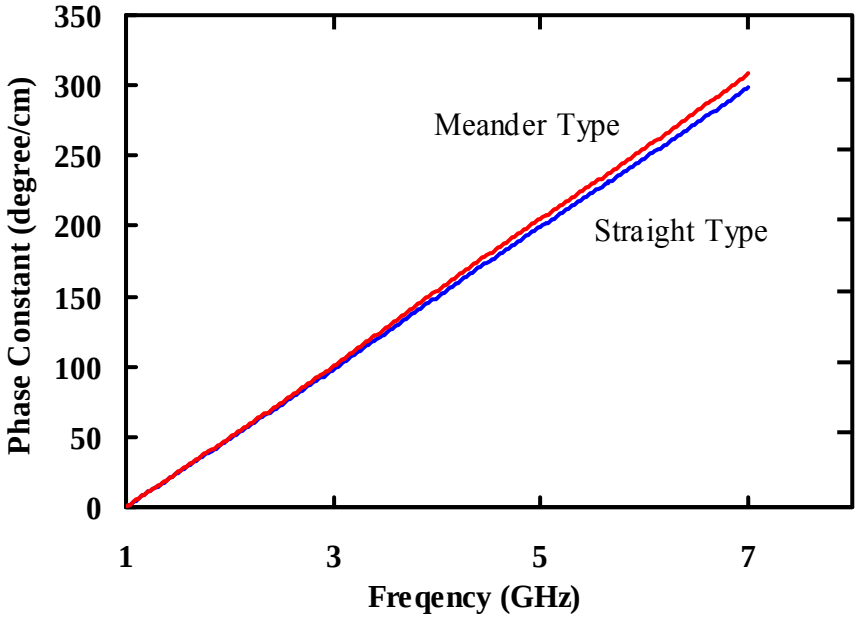


Figure 3-3 Simulated phase constant of (a) meander type and (b) straight type pattern.

Table 3-2 shows the simulation parameter to be carried out by software *sonnet* by designing waveguide shape in Fig. 3-2. Figure 3-3 shows that the straight line and meander line has similar characteristics, thus meander line can be used to save the device space. Figure 3-4 shows the SEM photo of the fabricated waveguide and the figure 3-5 shows the schematics of the coplanar waveguide.

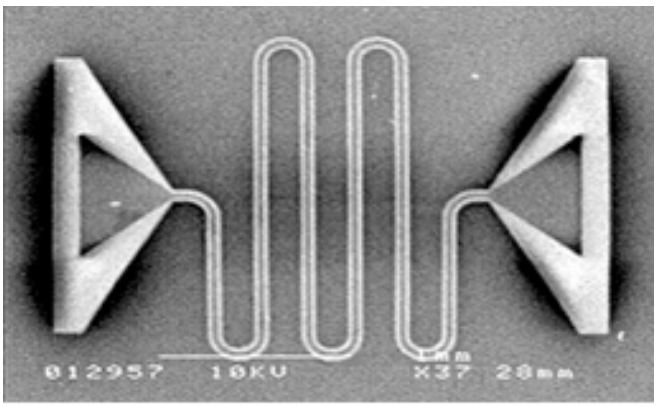


Figure 3-4 SEM image of phase shifter on BST.

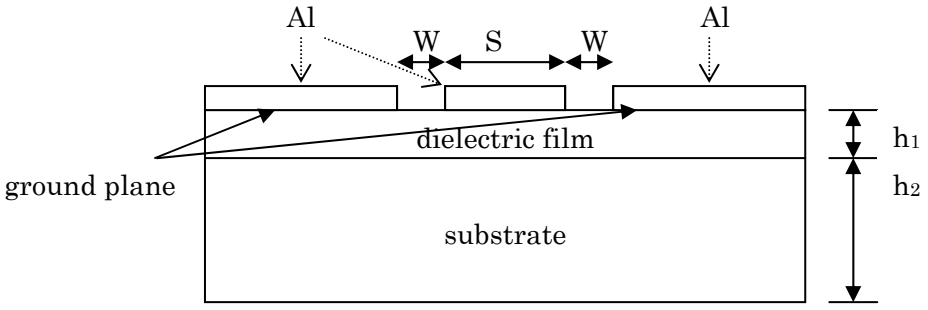


Figure 3-5 coplanar waveguide structure

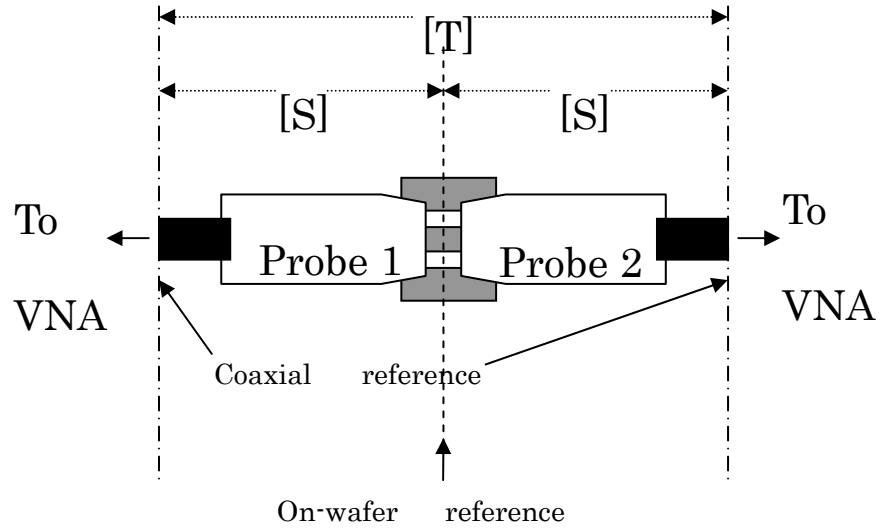


Figure 3-6 Schematic diagram for the “Thru" connection.

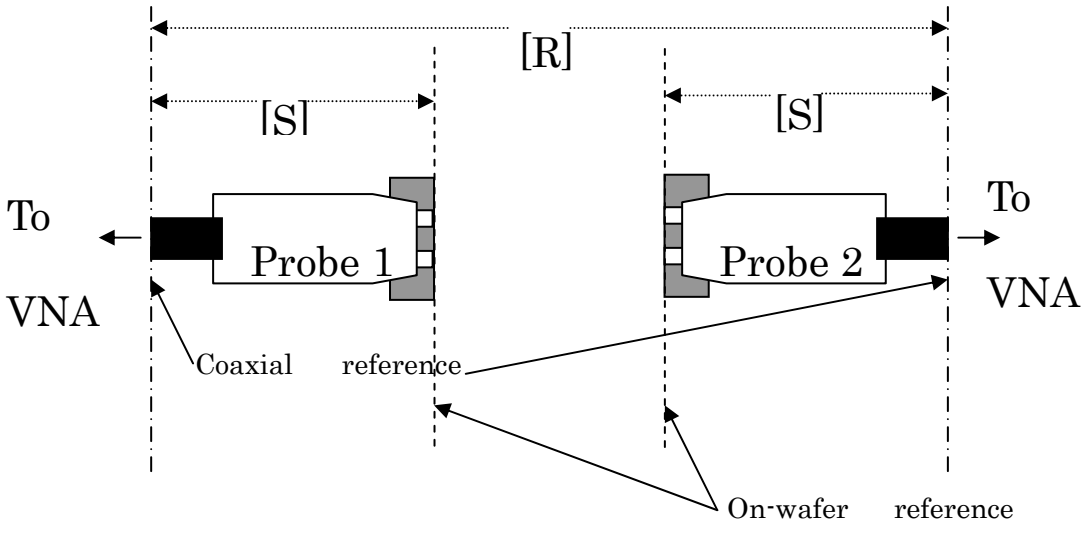


Figure 3-7 Schematic diagram for the “Reflect” connection.

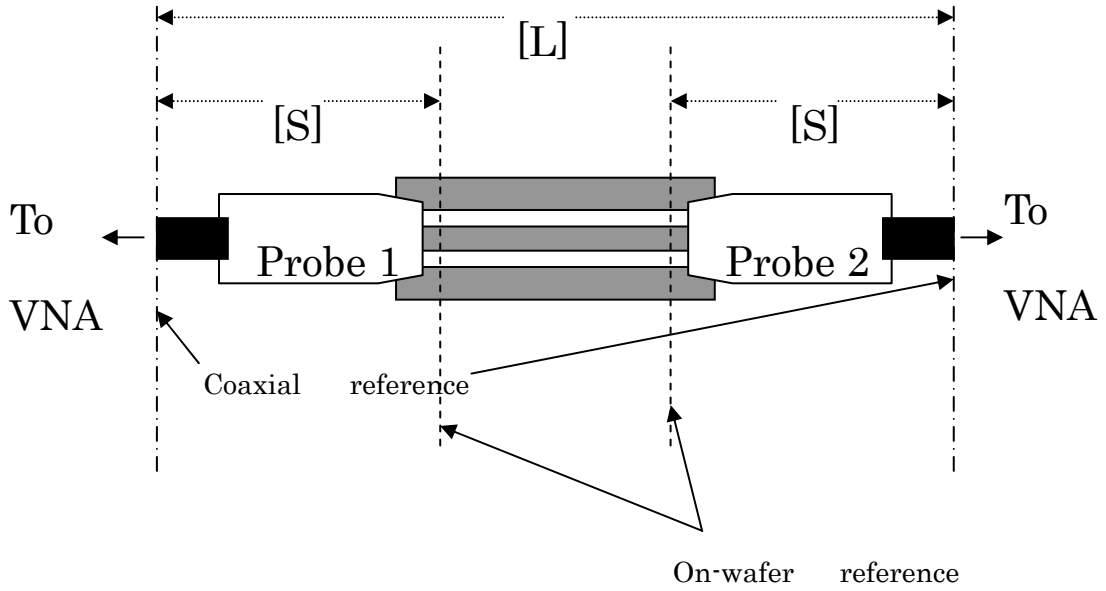


Figure 3-8 Schematic diagram for the "Line" connection.

In Figs. 3-6 to 3-8, suppose that matrix [S] is an error matrix (S-parameter matrix) that contains errors. [T], [R], [L] are Thru, Reflect, Line`s S-parameter matrix, respectively. First, calibrate the SMA connectors at "coaxial reference plane" by committing the "full-2 ports" calibration using calibration kit (agilent 85033D 3mm). Thus, we can neglect our measurement error due to SMA cables that connect our probes to a network analyzer. To move the reference plane from "coaxial reference plane" to "on-wafer reference plane", we utilize the on-wafer TRL calibration. Let Γl be an unknown reflection coefficient, we have;

$$T_{11} = S_{11} + \frac{S_{22}S_{12}^2}{1 - S_{22}^2} \tag{3-10}$$

$$T_{12} = \frac{S_{12}^2}{1 - S_{22}^2} \tag{3-11}$$

$$R_{11} = S_{11} + \frac{S_{12}^2 \Gamma l}{1 - S_{22} \Gamma l} \tag{3-12}$$

$$R_{12} = R_{21} = 0 \tag{3-13}$$

$$L_{11} = S_{11} + \frac{S_{22} S_{12}^2 e^{-2\gamma l}}{1 - S_{22}^2 e^{-2\gamma l}} \tag{3-14}$$

$$L_{12} = \frac{S_{12}^2 e^{-2\gamma l}}{1 - S_{22}^2 e^{-2\gamma l}} \tag{3-15}$$

where,

$T_{11}$: $S_{11}$ of the Thru pattern

$T_{12}$: $S_{12}$ of the Thru pattern

$R_{11}$: $S_{11}$ of the Reflect pattern

$R_{12}$: $S_{12}$ of the Reflect pattern

$L_{11}$: $S_{11}$ of the Line pattern

$L_{12}$: $S_{12}$ of the Line pattern

Now we can use equations from (3.10) to (3.15) to calculate $S_{11}$, $S_{22}$, $S_{12}$, $\Gamma l$, $e^{-\gamma l}$. It is important to notice that equation (3.14) and (3.15) will be the same to (3.10) and (3.11) if $e^{-2\gamma l} \equiv e^{-2\alpha l} e^{-2\beta l} = 1$, i.e. $l = \frac{n\lambda}{2}$ (n=1,2,3,…) for media with no loss(α=0). In practical, phase range from 20°to 160°is believed to be valid in our calculation. Below is a simulation of line length for phase 90 °at 3 GHz.

The result for positive traveling wave` propagation factor $e^{-\gamma l}$ is;

$$e^{-\gamma l} = \frac{L_{12}^2 + T_{12}^2 - (T_{11} - L_{11})^2 \pm \sqrt{\left[L_{12}^2 + T_{12}^2 - (T_{11} - L_{11})^2\right]^2 - 4L_{12}^2 T_{12}^2}}{2L_{12}T_{12}} \tag{3-16}$$

where $\gamma$ is the propagation constant.

The choice of sign in equation (3.16) is determined by the requirement that the real and imaginary parts of γ be positive. We will suppose that $S_{12}=S_{21}$ and $S_{11}=S_{22}$ for our convenience in calculation. The supposition is theoretically true because our pattern is symmetric. Then we know an attenuation constant α and a propagation constant β ;

$$e^{-\gamma l} = e^{-\alpha l} e^{-j\beta l} \tag{3-17}$$

The exponential damping factor $\alpha_d = e^{-\alpha l}$ [dB/cm]. Then;

$$\alpha_d = -\frac{S_{21}(dB)}{L(cm)} \tag{3-18}$$

$$\beta = -\frac{\Delta\phi s_{21}(rad)}{L(cm)} \tag{3-19}$$

Knowing $\alpha$ and $\beta$, the calibration is completed, and the dielectric constant and loss can be calculated.

A damping factor $\alpha_d$, and a propagation constant βcan be expressed refering to equation (3.18), (3.19). For a coplanar waveguide (CPW) phase shifter, the phase shift of transmission coefficient $S_{21}$ , $\Delta\phi_{S21}$ , is given by ;

$$\Delta\phi_{S21} = -\frac{\sqrt{\varepsilon_{eff}} \cdot f \cdot 2\pi L}{c} \tag{3-20}$$

where f is the frequency , L is the line length of the transmission line. From the slope of

$\Delta\phi_{S21}$ versus frequency f, we calculate the effective dielectric permittivity $\varepsilon_{eff}$. Using equation (3.1) ~ (3.9), we can find the BST layer`s dielectric constant.

Knowing$\varepsilon_{eff}$ , loss of the BST thin films can be calculate using equations below;

$$\alpha_d = 0.91\sqrt{\varepsilon_{eff}}\, f(GHz)\tan\delta_{eff} \quad [dB/cm] \tag{3-21}$$

$$\varepsilon_{eff}\tan\delta_{eff} = q_1\varepsilon_{r1}\tan\delta_1 + q_2\varepsilon_{r2}\tan\delta_2 \tag{3-22}$$

(3-23)

$$\tan\delta_2 = \frac{\varepsilon_{eff}\tan\delta_{eff}}{q_2\varepsilon_{r2}} \tag{3-24}$$

$\varepsilon_{r1}$ is a dielectric constant of the sapphire substrate, $\varepsilon_{r2}$ is a dielectric constant of the BST film, $\varepsilon_{re}$ is an effective dielectric constant of the BST/sapphire multilayer, tan$\sigma_2$ is the BST layer`s dielectric loss, and tan$\sigma_1$ is sapphire`s loss (<0.0001) which we can neglect.

### 3.1.2 Substrate selection for film growth

Dielectric nonlinearity in ferroelectric thin films, which is a result of applying an external electrical bias to the films, will be crucial for compact frequency-agile microwave devices [1-2]. $Ba_xSr_{1-x}TiO_3$ (BST) film exhibits high permittivity, considerable loss tangents and high nonlinearity, and therefore is considered as a promising material for microwave devices. In order to achieve higher nonlinearity, most efforts have focused on growing the BST films epitaxially on some single-crystal

substrates such as magnesium oxide (MgO), strontium titanate (STO) and lanthanum aluminate ($LaAlO_3$) [3]. These substrates are chosen because their lattice constants and thermal expansion coefficients are close to those of BST films. However, high costs and the deliquescence of the surfaces of these substrates are the practical problems for commercial BST microwave devices. As an alternative choice, the single-crystal sapphire substrates possess low dielectric losses and are relatively cheap.

## 3.2 Experimental

BST layer was sputtered on to substrates before patterning was done by photolithography method and wet etching. $Ba_{0.3}Sr_{0.7}TiO_3$, $Ba_{0.4}Sr_{0.6}TiO_3$ and $Ba_{0.5}Sr_{0.5}TiO_3$ films were deposited onto various substrates by RF magnetron sputtering method. The substrate temperature during sputtering was 600$^{o}$C. RF power was 100 Watt. In the sputtering chamber, Argon to oxygen gas ratio was set to 9:1, with flowing rate of 2 sccm. The sputtering pressure was set from 1 to 10 Pa. The thickness of deposited films after 1 hour was approximately 200 nm. After sputtered BST thin films on to substrates, Al was deposited as top electrode by electron evaporation method. Then the samples were spin-coated with solvent S1813(Shipley Far Eastern Co.) at 3000rpm for 30 seconds. The samples were baked at 80$^{o}$C for 30 minutes to dry up the

solvent. After that, UV light was exposed for 20 seconds through a mask alignment. Then the samples were soaked into developer MF CD-26(Shipley Far Eastern Co.) for around 5 seconds to peel off the solvent layer exposed to the UV light. The samples were wet-etched by alkali etching liquid SemikoClean(Furuuchi Co.) at 40$^{o}$C for 3 minutes. Then acetone was used to wash out all the solvent. Finally the samples were soaked into pure water and then were dried up.

The photolithography masks were prepared in a cleanroom. First, minicopy films HR2 (Fujifilm Co.), were used as camera films and the films were taken by a manual camera at various exposed light quantity by changing camera shutter speed. The films were then soaked into the film developer liquid (Copinal) for 5 minutes. The films were then soaked into the coating liquid (Fujifix) for 5 minutes to form a protecting layer and then washed by water. Then the films were miniaturized to 1/100 times in a dark room. After being exposed to light, Copinal and Fujifix were used again as a developer and coating liquid. At last, the patterned masks were washed by pure water.

The resultant stoichiometric composition of the BST films was confirmed by X-ray fluorescence spectroscopy. The crystalline structure of deposited films was confirmed by X-ray diffraction (XRD) analysis.

Microwave measurements were carried out with a network analyzer (R3767CH, Advantest) over the frequency range from 0.1 to 8 GHz. The propagation constant was calculated from *S*-parameters of the coplanar waveguide lines through the TRL calibration method. Details of the coplanar waveguide structures and the measuring method are given in [4]. The phase of a signal on the coplanar line and the loss tangent of the BST thin film were calculated from the propagation constant of the microwave signal in the waveguide.

## 3.3 Results

### 3.3.1 Comparison of the tunability of various BST film compositions ($Ba_{0.3}Sr_{0.7}TiO_3$, $Ba_{0.4}Sr_{0.6}TiO_3$ and $Ba_{0.5}Sr_{0.5}TiO_3$)

First, the BST film (thickness 200 nm) was sputtered onto R-cut sapphire (thickness 500 μm) to compare the tunability of these films at microwave frequency. Coplanar waveguide with both single line width and gap width of 26μm was fabricated. The waveguide length was 1 cm. An external DC bias of 200 V was applied across the 26 μm, resulting in phase shift of the microwave signal which was traveling through the waveguide. Because the amount of phase shift corresponds to the decrease of the

permittivity of the BST films under an external DC bias, the tunability of the films can be observed in the form of phase shift. Higher phase shift means that the film has more tunability.

Figure 3-9 shows the result of phase shift. At 8 GHz, the phase shift due to $Ba_{0.3}Sr_{0.7}TiO_3$, $Ba_{0.4}Sr_{0.6}TiO_3$ and $Ba_{0.5}Sr_{0.5}TiO_3$ films was 0.5, 1.5 and 2.5, respectively. This means that $Ba_{0.5}Sr_{0.5}TiO_3$ film has highest tunability. From this point, the $Ba_{0.5}Sr_{0.5}TiO_3$ was chosen in the following part of this dissertation. Table 3-3 shows the dielectric constants and losses of these BST films.

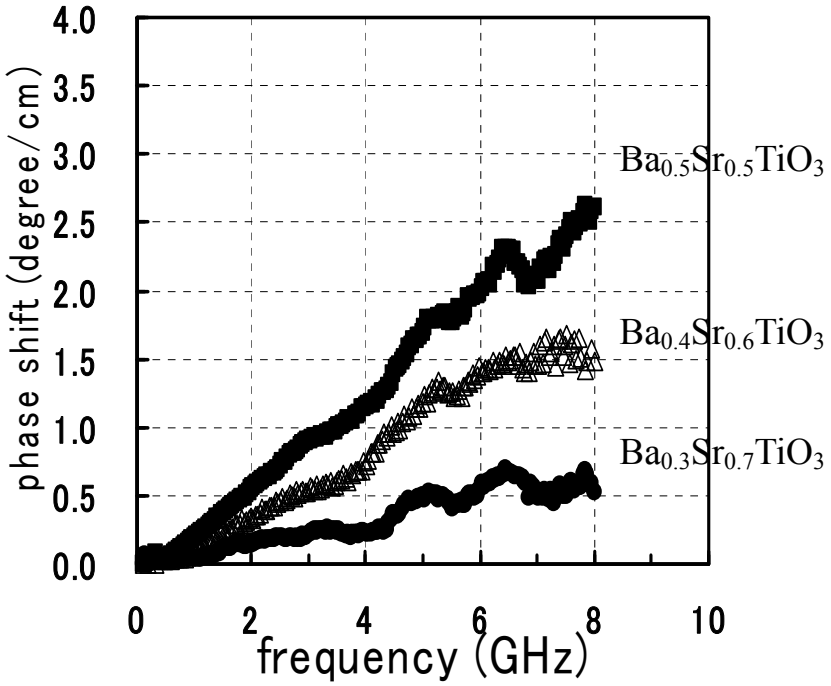


Figure 3-9 Phase shifts of various BST compositions.

Table 3-3 The electric constants and losses of the BST films

| Sample | Relative dielectric constant | | Dielectric loss | |
|---|---|---|---|---|
| | 1 MHz (BST on Platinum/silicon) | 3 GHz (BST on sapphire) | 1 MHz (BST on Platinum/silicon) | 3 GHz (BST on sapphire) |
| $Ba_{0.3}Sr_{0.7}TiO_3$ | 55 | 229 | 0.018 | 0.028 |
| $Ba_{0.4}Sr_{0.6}TiO_3$ | 121 | 354 | 0.035 | 0.026 |
| $Ba_{0.5}Sr_{0.5}TiO_3$ | 344 | 616 | 0.045 | 0.016 |

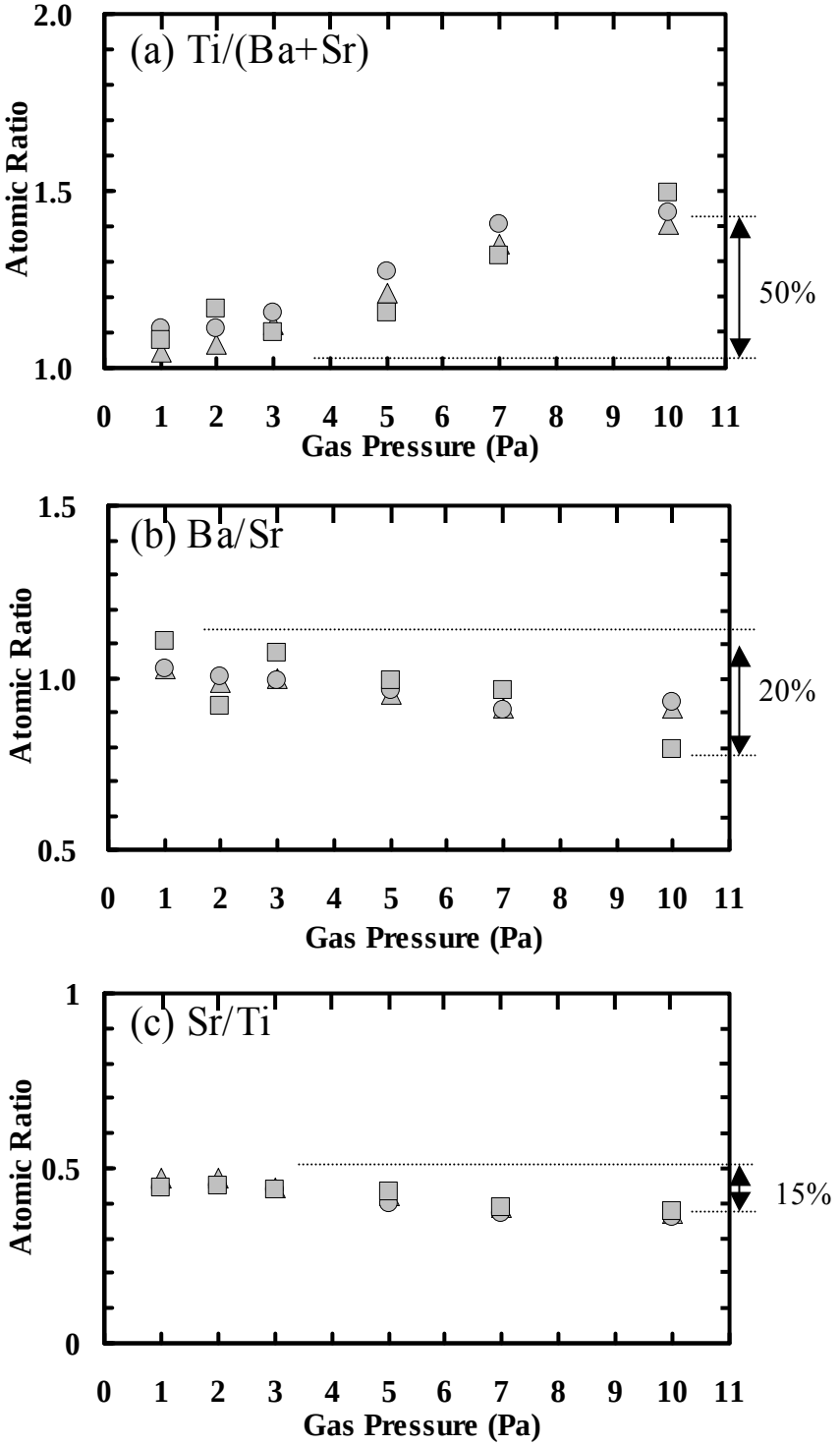


Figure 3-10 Composition of BST films deposited on various substrates.
(a) Ti/(Ba+Sr), (b) Ba/Sr and (c) Sr/Ti
□ MgO △ R-cut α-$Al_2O_3$ ○ C-cut α-$Al_2O_3$

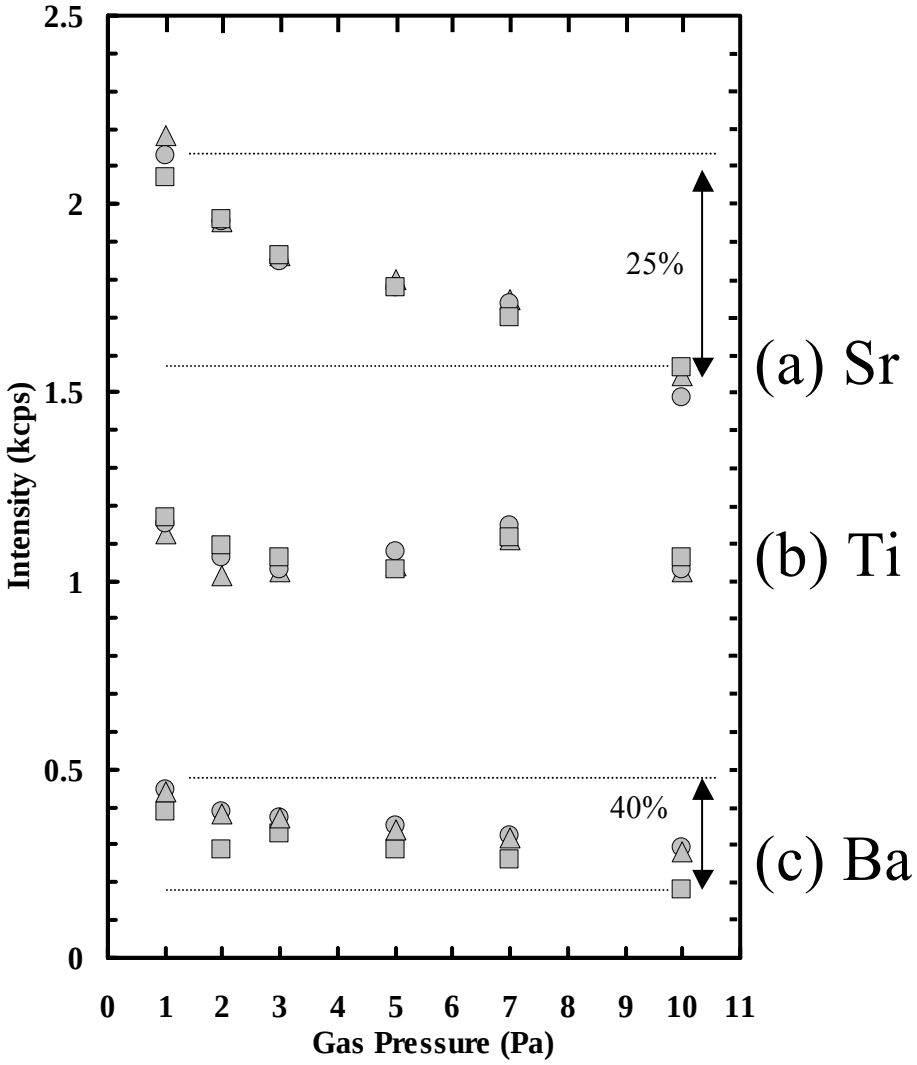


Figure 3-11 Count per second of (a)Strontium, (b) Titanium and (c) Barium on various substrates.
□ MgO △ R-cut α-$Al_2O_3$ ○ C-cut α-$Al_2O_3$

### 3.3.2 Influence of the sputtering pressure on the stoichiometry of the sputtered BST films

Figure 3-10 and 3-11 show the XRF analysis of the sputtered BST. Lower sputtering gas pressure results in BST films with composition close to the BST target. This was found to be independent on substrate type, and should be solely the results of sputtering process. At higher sputtering gas pressure, the sputtered BST film was titanium-rich, and the Ba/Sr ratio decreased. From the x-ray counts in XRF analysis, The Sr, Ba and Ti composition in the sputtered film was found to decrease by 25%, 40% and 10 %, respectively. This may be due to the argon atoms have lower energy when the plasma density increases as the sputtering gas pressure becomes higher. From this result, the sputtering gas pressure of 2 Pa is suitable for sputtering BST film with close composition to the sputtering target.

### 3.3.3 Influence of the sputtering pressure on the crystallinity of the sputtered BST films

Figure 3-12 shows the results of XRD $\theta$–$2\theta$ scans for BST deposited on MgO substrate. The XRD peak found at $42^{o}$ is the peak of the MgO(200), which is a substrate. In all

films BST(100) and BST(200) peak at 22° and 46°, respectively, are found. The count of x-ray was highest when the sputtering gas pressure was 2 Pa, implying good crystallinity. Rocking-curve scans were recorded to determine whether the films were fully coherent. Figure 3-13 shows the Full Width Half Maximum (FWHM) of the rocking curve measurement. The FWHM is below 1° in films that were sputtered at gas pressure below 7 Pa, while it goes beyond 1.5° at gas pressure of 10 Pa.

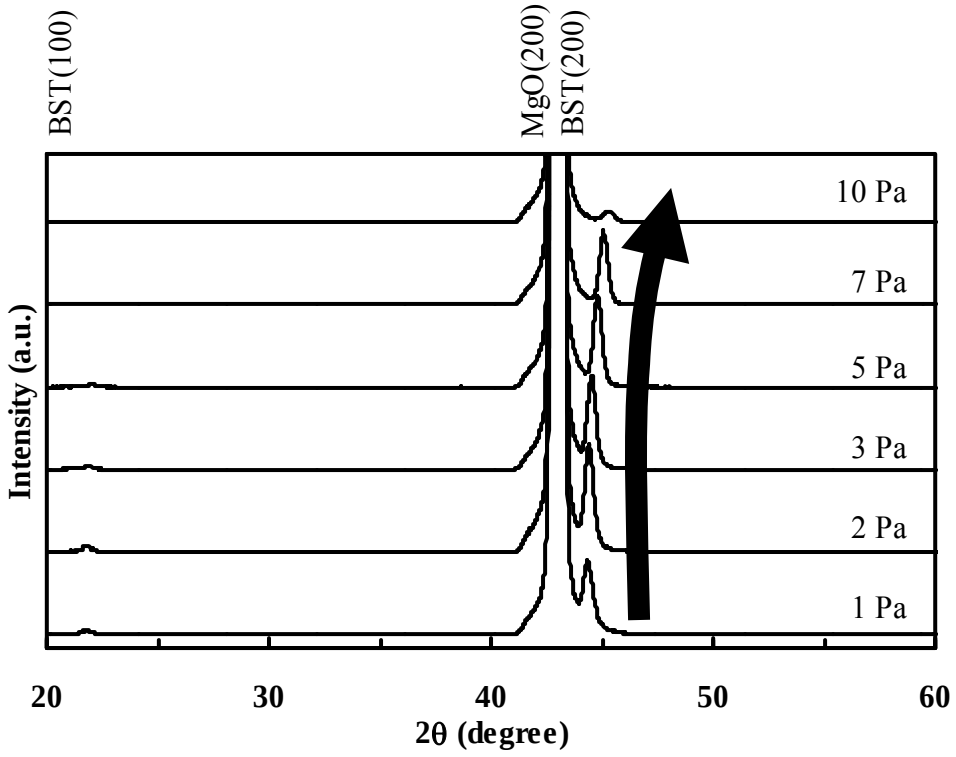


Figure 3-12 θ-2θ measurements of the BST films deposited on MgO substrate at various gas pressures.

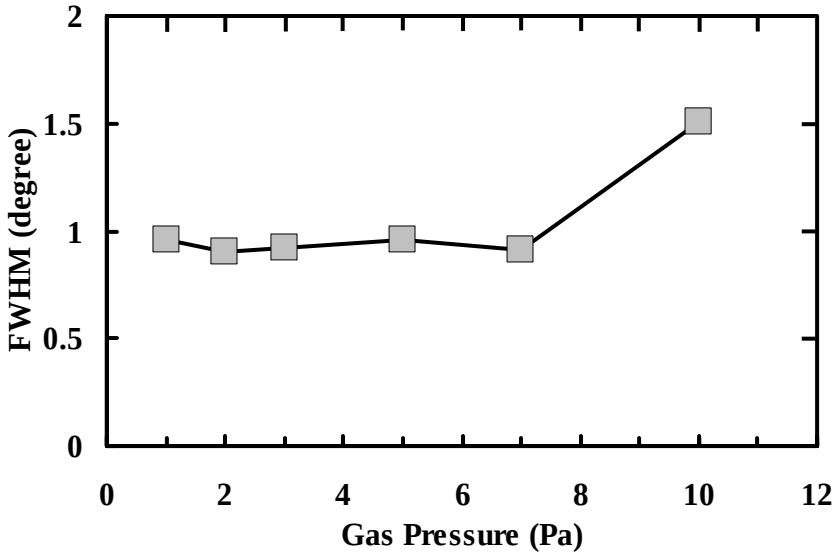


Figure 3-13 FWHM of BST 100 on MgO substrate by rocking curve.

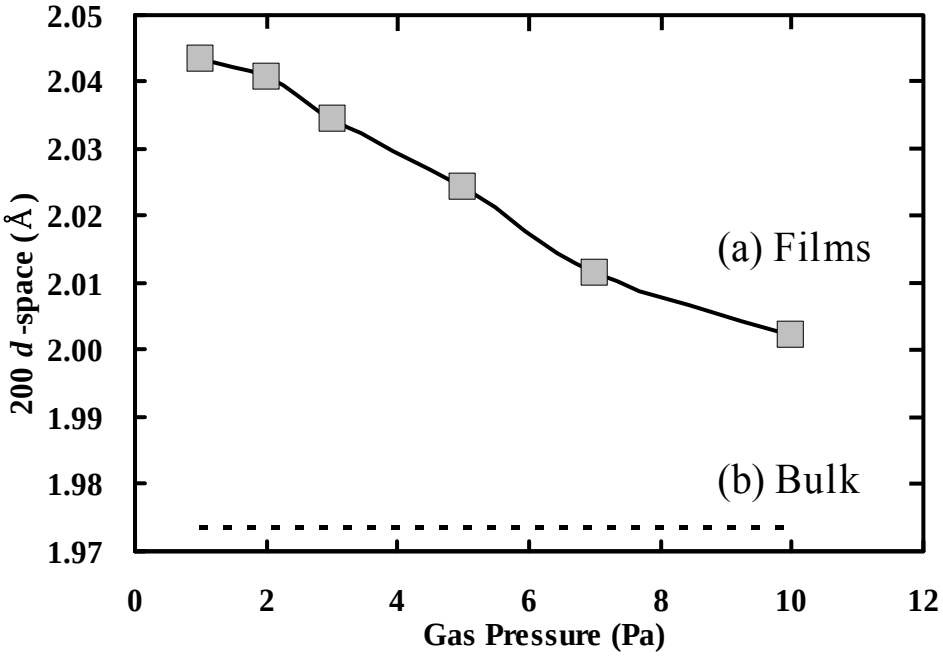


Figure 3-14 BST(200) *d*-space of (a) films on MgO and (b) bulk BST (ICDD:39-1395).

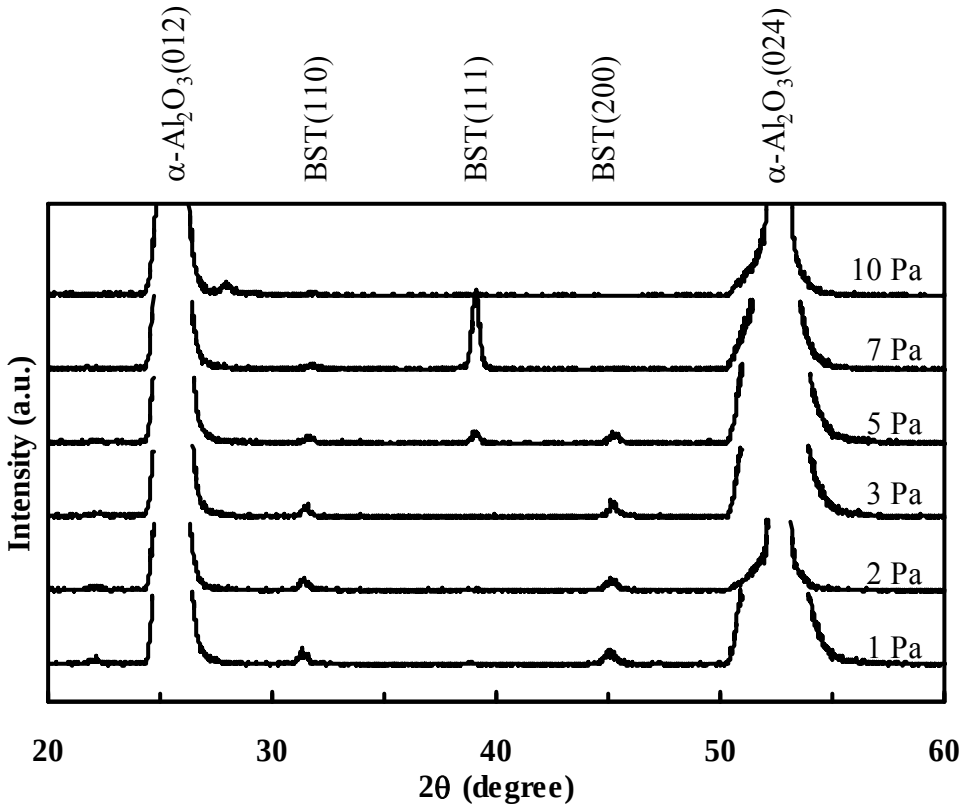


Figure 3-15 θ-2θ measurements of the BST films on R-cut $\alpha$-$Al_2O_3$ substrate at various gas pressures.

In the case of R-cut sapphire substrate (Fig. 3-15), $\alpha$-$Al_2O_3$(012), $\alpha$-$Al_2O_3$(024) substrate peak are found at $26^o$ and $53^o$, respectively. At sputtering gas pressure of 1-3 Pa, BST(110) and BST(200) peak were found at $32^o$ and $46^o$, respectively. At 5 Pa, in addition to BST(110) and BST(200) peak, there is a BST(111) peak at $39^o$. At 7 Pa, BST(200) peak disappears while BST(110) peak becomes weaker and BST(111) peak becomes stronger. At 10 Pa, there are no peaks of BST, meaning that the film was not crystallized. All results in the case of R-cut sapphire show low counts of x-ray, implying poor crystallinity of the deposited films.

In the case of C-cut sapphire substrate (Fig. 3-16), $\alpha$-$Al_2O_3$(006) substrate peak is found at $42^o$. All samples have BST(111) peak at $39^o$. This peak becomes strongest at 7 Pa, and weakest at 10 Pa. At the sputtering gas pressure of 1-3 Pa, weak BST(110) and BST(200) peak were observed, but these peaks disappear when the gas pressure is more than 5 Pa. At the sputtering gas pressure more than 5 Pa, all films are found to be single-oriented.

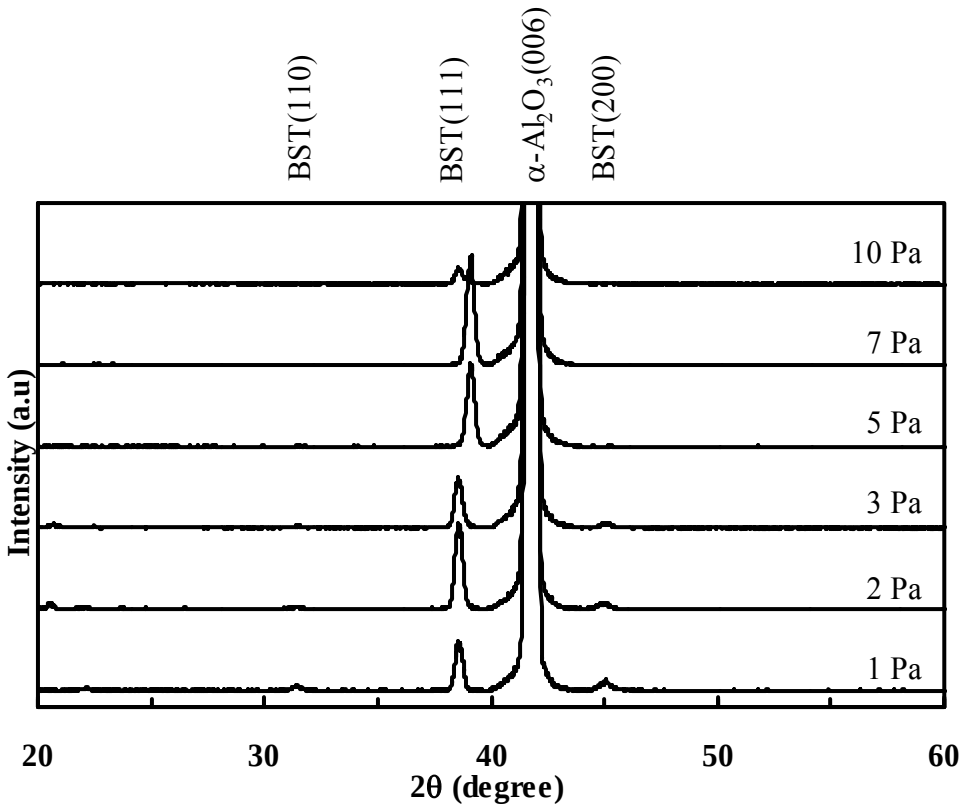


Figure 3-16 θ-2θ measurements of the BST films deposited on C-cut $\alpha$-$Al_2O_3$ substrate at various gas pressures.

### 3.3.4 Epitaxial growth of the BST films

From the previous section, there is a possibility for epitaxial growth of BST films on MgO and C-cut sapphire. To determine whether the films were epitaxially grown, $\phi$-scans were recorded. Figures 3-18 show the results of $\phi$-scans of the c-cut substrate and the BST films sputtered under the gas pressure of 7 Pa and 2 Pa, respectively. From this, we observe good BST [011] || c-cut sapphire [012] epitaxy. It was concluded that the film deposited on the c-cut substrate was epitaxially grown.

### 3.3.5 Phase shift and loss tangent in coplanar line structure

BST film (thickness 1 μm) was deposited onto various substrates. Then the coplanar waveguide was built directly onto the BST layer. The aluminum was deposited on top as an electrode. The microwave signal was fed through the waveguide and the phase of this signal was observed through the network analyzer. After a DC bias of 200 V was applied across the gap of the waveguide, the phase of the microwave signal shifted corresponding to the decrease of the permittivity of the BST film. Because the permittivity of the substrate under an applied bias is very small in comparison to that of the BST film, the phase shift under the influence of the DC bias occurs because of the film. The phase shift per unit line length is defined as the difference between the signal phase at zero bias and that under a DC bias across a slot of 25 $\mu$m. The results of the

phase shift at 3 GHz and a bias of 200 V are shown for comparison (Table 3-4).

## 3.4 Discussion

### 3.4.1 Influence of the sputtering pressure on the stoichiometry of the sputtered BST films

From the x-ray counts in XRF analysis, The Sr, Ba and Ti composition in the sputtered film was found to decrease by 25%, 40% and 10 %, respectively. From this result, the sputtering gas pressure of 2 Pa is suitable for sputtering BST film with close composition to the sputtering target.

### 3.4.2 Influence of the sputtering pressure on the crystallinity of the sputtered BST films

In the case of MgO substrate, from Fig. 3-2, in-plane crystallinity coherence was found to be dependent on the sputtering gas pressure. This result corresponds to the XRF analysis that lower sputtering gas pressure results in stoichiometric film. Moreover, at higher sputtering gas pressure, BST(200) peak shifts to higher $2\theta$ value, implying that the lattice constant of the BST film becomes lower. Figure 3-14 shows the lattice constant of the sputtered BST film, with comparison to that of a BST bulk. At higher

sputtering gas pressure, the lattice constant of the film becomes closer to that of the bulk, implying the possibility of epitaxial film growth. This result combining with the result in Fig. 3.2 may also imply the possibility that as the sputtering gas pressure becomes higher, out-of-plane lattice constant becomes lower and, at the same time, the in-plane lattice constant becomes higher.

### 3.4.3 Epitaxial growth of the BST films

The crystal structure of both MgO and BST are cubic. The lattice mismatch between the MgO and BST is 6.3%. As shown in Fig. 3-17, the result of $\phi$-scans show that the position of MgO(022) and BST(011) peaks are at the same position, with interval of $90^o$ between each peak. The angle between the plane of MgO(001) and MgO(011) is $45^o$. The angle between the plane of BST(001) and BST(011) is also $45^o$. Pole figure of the MgO and BST was shown in Fig. 3-19. This implies that both MgO and the deposited BST have the same crystal orientation. Thus, the unit cell of in plane of BST(100) was epitaxially grown on the unit cell of plane MgO(100).

On the other hand, the crystal structure of the C-cut sapphire is hexagonal. From Fig. 3-18, $\alpha$-$Al_2O_3$(012) has three peaks and the interval between each $\alpha$-$Al_2O_3$(012) peak

was 120$^{o}$, while there are six BST(011) peaks and the position of the BST(011) peaks shift 30$^{o}$ from the α-$Al_2O_3$(012) peaks. The angle between the plane of α-$Al_2O_3$(001) and α-$Al_2O_3$(012) is 57.6$^{o}$. The angle between the plane of BST(111) and BST(011) is 35.26$^{o}$. Pole figure of the MgO and BST was shown in Fig. 3-19. In this way, three unit cells of BST(111) were positioned on two unit cells α-$Al_2O_3$(001) in periodic order. The lattice mismatch is 1.6% in this case, which is lower than that of mismatch of 6.3% between BST(100) and MgO(100). This may be the reason why there are shifts of BST peaks in $\theta$–$2\theta$ scans for BST deposited on MgO substrate, but not for BST deposited on C-cut substrates.

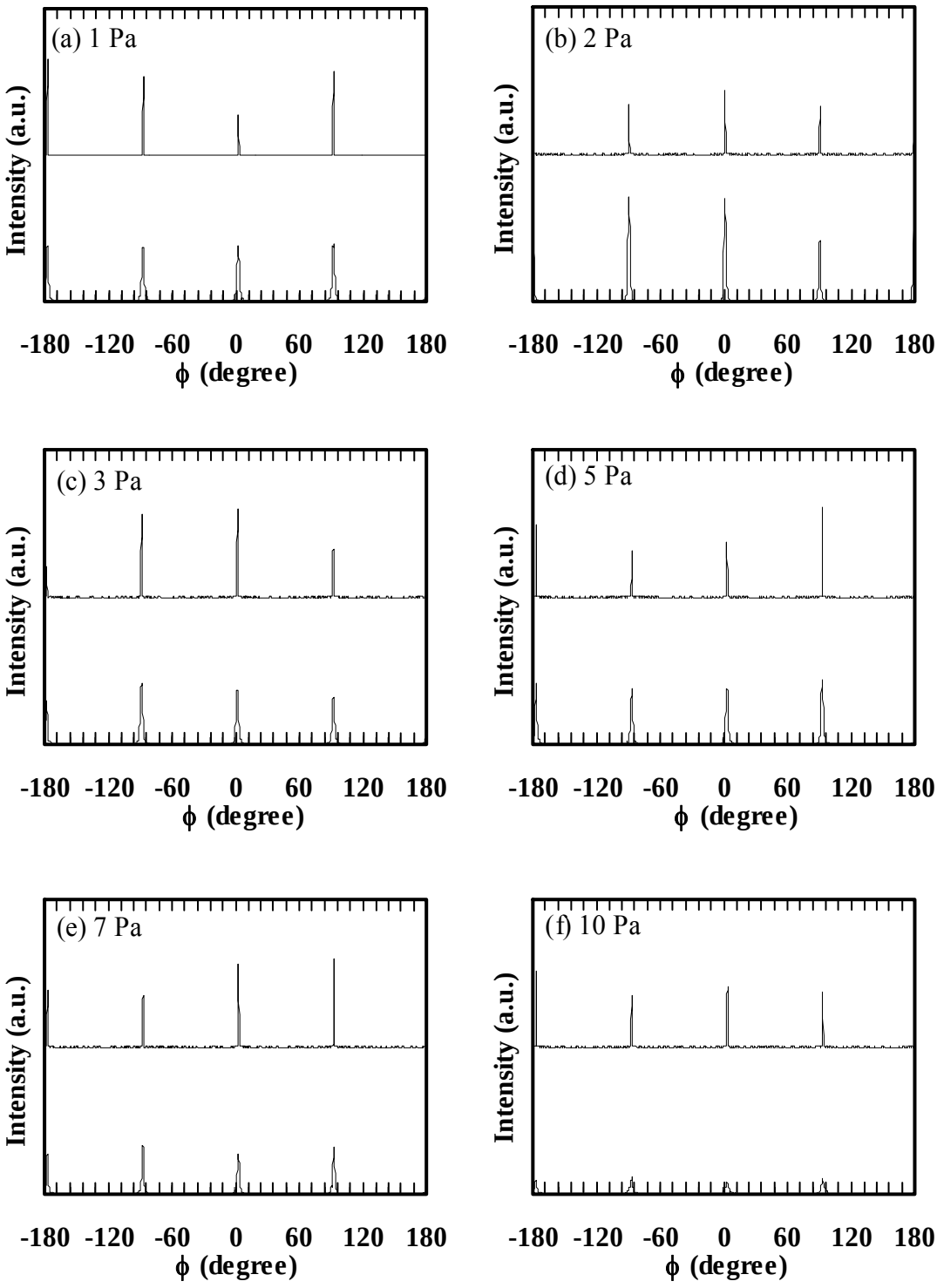


Figure 3-17 ϕ-scan of the BST films on MgO.

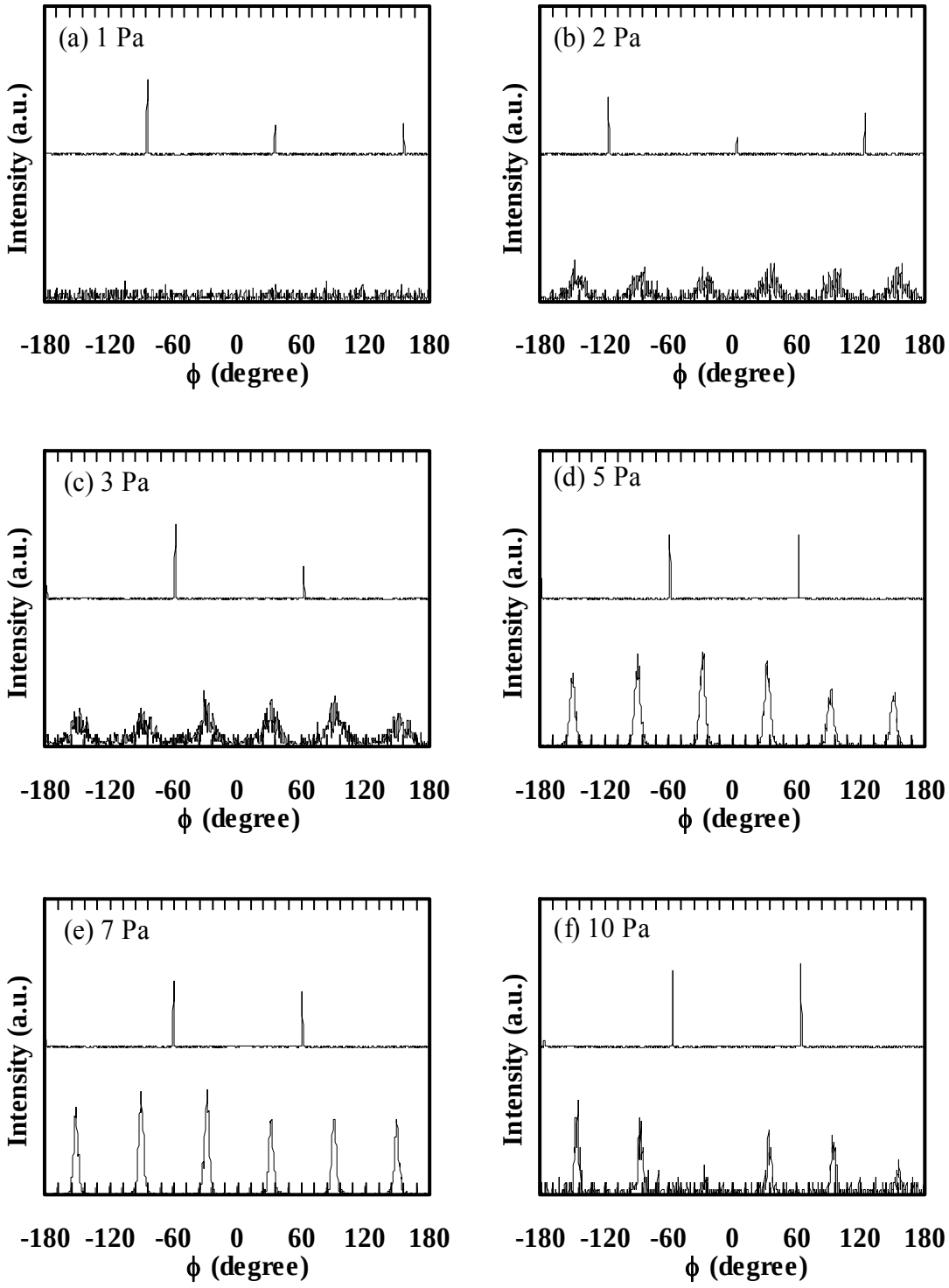


Figure 3-18 ϕ-scan of the BST films on C-cut $\alpha$-$Al_2O_3$.

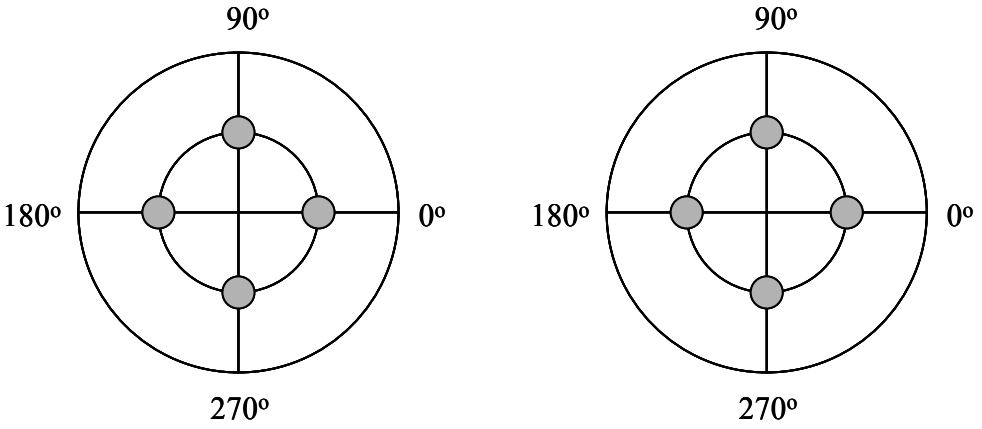


Pole figure of MgO　　Pole figure of BST

(a) Pole figure of (a) MgO100 and (b) BST100

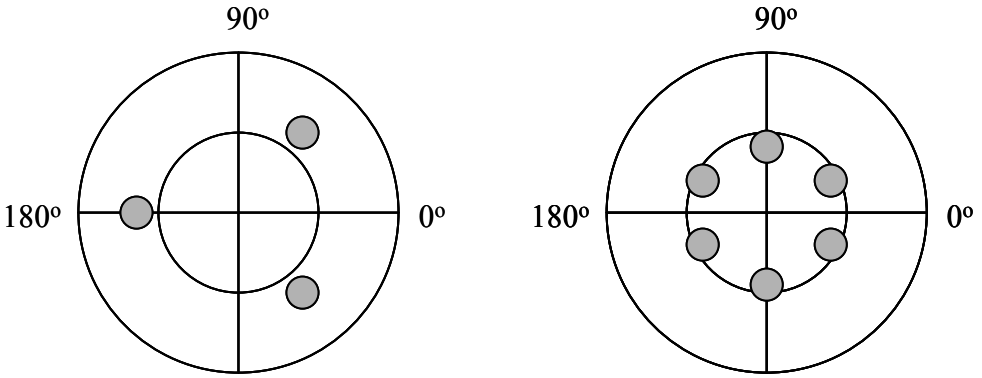


Pole figure of $\alpha$-$Al_2O_3$　　Pole figure of BST

(b) Pole figure of $\alpha$-$Al_2O_3$001 and BST111

Figure 3-19 Pole figure of BST epitaxial films on MgO and $\alpha$-$Al_2O_3$ substrates.

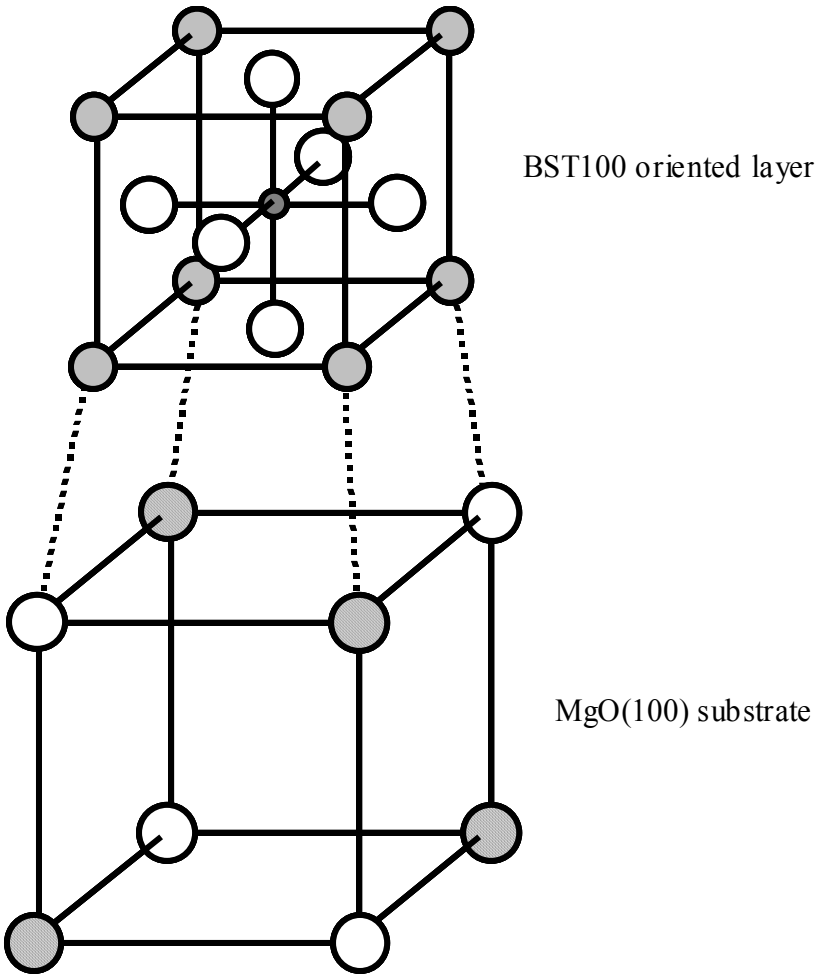


Figure 3-20　BST100 oriented thin films epitaxial growth on MgO(100)

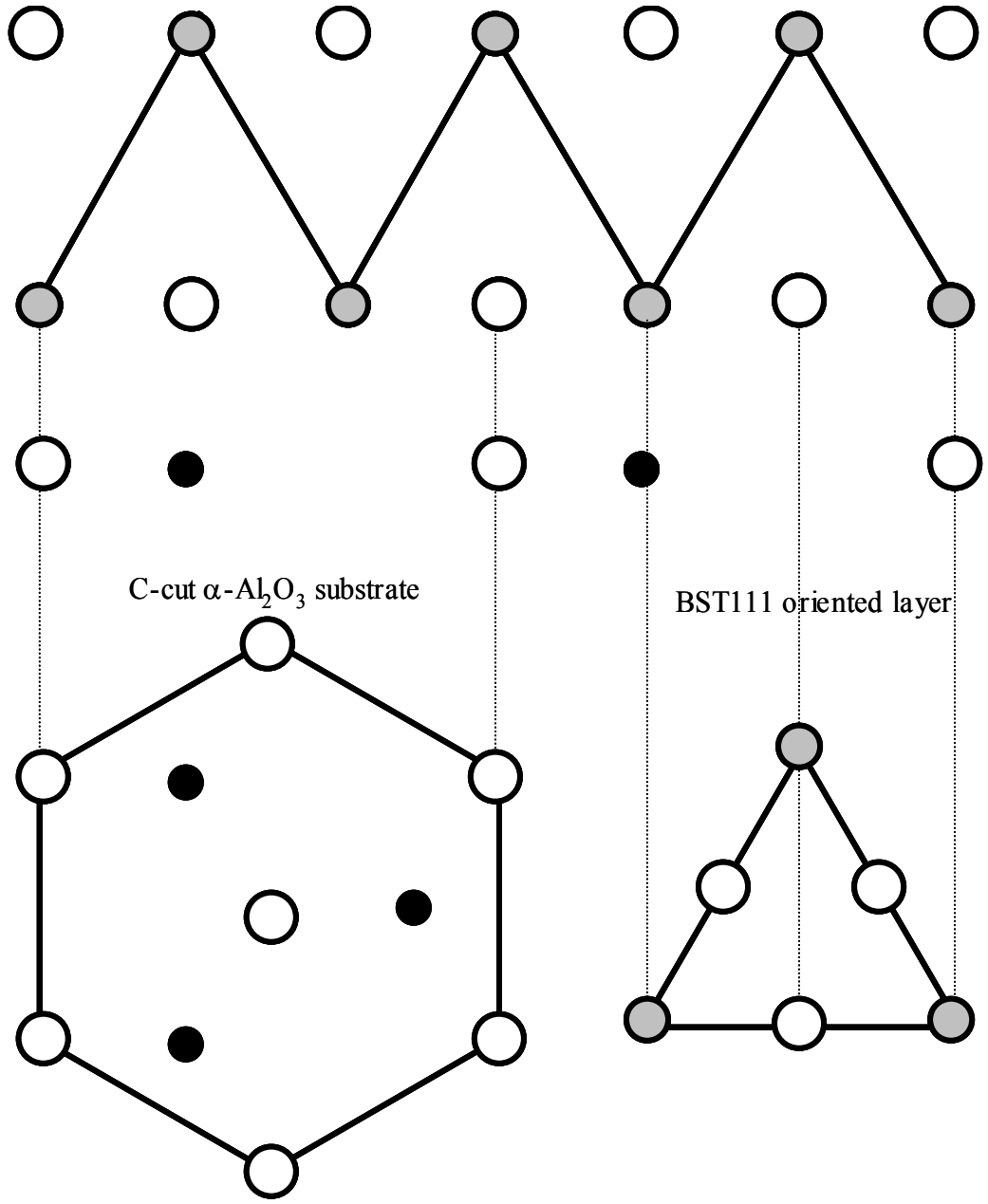


Figure 3-21 BST111 oriented thin films epitaxial growth on C-cut $\alpha$-$Al_2O_3$.

Table 3-6 summarize all results shown above. Figures 3-20 and 3-21 show how the BST unit cell epitaxially growed on the substrates.

### 3.4.4 Phase shift and loss tangent in coplanar line structure

From Tables 3-4 and 3-5, comparing with the resultant phase shifts, the BST grown on c-cut sapphire showed the largest phase shift in the coplanar waveguide lines, followed by the MgO and r-cut sapphire substrates. From this result, the high crystalline quality in BST film was observed to strongly influence the phase shift, which is highly correlated with the tunability (i.e., the dependence of permittivity on DC bias) of the deposited film. Others have investigated similar microwave properties of thin [6] and thick [7] BST films (Table 3-4). Note that phase shift increases almost linearly with increasing frequency and nonlinearly with the applied bias, and the larger slot (25 $\mu$m) in our experiment should, in comparison, result in a smaller phase shift. The highest loss tangent was found in the BST films deposited on the r-cut sapphire, followed by those deposited on the c-cut sapphire, and MgO substrate. Accordingly, the loss of BST on MgO and c-cut sapphire are low because the films deposited were epitaxially grown. Less-oriented films have a different stoichiometry at different regions and especially at

grain boundaries; this is considered as the primary cause of the high loss in a less-oriented film. Thus, the loss is low when the BST film is highly oriented.

Data of the phase shift is shown in Fig. 3-22. For silicon, loss is too high and the silicon acts as conductive layer so that the phase shift is higher. But such structure is different from other samples and cannot be compared with. It was concluded that BST grown directly on silicon is not suitable for microwave application because of its high loss.

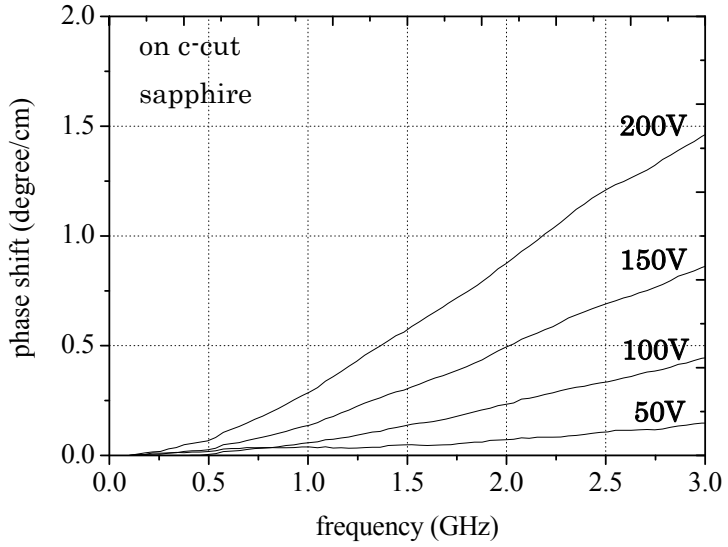
on c-cut
sapphire
200V
150V
100V
50V
phase shift (degree/cm)
frequency (GHz)
0.0
0.5
1.0
1.5
2.0
2.5
3.0

(a)

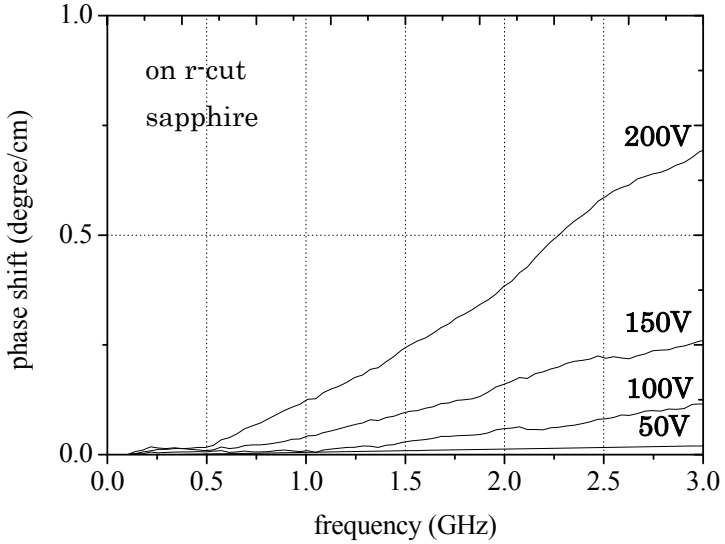
on r-cut
sapphire
200V
150V
100V
50V
phase shift (degree/cm)
frequency (GHz)
0.0
0.5
1.0
1.5
2.0
2.5
3.0

(b)

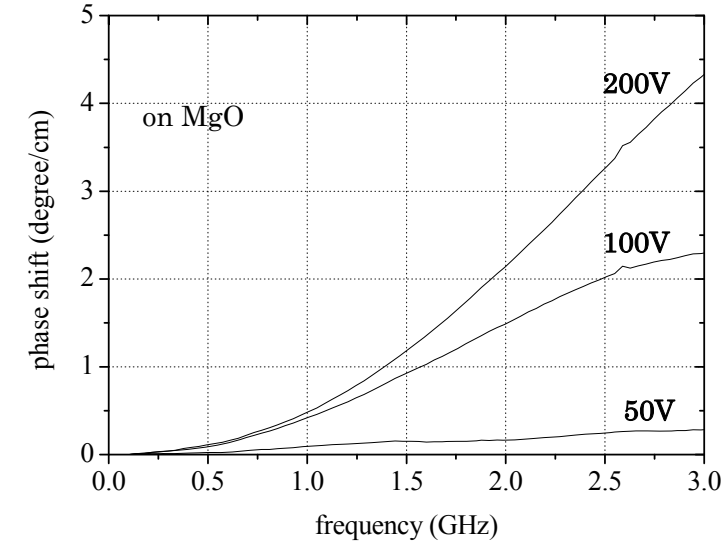


(c)

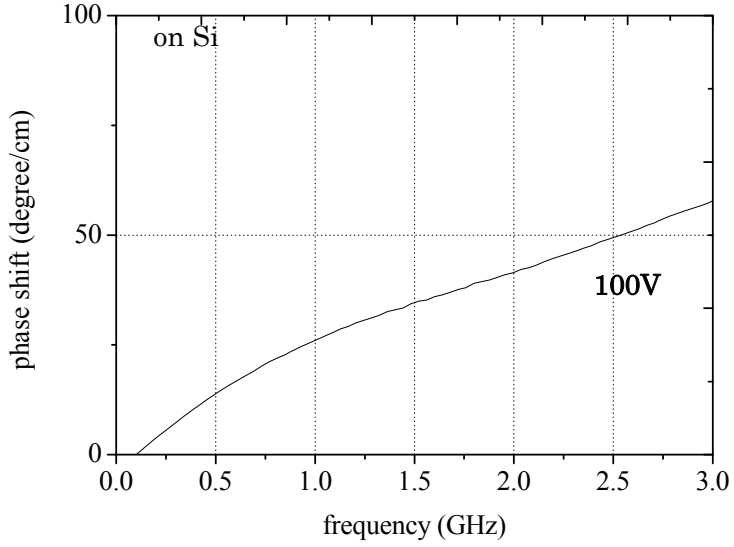


(d)

Figure 3-22 Phase shifts in a coplanar waveguide, after applied an external dc bias to the BST films deposited on: a) c-cut sapphire, b) r-cut sapphire, c) MgO, d) silicon.

Table 3-4 Summaries of the dielectric properties measured by coplanar waveguide method [5, 10].

| case | Substrate | Ba ratio in BST ($x$) | Film thickness | Applied bias: slot width | Phase shift | Loss tangent |
|---|---|---|---|---|---|---|
| 1 (7 Pa) | c-cut sapphire | 0.5 | 1 $\mu$m | 80 kV/cm: 25 $\mu$m | 6.3°/cm @3 GHz | 0.009 @7 GHz |
| 2 (2 Pa) | c-cut sapphire | 0.5 | 1 $\mu$m | 80 kV/cm: 25 $\mu$m | 1.5°/cm @3 GHz | 0.026 @7 GHz |
| 3 (2 Pa) | MgO | 0.5 | 1 $\mu$m | 80 kV/cm: 25 $\mu$m | 4.4°/cm @3 GHz | 0.008 @7 GHz |
| 4 | r-cut sapphire | 0.5 | 1 $\mu$m | 80 kV/cm: 25 $\mu$m | 0.7°/cm @3 GHz | 0.016 @7 GHz |
| *(ref.* [5]) | r-cut sapphire | 0.5 | 0.2 $\mu$m | 20 kV/cm: 20 $\mu$m | 11.6°/cm @20 GHz | 0.05~0.07 @7-20 GHz |
| *(ref.* [10]) | alumina | 0.6 | 5 $\mu$m | 25 kV/cm: 16 $\mu$m | 1.26°/cm @24 GHz | 0.09 @24 GHz |

Table 3-5 Summary of the effective dielectric constants and dielectric losses of the BST films measured by coplanar waveguide method.

| BST on substrate | DC bias (V) | Dielectric constant (effective) | Loss tangent (7GHz) |
|---|---|---|---|
| MgO | 0 | 7.568632 | 0.007 |
| | 50 | 7.54237 | 0.008 |
| | 150 | 7.566004 | 0.016 |
| | 200 | 7.537123 | 0.027 |
| c-cut sapphire | 0 | 10.59254 | 0.025 |
| | 50 | 10.5801 | 0.025 |
| | 100 | 10.54595 | 0.026 |
| | 150 | 10.50255 | 0.026 |
| | 200 | 10.44072 | 0.025 |
| r-cut sapphire | 0 | 9.353724 | 0.020 |
| | 50 | 9.350156 | 0.014 |
| | 100 | 9.341394 | 0.014 |
| | 150 | 9.280173 | 0.014 |
| | 200 | 9.280173 | 0.014 |

**References**

1) F. A. Miranda, G. Subramanyam, F. W. Van Keuls, R. R. Romanofsky, J. D. Warner and C. H. Mueller, "Design and development of ferroelectric tunable microwavecomponents for Ku and K-band satellite communication systems", IEEE Transaction of Microwave Theory and Techniques, **48** (2000) 1181

2) O. Auciello, S. Saha, D. Y. Kaufman, S. K. Streiffer, W. Fan, B. Kabius, J. Im and P. Bauman, "Science and Technology of High Dielectric Constant Thin Films and Materials Integration for Application to High Frequency Devices", Journal of Electroceramics **12** (2004) 119

3) M. F. Iskander, Z. Zhang, Z. Yun, R. S. Isom, M. G. Hawkins, R. Emrick, B. Bosco, J. Synowczynski and B. Gersten, "New phase shifters and phased antenna array designs based onferroelectric materials and CTS technologies", IEEE Transaction of Microwave Theory and Techniques, **49** (2001) 2547

4) S. Hyun, J. H. Lee, S. S. Kim, K. Char, S. J. Park, J. Sok and H. E. Lee, "Anisotropic tuning behavior in epitaxial $Ba_{0.5}Sr_{0.5}TiO_3$ thin films" Applied Physics Letters, **77** (2000) 3084

5) H. Lue and T. Tseng, "Application of on-wafer TRL calibration on the measurement ofmicrowave properties of $Ba_{0.5}Sr_{0.5}TiO_3$ films" IEEE Transaction of Ultrasonics,

Feeroelectrics and Frequency Control, **48** (2001) 1640

6) M. D. Janezic and J. A. Jargon, "Complex permittivity determination from propagation constant measurements" IEEE Microwave & Guided Wave Letters, **9** (1999) 76

7) G. Bhakdisongkhram, Y. Yamashita, T. Nishida and T. Shiosaki, " Dependence of Microwave Properties of $Ba_xSr_{1-x}TiO3$ Thin Films on Substrate", Japanese Journal of Applied Physics, **44** (2005) 7098

8) D. M. Pozar, "Microwave Engineering", John Wiley and Sons, New York, (1998), 2nd ed., 217

9) K. C. Gupta, R. Garg, I. Bahl and P. Bhartia, "Microstrip Lines and Slotlines" Artech House, London (1996), 2nd ed., 83 and 379.

10) F. Zimmermann, M. Voigts, C. Weil, R. Jakoby, P. Wang, W. Menesklou and E. Ivers-Tiffee, **"**Investigation of barium strontium titanate thick films for tunable phase shifters" Journal of the European Ceramic Society **21** (2001) 2019

# Chapter 4. Consideration for frequency multiplication based on BST films

The large tunability of the BST film implies that it has a significantly high dielectric nonlinearity. Thus, it is possible to create a low-cost and compact frequency converter, because an input signal frequency can be converted to the desired frequency through the nonlinearity.

## 4.1 Introduction

### 4.1.1 Frequency multiplier

Frequency multipliers can be either passive or active. In passive multipliers, a varactor or step recovery diode is commonly used, while in active multipliers, the design includes transistor-class devices such as the bipolar junction transistors, field effect transistors, or high electron mobility transistors [1]. The frequency multipliers referred to in this chapter make use of a dielectric material, and can be categorized into a passive multiplier class.

Conventional passive multipliers can be classified as resistive or capacitive types. In the first case, the frequency–multiplying mechanism is due to the strong nonlinearity of the conduction current flowing in the diode. In the latter case, the frequency-multiplying mechanism is due to the nonlinear nature of the reactance of the diode [2]. The mechanism of the multiplier presented in this thesis is similar to that of the latter case. However, unlike the conventional semiconductor diode, the nature of an ideal dielectric material is that it does not contain free electrons that generate noise in the device. Moreover, low leakage currents in dielectrics result in some advantages such as lower DC power consumption and higher breakdown voltage.

Despite the extensive research on the applications that make use of the large tunability of the BST films [3-5], little research has been carried out to realize a BST-based frequency conversion [6].

### 4.1.2 Nonlinearity and harmonics of the signal in the BST films

From some previous studies on the nonlinearity of the material for high-frequency application, the resultant harmonics due to the nonlinearity of the bulk material for

resonators has been investigated by Tamura [7]. Frequency conversion by a coplanar waveguide transmission line on a BST film has also been studied [6].

### 4.1.3 Problems and approaches for a BST-based frequency multiplier

However, the nonlinearity of a BST film in such a planar structure is not large enough for an effective frequency conversion. To realize practical frequency conversion, a parallel-plate capacitor was used to make the voltage drop across the capacitance as much as possible. In this chapter, practical frequency conversion due to BST film's nonlinearity is reported.

**Model of the BST-based frequency multiplier**

To make a model, the voltage across BST capacitor is separated into linear part Vc and nonlinear part $V_3$. Figure 4-11 shows the modeling of nonlinear capacitor in to linear part Vc and nonlinear part $V_3$. The capacitance, applied voltage and electric charge have their relation as:

$$V = Vc + V_3 = \frac{Q}{C_0} + \frac{\alpha Q^3}{C_0} \tag{4-1}$$

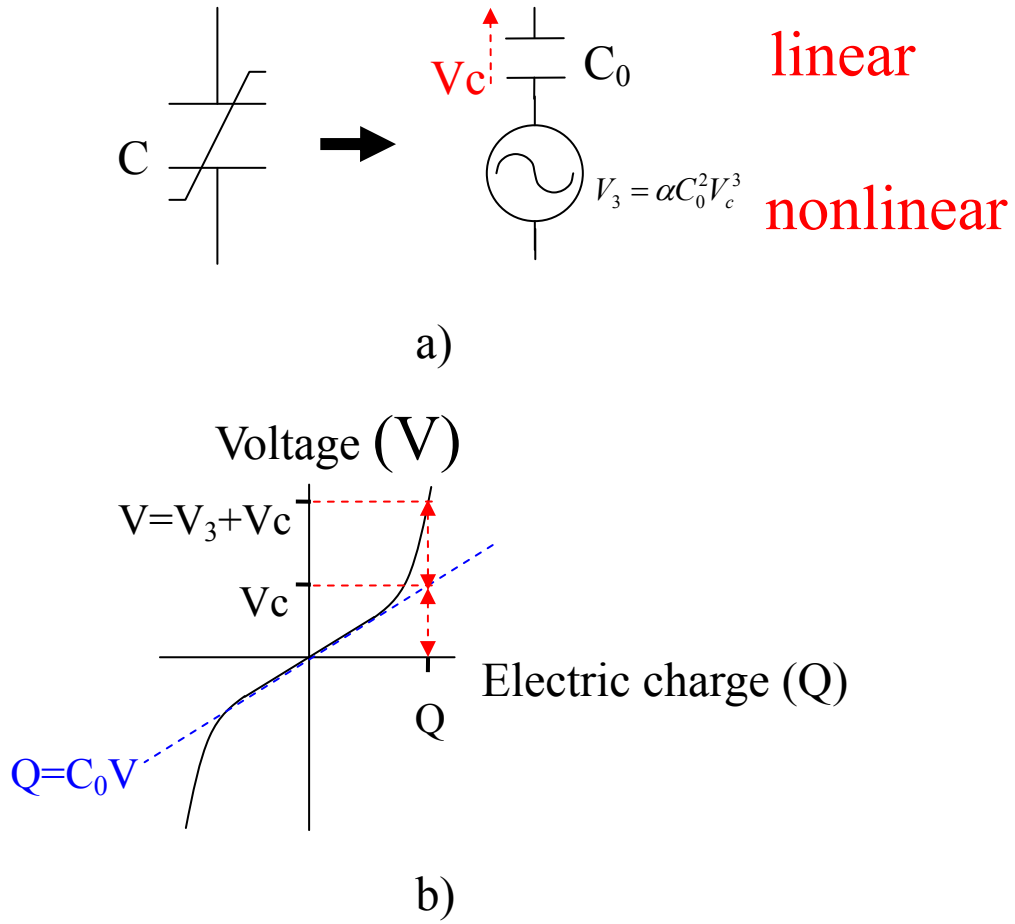


Figure 4-11 a) The voltage across BST capacitor is separated into linear part Vc and nonlinear part $V_3$, b) electric charge inside a BST capacitor after applied an external voltage V.

$$Vc = \frac{Q}{C_0} \tag{4-2}$$

$$V_3 = \frac{\alpha Q^3}{C_0} = \alpha C_0^2 V_c^3 \tag{4-3}$$

,where $\alpha$ is a constant value that is dependent on the type of material and film deposition process.

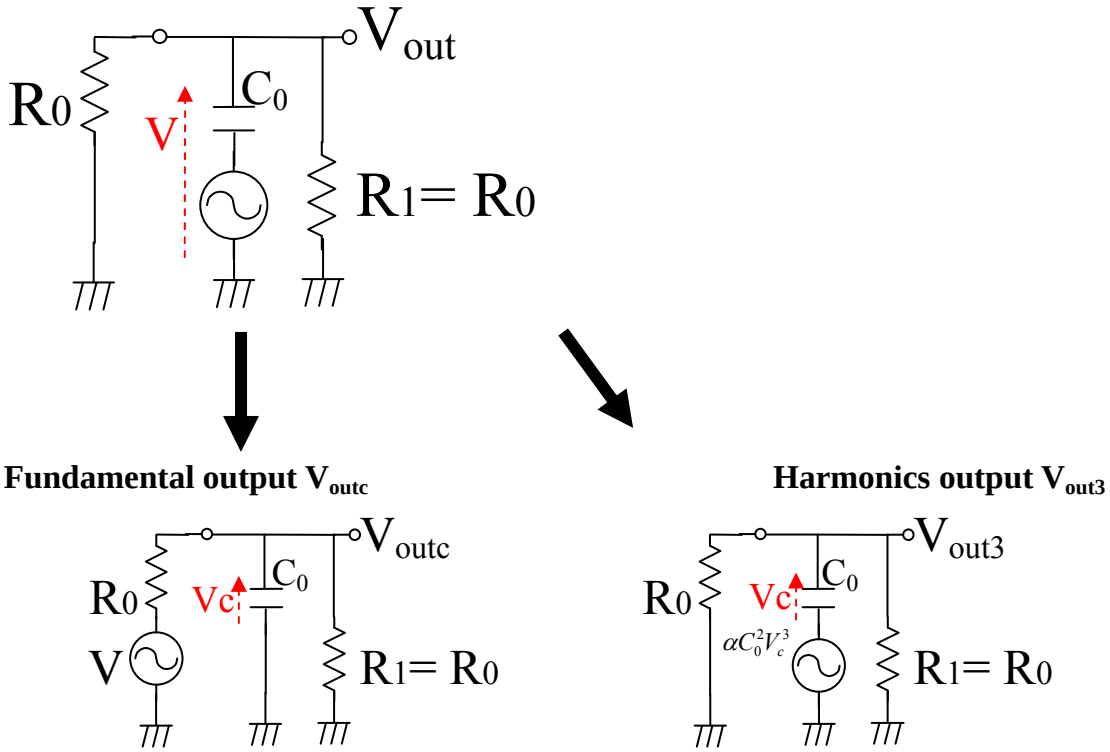


Figure 4-12 The voltage across BST capacitor is separated into linear part Vc and nonlinear part $V_3$, the fundamental output $V_{out}$ and harmonics output $V_{out3}$ can be calculated using the superposition theorem.

Figure 4-12 shows the 3rd harmonics generation. By using the superposition theorem, the output of the harmonics can be calculated as $V_{out3}$, while the output of the linear part is $V_{outc}$. The signal output due to the linear part (Vc) is:

$$V_{out\,c} = \frac{V}{2 + j\omega C_0 R_0} \tag{4-4}$$

From $V_{outc}$, the signal output due to the nonlinear part can be expressed as:

$$V_{out3} = \frac{j\omega C_0 R_0}{2 + j\omega C_0 R_0} \times \alpha C_0 V_{outc}^3 = \frac{j\omega C_0 R_0}{(2 + j\omega C_0 R_0)^4} \times \alpha C_0 V^3 \quad (4\text{-}5)$$

From the above equation, because $V^3$ appears in the expression of the output signal of nonlinear part $V_{out3}$, for a given a sinusoidal wave with frequency $\omega$ and strength $E_0$, the $3\omega$ frequency will appear in the $V_{out3}$, as:

$$V^3 = E_0^3 \sin^3 \omega t = \frac{1}{4} E_0^3 (3\sin \omega t - \sin 3\omega t) \quad (4\text{-}6)$$

This is the reason why there is a third harmonics wave in the signal output of a BST capacitor. To further increase the output power $V_{out3}$, the value of $|2 + j\omega C_0 R_0|$ , where $R_0 = 50\,\Omega$, must be minimized.

Adding a crystal oscillator

Figure 4 -14 shows that after adding a crystal oscillator, 3rd harmonics level is 8 time higher. In this case, there is no current passing through the resistor $R_1$, thus the linear signal output $V_{outc}$ becomes:

$$V_{outc} = \frac{V}{1 + j\omega C_0 R_0} \quad (4\text{-}7)$$

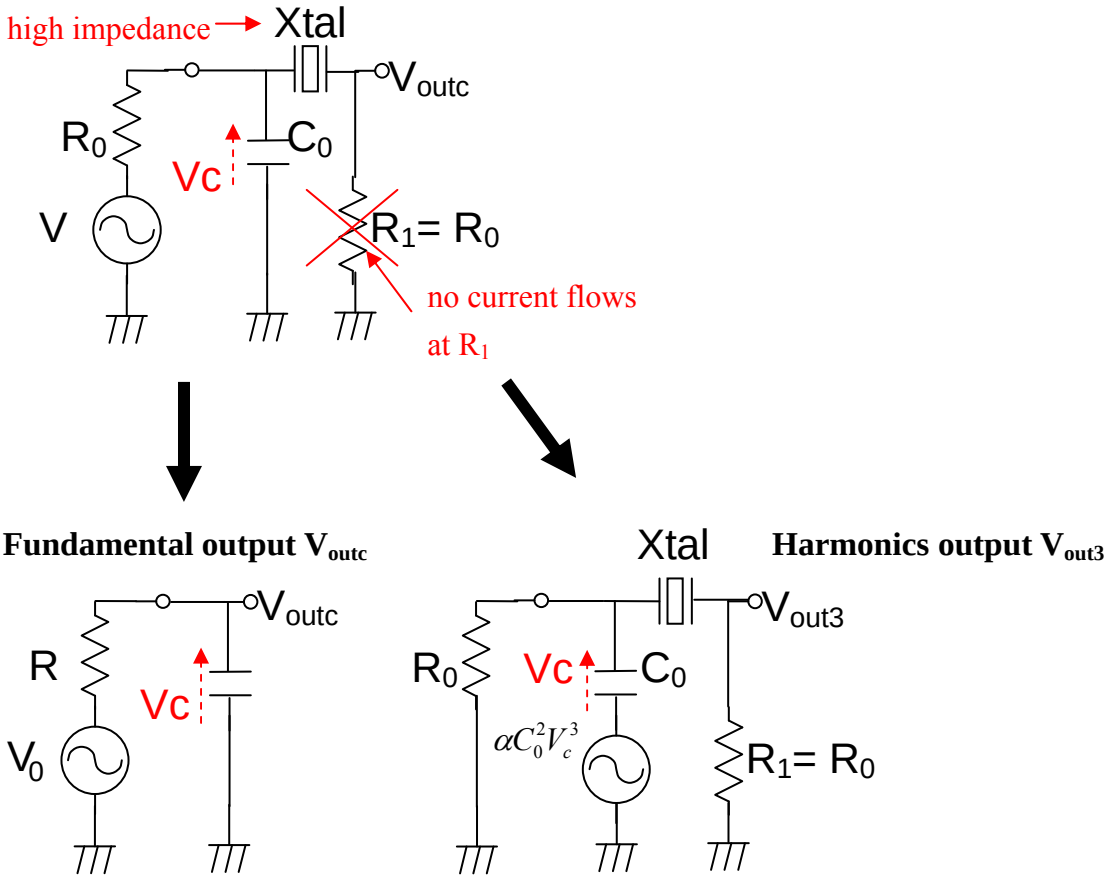


Figure 4-13 After adding a crystal oscillator, no current passes through $R_1$, because the impedance of the crystal oscillator is too high. The fundamental output $V_{out}$ and harmonics output $V_{out3}$ can be calculated using the superposition theorem.

Before adding the crystal oscillator, the nonlinear output signal was:

$$V_{out3} = \frac{j\omega C_0 R_0}{2 + j\omega C_0 R_0} \times \alpha C_0 V_{outc}^3 = \frac{j\omega C_0 R_0}{(2 + j\omega C_0 R_0)^4} \times \alpha C_0 V^3 \approx \frac{j\omega C_0 R_0}{16} \times \alpha C_0 V^3 \qquad (4\text{-}8)$$

After adding the crystal oscillator, the nonlinear output signal becomes:

$$V_{out3} = \frac{j\omega C_0 R_0}{2 + j\omega C_0 R_0} \times \alpha C_0 V_{outc}^3 = \frac{j\omega C_0 R_0}{(2 + j\omega C_0 R_0)(1 + j\omega C_0 R_0)^3} \times \alpha C_0 V^3 \approx \frac{j\omega C_0 R_0}{2} \times \alpha C_0 V^3$$

(4-9)

Thus, after adding the crystal oscillator, the signal level of the nonlinear output signal ($3^{rd}$ harmonics level) is 8 time higher.

Adding an inductor

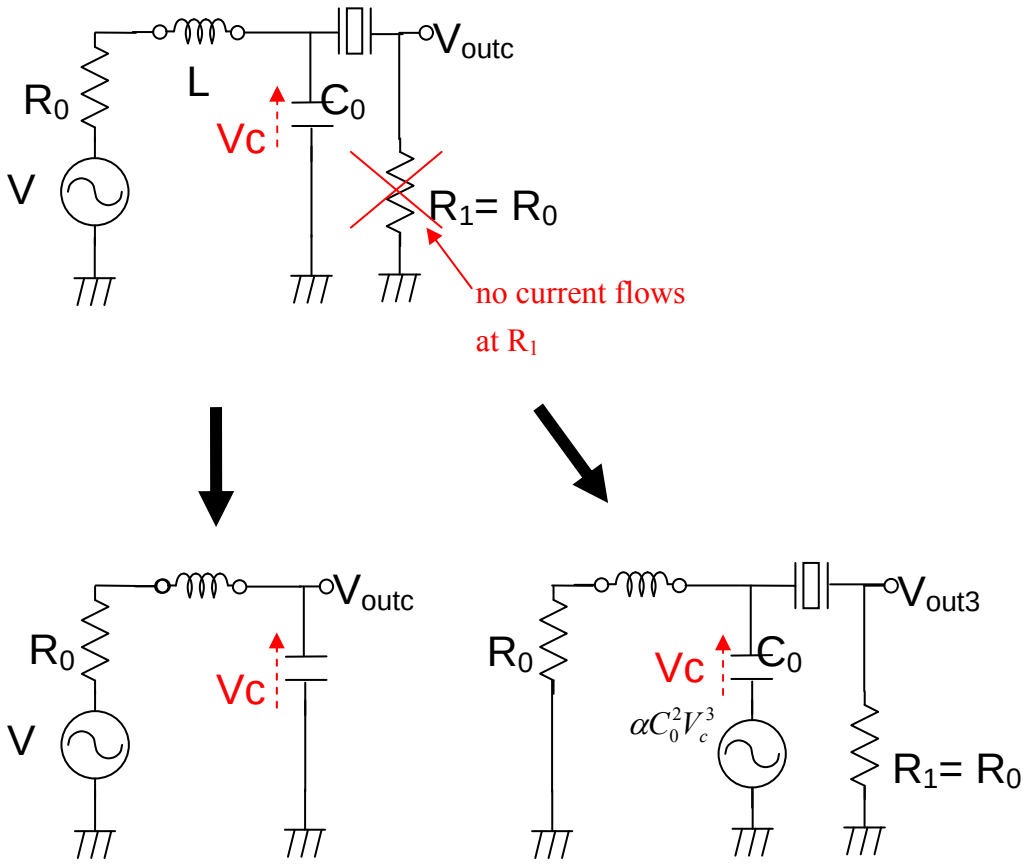


Figure 4-14 After adding a crystal oscillator, no current passes through $R_1$, because the impedance of the crystal oscillator is too high. An inductor was added to increase the voltage signal drop across the capacitor. The fundamental output $V_{out}$ and harmonics output $V_{out3}$ can be calculated using the superposition theorem.

Figures 4-14 shows that adding an inductor can improve a higher $3^{rd}$ harmonics level.

After adding an inductor, the voltage signal drop across the BST capacitor becomes:

$$V_{cap} = \frac{\frac{1}{j\omega C}}{R_0 + \left( j\omega L - \frac{1}{j\omega C} \right)} \times V \tag{4-10}$$

Thus, the nonlinear output signal (3rd harmonics level) becomes

$$V_{out3} = \frac{j\omega C_0 R_0}{2 + j\omega C_0 R_0} \times \alpha C_0 V_{outc}^3 = \frac{j\omega C_0 R_0}{(2 + j\omega C_0 R_0)(j\omega C_0 R_0)^3} \times \alpha C_0 V^3 \tag{4-11}$$

, specifically at the resonant frequency, the voltage signal across the BST capacitor becomes:

$$V_{cap} = \frac{V}{j\omega C R_0} \tag{4-12}$$

Therefore, the nonlinear output signal (3rd harmonics level) becomes:

$$V_{out3} \approx \frac{1}{2(j\omega C_0 R_0)^2} \times \alpha C_0 V^3 \tag{4-13}$$

Accordingly, after adding an inductor, the nonlinear output signal (3rd harmonics level) becomes $\frac{1}{(\omega C_0 R_0)^3}$ times higher.

## 4.2 Experimental

### 4.2.1 Epitaxial BST film growth

To make a parallel-plate BST capacitor, bottom-electrode platinum (Pt) films (150 nm) were deposited on 0.5-mm-thick sapphire substrates by sputtering. Then $Ba_xSr_{1-x}TiO_3$ ($x$=0.5) films were deposited onto the bottom electrode at 600°C by rf-magnetron

sputtering. Pt/sapphire substrates and BST powder targets were positioned parallel to each other and 5.5 cm apart. The thickness of deposited films after 1 h deposition was approximately 200 nm; the deposition rate was 3.3 nm/min. The sputtering gas pressure was 4 Pa with an $Ar/O_2$ gas ratio of 9/1. After sputtering, the stoichiometric composition of the $Ba_{0.5}Sr_{0.5}TiO_3$ films was confirmed by X-ray fluorescence spectroscopy. The crystalline structure of deposited films was confirmed by X-ray diffraction (XRD) analysis.

### 4.2.2 Construction of the frequency multiplier

For a low-frequency converter experiment, a circular top electrode with a diameter of 2.1 mm was formed by sputtering Pt onto the BST films through a metal mask. The thickness of the top electrode was 150 nm.

Low-frequency measurements were carried out with an impedance analyzer (Agilent, 4194A) and an oscilloscope (Tektronik, TDS3052), over the frequency range up to 16 MHz. High-frequency conversion (1 GHz) was confirmed with a measurement system including an oscillator, a notch filter, an attenuator, high-frequency probes and a network analyzer (Advantest, R3767CH).

## 4.3 Results

### 4.3.1 Crystalline structure and electrical properties of the BST varactor

Figure 4-1 shows the results of an XRD $\theta$–$2\theta$ scan for a BST film deposited on sapphire substrate. This result indicates that the BST film tended toward a preferential (111) orientation. The dielectric properties of the BST film capacitor are shown in Fig. 4-2. After applying an external DC bias of 15 V, the relative permittivity of the BST films decreased from 417 to 184. This corresponds to the decrease in the capacitance from 639 to 282 pF, which is a 55.8 % decrease from the maximum value. The loss tangent of the capacitor was less than 2 %.

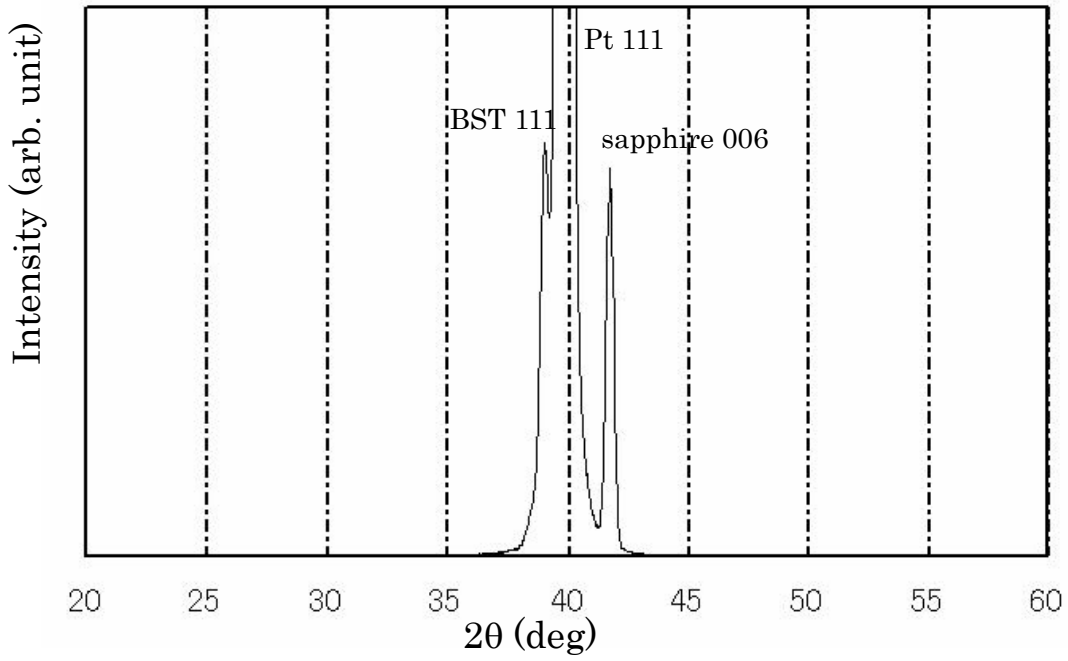


Figure 4-1 XRD analysis of the sputtered BST film.

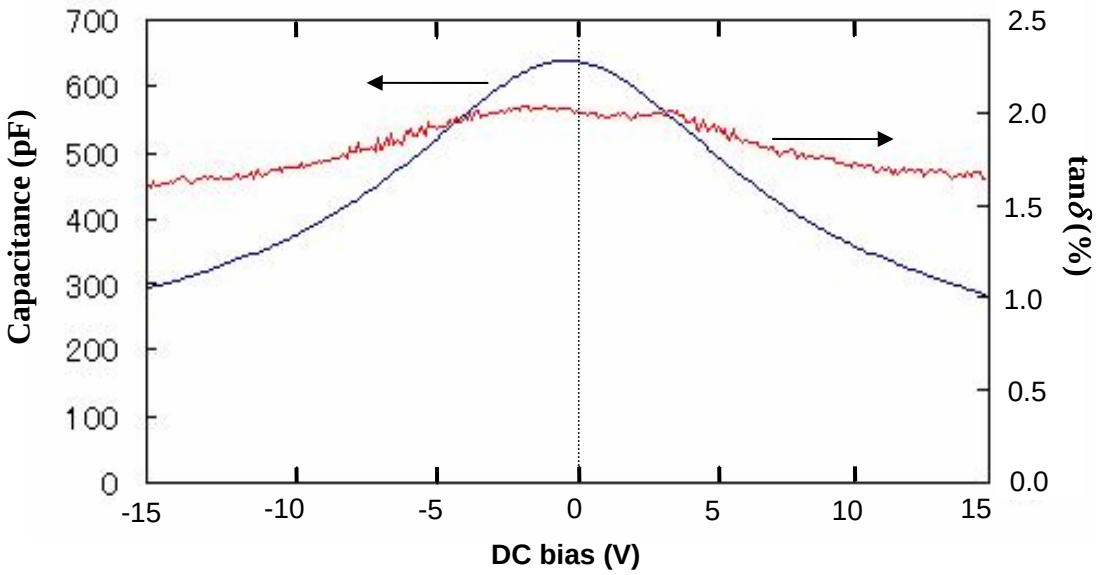


Figure 4-2 Capacitance and loss tangent of the BST capacitor

### 4.3.2 Frequency multiplication below 100 MHz

To demonstrate a frequency converter at low frequency, the principle of frequency conversion is shown in Fig. 4-3. In Fig. 4-3(a), after feeding an input signal through a capacitor, the electric charge and electric current are distorted because of the nonlinear electric charge-voltage characteristics of the BST films [Fig. 4-3(b)]. This distortion includes high-order harmonics whose frequencies are multiples of the input signal frequency. Therefore, these higher-harmonic signals can be filtered out as a signal of the multiplied frequency. The more an input signal is distorted, the larger a harmonic signal becomes.

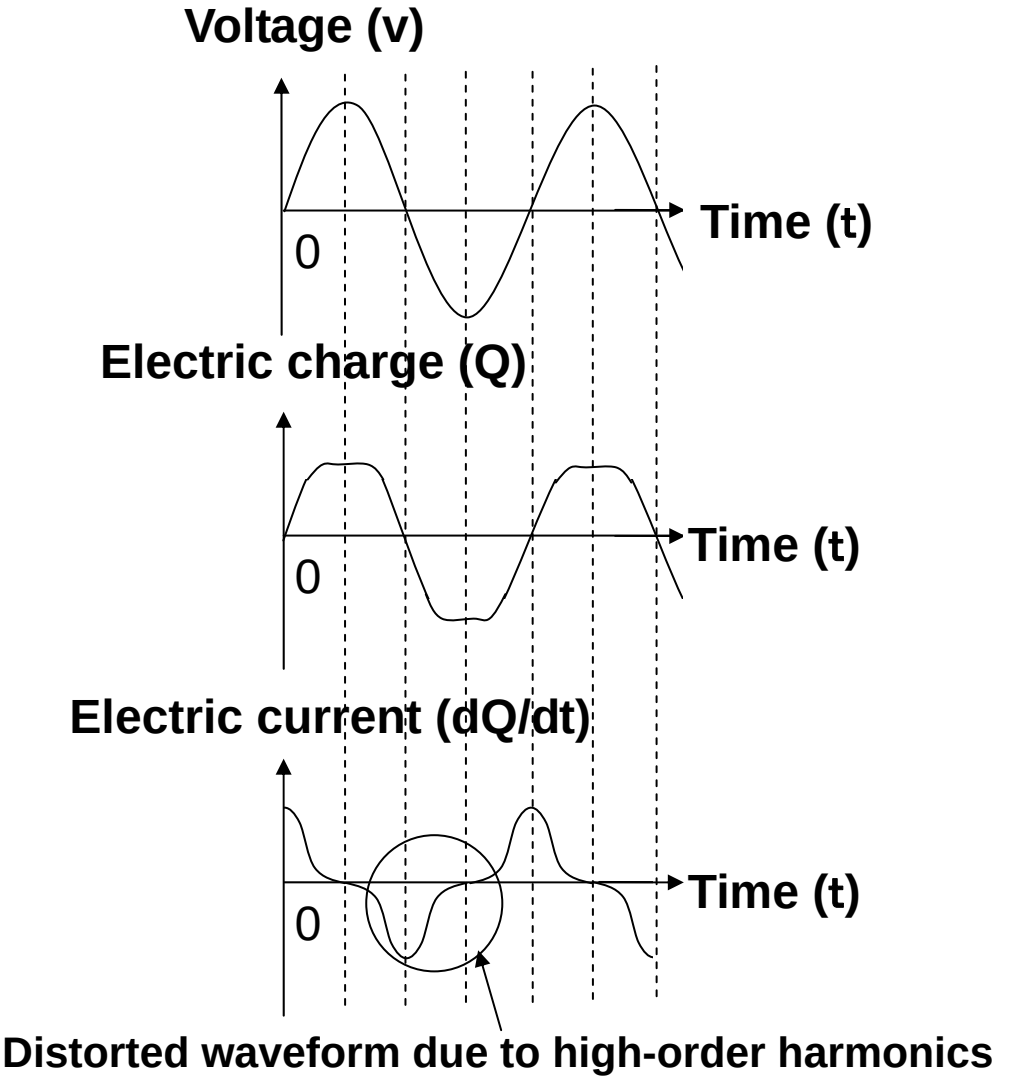


a)

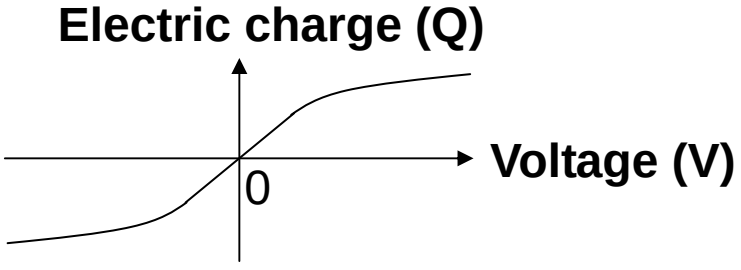


b)

Figure 4-3 Mechanism of signal distortion due to nonlinearity: a) electric current is distorted due to the saturation of electric charge, b) saturated electric charge in the BST capacitor

To obtain a significant signal distortion, high input signal amplitude is necessary. Figure 4-4 shows the measurement setup used to observe the distortion due to the nonlinearity of the BST capacitor. In Fig. 4-4, an oscillator with an internal resistance of Ro=50 Ω, is a signal source. An inductor (10 $\mu$H) is inserted between the oscillator and the capacitor to increase the voltage drop across the capacitor at 2 MHz. Figure 4-5 shows the output signal across the BST capacitor when the input signal amplitudes are 2 V [Fig. 4-5(a)] and 10 V [Fig. 4-5(b)]. The input signal of 2 V did not result in much distortion. The input signal of 10 V resulted in a distorted signal, which can be observed because the distorted output signal waveform is different from a sinusoidal waveform, as shown in Fig. 4-3(a).

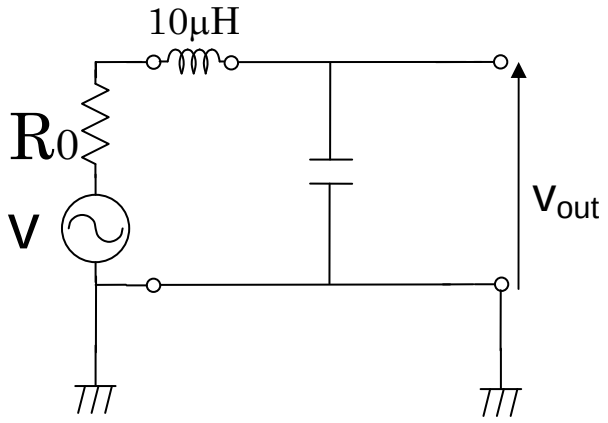


Figure 4-4 Test circuit for observation of nonlinearity in a capacitor

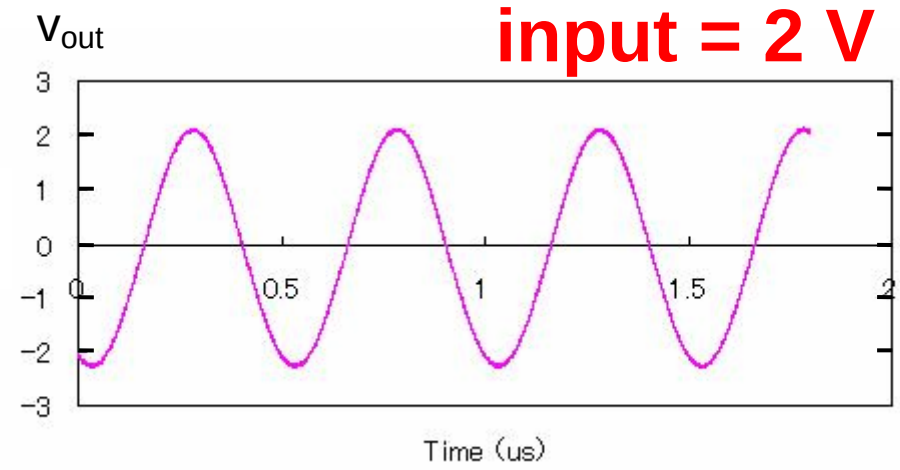


a)

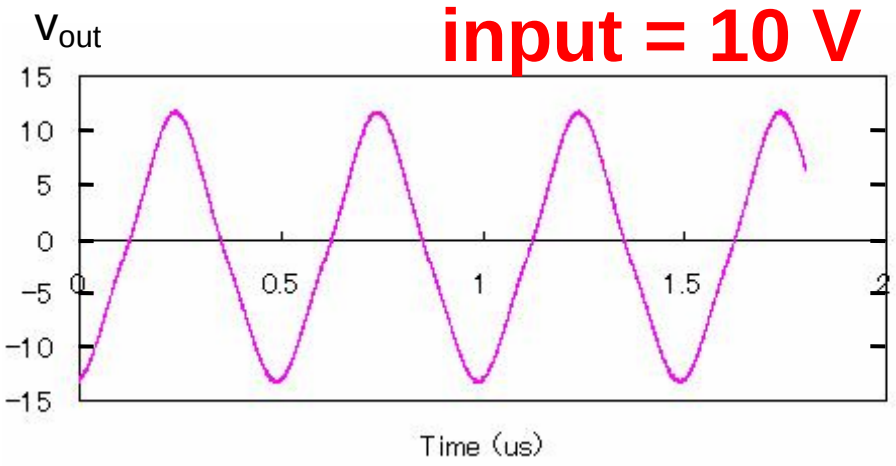


b)

Figure 4-5 a) Signal was not distorted when input signal was 2 V, b) Observed distorted signal when input signal was 10 V

The measurement setup for the frequency conversion at low frequency is shown in Fig. 4-6. The oscillator with internal resistance $R_0$ was connected to the BST capacitor. A 10 $\mu$H inductor was inserted to enlarge the resultant signal amplitude across the capacitor. The crystal resonator (resonating frequency of 6 MHz) was added at the output port to filter the frequency-multiplied signal. In Figs. 4-7(a) to 4-7(c), the input signal of frequency 2 MHz [Fig. 4-7(a)] resulted in the signal across the capacitor [Fig. 4-7(b)] and the harmonics output signal of 6 MHz [Fig. 4-7(c)]. From Figs. 4-7(a) to 4-7(c), the frequency conversion from 2 to 6 MHz was successfully realized.

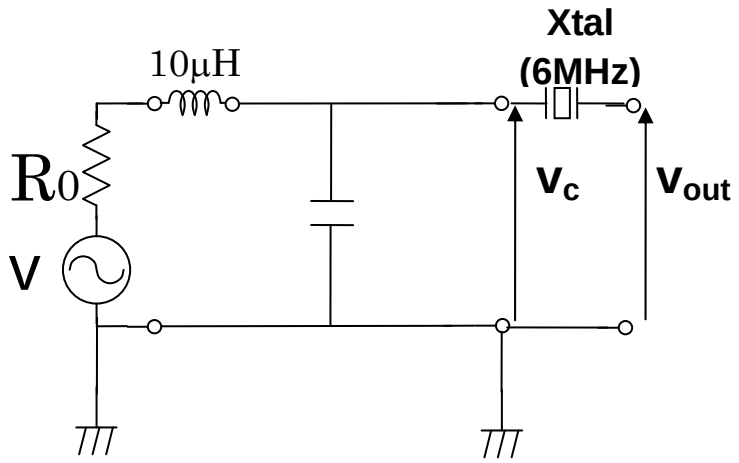


Figure 4-6 Schematics of frequency multiplication at 6 MHz.

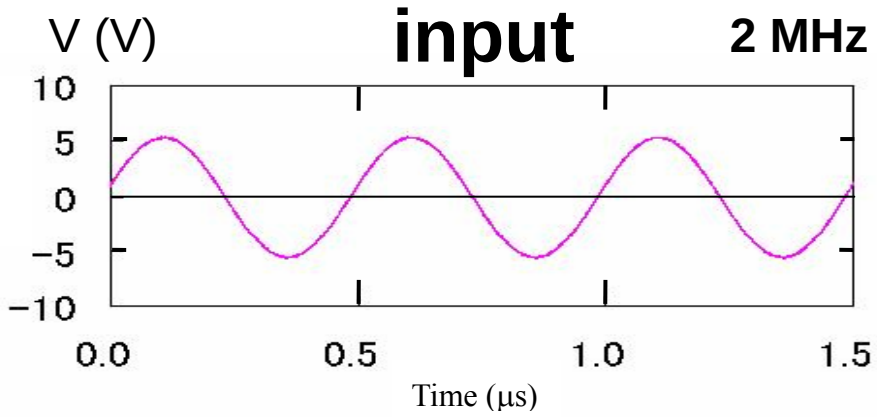


a)

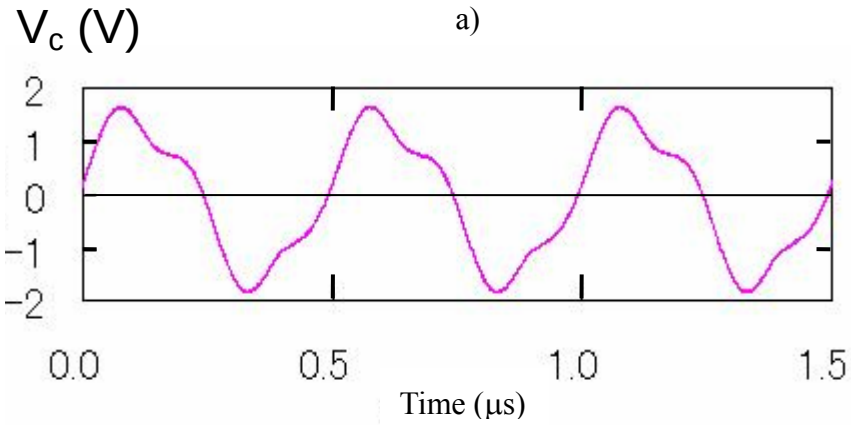


b)

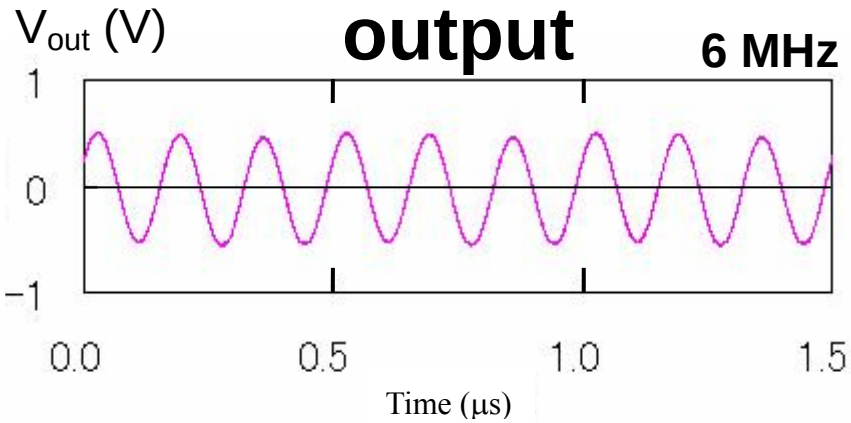


c)

Figure 4-7 a) Input signal at 2 MHz, b) output signal containing no 3rd harmonics c) output signal containing only 3rd harmonics (6MHz) that is filtered by a crystal resonator

### 4.3.3 Frequency multiplication above 100 MHz

To demonstrate the frequency conversion at high frequency, the measurement setup was configured as shown in Fig. 4-8. The signal source is an oscillator that feeds a maximum signal of 19 dBm (19 dBm = 1.99 V). The signal frequency (500 MHz) was fed through the signal source through the 1 GHz notch filter to exclude the 1 GHz harmonics from the signal source itself. Then the input signal was adjusted by an attenuator that attenuated from 0 to 40 dB. The input signal was fed through the high-frequency probes, as the probes were directly attached to each other on the BST layer. The output signal was analyzed using a network analyzer.

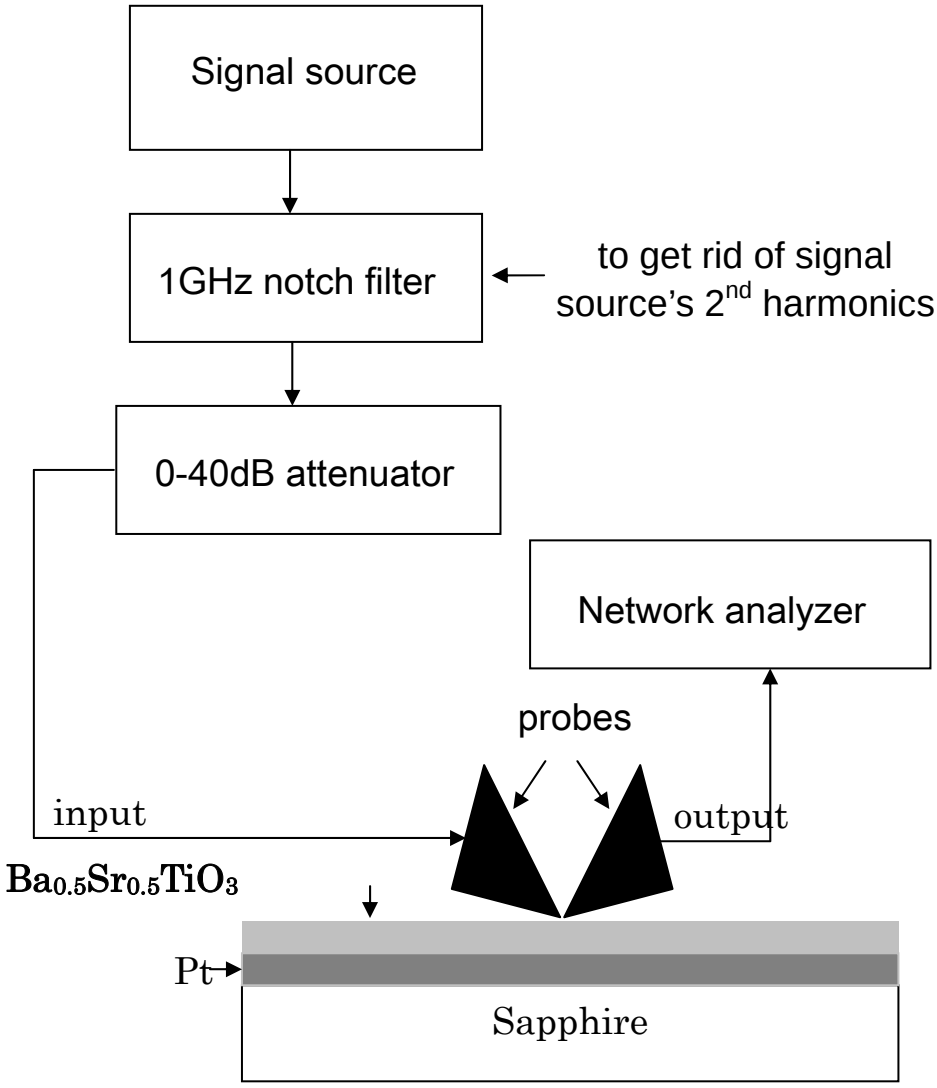


Figure 4-8 Measurement of frequency multiplication at frequency more than 100 MHz.

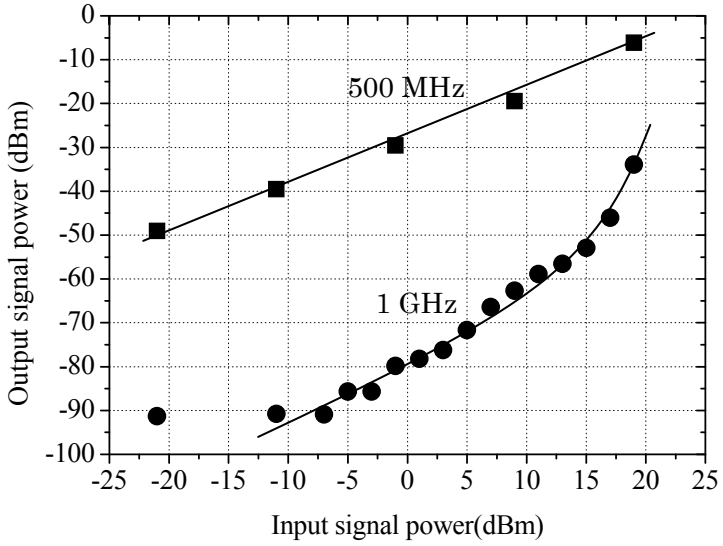


Figure 4-9 Result of the frequency multiplication from 500 MHz to 1 GHz

Figure 4-9 shows the experimental result of the high-frequency conversion. From Fig. 4-9, it was successfully demonstrated that frequency conversion from 500 MHz to 1 GHz can be realized.

## 4.4 Discussion

The conversion of frequencies by using the ferroelectric materials was done through second harmonics and third harmonics. It is important to show the two conditions that the second harmonics or the third harmonics dominates the output power. Such conditions are:

1) The applied external bias

2) The deviation from symmetry of the capacitance-voltage curve.

Figure 4-11 shows the dependence of the capacitance on the DC bias of a BST capacitor. The center of the curve is found to be 0.7 [V] far away from the zero bias. This deviation of the center from zero bias is the reason for the generation of the second harmonics signal in the output power.

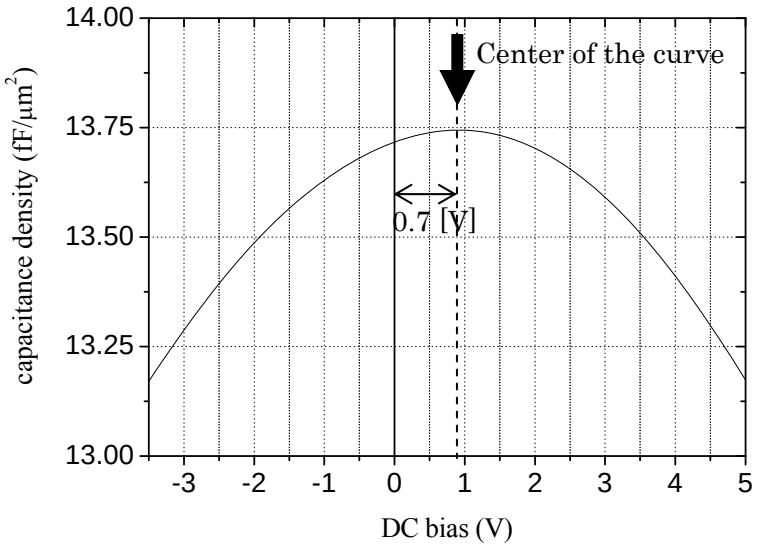


Figure 4-11 Dependence of the capacitance on the DC bias (measured at 1 MHz) of a BST capacitor. The curve is not symmetric and the center of the curve is found to be 0.7 [V] away from zero bias.

If the nonlinearity of the capacitance-voltage characteristics is approximated to the fifth order, the expression for the electric charge (Q), applied voltage (V) and the linear part of the capacitance ($C_0$) (see Fig. 4-11) is:

$$V = V_c + V_3 + V_5 = \frac{Q}{C_0} + \frac{\alpha Q^3}{C_0} + \frac{\beta Q^5}{C_0} \tag{4-14}$$

where,

$V_3$: nonlinearity of the capacitance-voltage characteristics by third order

$V_5$: nonlinearity of the capacitance-voltage characteristics by fifth order

After applied the signal of $mSin[x]$ on the capacitance that has the center deviated from zero equal to $n$ (for example, in the Fig. 4-11, n=0.7 [V]), the applied signal on the center of the capacitance-voltage curve becomes:

$$V_c = n + mSin[x] \tag{4-15}$$

Thus, the output signal (V) becomes:

$$\begin{aligned}
&V = V_c + \alpha C_0^2 V_c^3 + \beta C_0^4 V_c^5 = \\
&\left[ n + \alpha \frac{1}{4} C_0^2 (6m^2 n + 4n^3) + \beta \frac{1}{16} C_0^4 (30m^4 n + 80m^2 n^3 + 16n^5) \right] + \\
&Sin[x]\left[ \alpha \frac{1}{4} C_0^2 (3m^3 + 12mn^2) + \beta \frac{1}{16} C_0^4 (10m^5 + 120m^3 n^2 + 80mn^4) \right] + \\
&Cos[2x]\left[ -\alpha \frac{1}{4} C_0^2 (6m^2 n) - \beta \frac{1}{16} C_0^4 (40m^4 n + 80m^2 n^2) \right] + \\
&Sin[3x]\left[ -\alpha C_0^2 \frac{1}{4} (m^3) - \beta \frac{1}{16} C_0^4 (5m^5 + 40m^3 n^2) \right] + \\
&Cos[4x]\left[ \beta \frac{1}{16} C_0^4 (10m^4 n) \right] + \\
&Sin[5x]\left[ \beta \frac{1}{16} C_0^4 (m^5) \right]
\end{aligned}$$

(4-16)

where,

$\alpha$ and $\beta$ are the constant coefficients,

$$V_c = \frac{Q}{C_0},$$

$$V_3 = \frac{\alpha Q^3}{C_0} = \alpha C_0^2 V_c^3,$$

$$V_5 = \frac{\beta Q^5}{C_0} = \beta C_0^4 V_c^5$$

From the equation (4-16), if the capacitance-voltage curve is symmetric (no deviation from center), i.e. $n$=0, there will not be a second harmonics. In this case, the highest harmonics power level originates from the third harmonics.

In the case that the capacitance-voltage curve is non-symmetric, consider $n$=0.7 [$V$] and $m$=2 [$V$] which is the case when conversion of the signal frequency from 500 MHz to 1 GHz was obtained in this thesis, the constant coefficient of $Cos[2x]$ is much higher than that of $Sin[3x]$. Thus the second harmonics output is much stronger than third harmonics output. This is why the result in Fig. 4-9 shows only second harmonics.

**References**

1) F. Giannini and G. Leuzzi, “Non-linear Microwave Circuit Design”, John Wiley & Sons, West Sussex, (2004), 280

2) R. Gilmore and L. Besser, “Practical RF Circuit Design for Modern Wireless Systems”, Artech House, Massachusetts, (2003), Vol. 2, 501

3) T. O'Sullivan, R. A. York, B. Noren and P. M. Asbeck “Adaptive duplexer implemented using single-path and multipath feedforward techniques with BST phase shifters”, IEEE Transaction of Microwave Theory and Techniques, **53** (2005) 106

4) F. D. Flaviis, N. G. Alexopoulos and O. M. Stafsudd, “Planar microwave integrated phase-shifter design with high purity ferroelectric material”, IEEE Transaction of Microwave Theory and Techniques, **45** (1997) 963

5) J. Nath, D. Ghosh, J. P. .Maria, A. I. Kingon, W. Fathelbab, P. D. Franzon and M. B. Steer, “An electronically tunable microstrip bandpass filter using thin-film Barium-Strontium-Titanate (BST) varactors”, IEEE Transaction of Microwave Theory and Techniques **53** (2005) 2707

6) T. B. Samoilova, K. F. Astafiev, T. Rivkin and D. S. Ginley, “Frequency conversion in coplanar waveguide based on $Ba_xSr_{1-x}TiO_3$ film”, Journal of Applied Physics, **90** (2001) 5703

7) H. Tamura, J. Hattori, T. Nishikawa and K. Wakino, “Third Harmonic Distortion of Dielectric Resonator Materials”, Japanese Journal of Applies Physics, **28** (1989) 2528

# Chapter 5. General conclusions

The main objective of this dissertation was to investigate, for microwave component application, the high-quality BST film growth on different substrates and to demonstrate the frequency conversion by using a BST capacitor up to GHz region.

Our proposal to achieve the first objective is to optimize the film deposition process for epitaxial film growth. In the first stage, the dielectric property of BST films with different Br:Sr composition ratio (BST, x=0.3, 0.4 and 0.5) was studied. At room temperature, the relative permittivity of the BST with composition x=0.3, 0.4, and 0.5 was observed to be 229, 354, and 616, respectively, and the resultant phase shift of the same waveguide structure at 7 GHz was $0.5^{o}$, $1.5^{o}$, and $2.5^{o}$, respectively. This result indicates that the films with x=0.5 has highest tunability.

Substrate selection for epitaxial BST film growth was investigated using MgO, sapphire, and silicon substrates. BST films were directly deposited onto different types of substrates by conventional RF sputtering. The evaluation of BST films as microwave

material was done through the measurement of phase shift of the microwave signal (8 GHz) passing through the waveguide on the BST/substrate.

The results showed that the c-cut sapphire assisted BST epitaxial 111-oriented film growth, while the MgO assisted BST 100-oriented film growth. The BST grown on silicon and r-cut sapphire preferred random orientation. At 7 GHz, The phase shift and dielectric loss due to the BST film (1 $\mu$m) deposited on MgO were $3.0^{o}$ and 0.75%, which is comparable to the values of $2.4^{o}$ and 0.68% in the case of BST deposited on the c-cut sapphire. Thus it was successfully demonstrated that the c-cut sapphire substrates are suitable for depositing BST films for microwave application.

On the other hand, little research has been carried out to realize a BST-based frequency conversion. Frequency conversion by a coplanar waveguide transmission line on a BST film has also been studied before. However, the nonlinearity of a BST film in such a planar structure is not large enough for an effective frequency conversion. In this thesis, a parallel-plate capacitor was used to realize practical frequency conversion because it made the voltage drop across the capacitance higher. Practical frequency conversion due to BST film's nonlinearity was successfully demonstrated. It was also shown that the

higher the frequency conversion efficiency can be achieved by increasing the input signal power. For the conversion from 500 MHz to 1 GHz, the conversion loss was -30 dB at an input power of 20 dBm.

# Acknowledgement

I would like to foremost thank Professor Tadashi Shiosaki for his continuous guidance and support during my studies. He has been very involved with my research and I benefited tremendously from his depth of knowledge in many diverse fields. Professor Soichiro Okamura had encouraged and dedicated much of his time and consideration in the early stage of my research. I am very thankful to Associate Professor Kiyoshi Uchiyama for his vital role in advising and encouraging me during my researches. I want to thank both Professor Jun Ohta and Professor Takashi Fuyuki for their time and for providing me with valuable advices and suggestions. I am very grateful to Assistant Professor Takashi Nishida for his kind instruction about sputtering machine, photolithography, simulations, and other valuable advices. I also like to thank Assistant Professor Hiroaki Takeda especially for his advice about making a BST sputtering target in my earlier research. I am also grateful to Murata Manufacturing Company for providing me with high quality BST powders and a hp8753D network analyzer. I also benefit from helps from Youji Yamashita, Takuma Kohno, and Takuya Tsuchikawa, who I feel happy and proud to work with. I want to thanks everyone in this lab who makes the environment enjoyable and easy to work. Finally I deeply thank for the endless

support from my family.

During my graduate study, I was proud and grateful to receive the Japanese Government (Monbusho) Scholarship, Gakushu Shoreihi (Honors Scholarship), and the Rotary-Yoneyama Memorial Fund Scholarship. I was also granted the Presidential Special Fund of Nara Institute of Science and Technology, which help funding the research apparatus during my study. I am thankful to all the organizations who kindly offered me these monetary supports.

## List of publications

### Printed Works

G. Bhakdisongkhram, Y. Yamashita, T. Nishida and T. Shiosaki, " Dependence of Microwave Properties of $Ba_xSr_{1-x}TiO3$ Thin Films on Substrate", Jpn. J. Appl. Phys. **44** (2005) pp.7098-7102

G. Bhakdisongkhram, S. Okamura and T. Shiosaki, "Precise Measurement of the Dielectric Properties of $Ba_xSr_{1-x}TiO3$ Thin Films by On-wafer Through-Reflect-Line (TRL) Calibration Method", J. Eur. Ceram. Soc. **26** (2006), pp.1835-1839

G. Bhakdisongkhram, Y. Yamashita, T. Nishida, K. Uchiyama, S. Okamura and T. Shiosaki、 "Fabrication of (Ba,Sr)$TiO_3$ Epitaxial Thin Films and Characterization of Microwave Waveguiding Structures", Transactions of the Materials Research Society of Japan **31**[1] (2006), pp.173-176

G. Bhakdisongkhram, Y. Yamashita, T. Nishida and T. Shiosaki, " Consideration for Broadband Frequency Conversion Based on $Ba_{0.5}Sr_{0.5}TiO_3$ Films", Jpn. J. Appl. Phys. **45** (2006) pp.7479-7483

### Conferences

G. Bhakdisongkhram, S. Okamura and T. Shiosaki,「Preparation of Low Loss Microwave Dielectric BaxSr1-xTiO3 Thin Films and Their Properties in GHz Region」, 第51回応用物理学関係連合講演会、28a-ZL-7, 東京都八王子市, 東京工科大学, 2004年3月, 講演予稿集 p.593.

G. Bhakdisongkhram, S. Okamura and T. Shiosaki,「Precise Measurement of the Dielectric Properties of the Dielectric $Ba_xSr_{1-x}TiO_3$ Thin Films by On-wafer Through-Reflect-Line (TRL) Calibration Method」, Third International Conference on Microwave Materials and Their Applications, O-A27, 愛知県犬山市, 2004 年 10 月, 講演予稿集 p.65.

G. Bhakdisongkhram, Y. Yamashita, T. Nishida and T. Shiosaki,「誘電体薄膜のチューナブル特性」, 誘電体研究委員会第 82 回例会, 京都, 2005 年 5 月 (招待講演)

G. Bhakdisongkhram, Y. Yamashita, T. Nishida and T. Shiosaki,「Influence of the Substrate Type Dependence on the Microwave Properties of the BST Thin Films」, The 22nd Meeting on Ferroelectric Materials and Their Applications, 京都, 2005 年 5 月

.

Y. Yamashita, G. Bhakdisongkhram, T. Nishida, K. Uchiyama, S. Okamura and T. Shiosaki,「各種基板上に成長した(Ba,Sr)$TiO_3$ 薄膜の GHz 帯における特性評価」, 第 66 回応用物理学会学術講演会, 7a-L-2, 徳島県徳島市, 徳島大学, 2005 年 9 月, 講演予稿集 p.457

G. Bhakdisongkhram, Y. Yamashita, T. Nishida, K. Uchiyama and T. Shiosaki,「Dependence of Microwave Properties of Epitaxial (Ba,Sr)$TiO_3$ Thin Films on Substrate」, GIST-NAIST Symposium, Korea, 2005年10月

Y. Yamashita, G. Bhakdisongkhram, T. Nishida, K. Uchiyama, S. Okamura and T. Shiosaki,「Fabrication of (Ba,Sr)$TiO_3$ Epitaxial Thin Films and Characterization of Microwave Waveguiding Structures」, 16$^{th}$ MRS-Japan Academic Symposium, 東京, 2005年12月

G. Bhakdisongkhram, T. Kohno, Y. Yamashita, T. Nishida, K. Uchiyama and T. Shiosaki,「サファイア基板上への(Ba,Sr)$TiO_3$ 薄膜の作製と GHz 帯における特性評価」, 第 53 回応用物理学関係連合講演会, 25a-P6-8, 東京都世田谷区, 武蔵工業大学, 2006 年 3 月, 講演予稿集 p.214

G. Bhakdisongkhram, T. Kohno, Y. Yamashita, T. Nishida, K. Uchiyama and T. Shiosaki, 「マイクロ波チューナブル素子用 BST 薄膜に関する研究」, 学長裁量経費受領者による研究成果報告講演会, 奈良県生駒市、奈良先端科学技術大学院大学, 2006 年 5 月

G. Bhakdisongkhram, T. Kohno, Y. Yamashita, T. Nishida, K. Uchiyama and T. Shiosaki,「BST 薄膜を用いた広帯域周波数逓倍器の作製及び評価」, The 23nd Meeting on Ferroelectric Materials and Their Applications, 京都, 2006 年 5 月

G. Bhakdisongkhram, T. Kohno, Y. Yamashita, T. Nishida, K. Uchiyama and T. Shiosaki,「Nonlinear Epitaxial BST Film for Broadband Frequency Converter Element」, Fourth International Conference on Microwave Materials and Their Applications, O-53, Oulu, Finland, 2006 年 6 月

T. Kohno, G. Bhakdisongkhram, Y. Yamashita, T. Nishida, K. Uchiyama and T. Shiosaki,「マイクロ波導波路用$(Ba_{0.5}Sr_{0.5})TiO_3$薄膜の電気的特性評価」, 第 67 回応用物理学会学術講演会, 30p-M-6, 滋賀県草津市, 立命館大学, 2006 年 9 月, 講演予稿集 p.209

G. Bhakdisongkhram, T. Kohno, Y. Yamashita, T. Nishida, K. Uchiyama and T. Shiosaki,「Frequency Conversion by Using a BST Capacitor」, The 5th Asian Meeting on Electroceramics (AMEC5), Bangkok, Thailand, 2006 年 12 月